

Chapter Title: NEPTUNE'S RING SYSTEM

Chapter Author(s): CAROLYN C. PORCO, PHILIP D. NICHOLSON, JEFFREY N. CUZZI, JACK T. LISSAUER and LARRY W. ESPOSITO

Book Title: Neptune and Triton

Book Editor(s): Dale P. Cruikshank

Published by: University of Arizona Press. (1995)

Stable URL: <https://www.jstor.org/stable/j.ctt1gn6b0z.21>

---

JSTOR is a not-for-profit service that helps scholars, researchers, and students discover, use, and build upon a wide range of content in a trusted digital archive. We use information technology and tools to increase productivity and facilitate new forms of scholarship. For more information about JSTOR, please contact support@jstor.org.

Your use of the JSTOR archive indicates your acceptance of the Terms & Conditions of Use, available at

<https://about.jstor.org/terms>



*University of Arizona Press* is collaborating with JSTOR to digitize, preserve and extend access to *Neptune and Triton*

JSTOR

## PART V

# Rings



## NEPTUNE'S RING SYSTEM

CAROLYN C. PORCO

*University of Arizona*

PHILIP D. NICHOLSON

*Cornell University*

JEFFREY N. CUZZI

*NASA Ames Research Center*

JACK J. LISSAUER

*State University of New York, Stony Brook*

and

LARRY W. ESPOSITO

*University of Colorado*

We review the current state of knowledge regarding the structure, particle properties, kinematics, dynamics, origin, and evolution of the Neptune rings derived from Earth-based and Voyager data. Neptune has a diverse system of five continuous rings—2 broad (Galle and Lassell) and 3 narrow (Adams, Le Verrier, and Arago)—plus a narrow discontinuous ring sharing the orbit of one of its ring-region satellites, Galatea. The outermost Adams ring contains the only arcs observed so far in Voyager images. These were responsible for most of the Earth-based stellar occultation detections of circum-Neptunian material in the mid-1980s. Three other Earth-based detections recorded material of some sort within Lassell and Galle, and interior to Galle. The five arcs vary in angular extent from  $\sim 1^\circ$  to  $\sim 10^\circ$ , and exhibit internal azimuthal structure with typical spatial scales of  $\sim 0.5^\circ$ . All five lie within  $\sim 40^\circ$  of longitude. Combined analysis of Earth-based occultation data and Voyager photometry yields typical optical depths of  $\tau_{\text{arcs}} \sim 0.1$ , and  $\tau \sim 0.003$  for the two narrow rings Adams and Le Verrier. Dust is present throughout the Neptune system and measurable quantities of it were detected over Neptune's north pole. The Adams ring (including the arcs) and the Le Verrier ring contain a significant fraction of dust, comparable to that observed in Saturn's F ring; Lassell appears to have a different mix of particle sizes than Le Verrier or Adams. The Neptune ring particles are as dark as those in the rings of Uranus (with a single-scattering albedo  $\omega \sim 0.04$ ), are probably red, and may consist of ice "dirtied" with silicates and/or some carbon-bearing material. A kinematic model for the arcs derived from Voyager data, the arcs' physical characteristics, and their orbital geometry and phasing are all roughly in accord with single-satellite arc shepherding by Galatea, though the presence of small kilometer-sized bodies embedded either within the arcs or placed at their Lagrange points may explain some inconsistencies with

this model. Detailed numerical simulations demonstrate the plausibility of a model in which disrupted satellites provide the source of the Neptune rings and arcs.

## I. INTRODUCTION

Soon after the rings of Uranus were serendipitously discovered in March 1977, establishing definitively that Saturn was not the only ringed planet, attempts began in earnest to search for rings around the planet Neptune. The Uranian rings had been found during a stellar occultation, an observation having enormous advantages over Earth-based imaging for detecting distant, narrow and dark rings like those of Uranus, and this technique became the method of choice for searching for Neptunian rings.

Because of Neptune's present proximity to the galactic plane (as seen from the Earth), many opportunities arose in the 1980s to observe stellar occultations by Neptune<sup>a</sup>. The first report of circum-Neptunian material was made by Nicholson and Jones (1980) who observed a Neptune stellar occultation by Neptune in August 1980. Their sighting, however, was tentative, and unconfirmed. Three Neptune stellar occultations were observed during the year 1981 involving multiple observations of the same occultation at widely spaced sites to maximize coverage and provide independent confirmation of any putative ring occultations. An opaque, Neptune-orbiting body was detected on 24 May 1981 and was correctly identified as a satellite (Reitsema et al. 1982), later imaged by Voyager and named Larissa. However, the remaining two 1981 occultations yielded negative results, as did another which occurred during 1983 (Elliot et al. 1981, 1985; Hubbard et al. 1985). Based on analogy with Uranus, the emphasis in these studies was on finding continuous rings. No unambiguous ring occultation signature was reported from any of the dozen or so independent chords.

A breakthrough occurred in July 1984, when multi-wavelength observations of an occultation of a particularly bright star were made simultaneously at three telescopes in South America. Although separated by up to 100 km, all three telescopes recorded on ingress a near-simultaneous partial occultation in their infrared channels, corresponding to a ring segment with a radial width  $W = 15$  km and an average normal optical depth  $\tau \approx 0.13$  (Manfroid et al. 1986; Hubbard et al. 1986; Sicardy et al. 1991). No corresponding feature was seen when the star's track crossed this same radial range on the opposite side of the planet. As a result, the term "arc" was proposed for the feature by Hubbard et al. (1986).

<sup>a</sup> Only a single stellar occultation was observed prior to 1980 on 7 April 1968 (Koalevsky and Link 1969; Freeman and Lynga 1970). However, while this observation provided the first accurate data on Neptune's radius and oblateness, no convincing evidence of a ring system was reported. (A subsequent report by Guinan et al. [1982] of a possible ring between 28,500 and 32,800 km based on data from this event, is contradicted by higher quality occultations in 1983 and 1985 [Elliot et al. 1985; Hubbard et al. 1985; Sicardy et al. 1991].)

Since then, over 20 successful Neptune system occultations have been observed at over 40 observatories. Five of these observations yielded positive identifications of material in orbit around Neptune; three of these detections were confirmed by more than one telescope. Recently, Neptune stellar occultations observations acquired prior to July 22, 1984 were re-examined for the presence of discontinuous circum-Neptunian rings: one of these lightcurves revealed the presence of arc-like material (Sec. II.B.1). Though meager, these groundbased data provide, to this day, the best estimates of arc widths and optical depths, and restrictive upper limits on the radially integrated optical depths of the continuous rings (Sec. II).

Immediately evident upon the discovery of Neptune's arcs was the fact that ring material would not remain configured into discrete longitudinally-limited arcs if left to itself, but would soon spread to form a complete ring. Several theoretical models were proposed in the mid 1980s, all of which relied on the perturbing action of gravitational resonances to explain the azimuthal confinement of the arcs (Sec. III.A.1). One of these models suggested that acoustic oscillations within Neptune might provide the necessary perturbations; two models suggested different ways in which nearby satellites might shepherd ring material into arcs. While the first of these suggestions was easily refuted on the basis of a gross mismatch between the approximate orbital location of the arcs and the expected locations of Neptunian acoustic oscillation resonances, the information available on the Neptune arcs prior to 1989 was insufficient to determine which satellite perturbation model, if any, was successful in explaining arc confinement. The large uncertainties in the estimates of Neptune-centered radii for the groundbased arc detections prevented the formulation of an arc kinematic model like that available for the Uranian rings prior to the Voyager Uranus encounter (French et al. 1986). Without an accurate and precise geometric/kinematic model, serious dynamical investigations were impossible.

In August 1989, Voyager 2 encountered Neptune, its last planetary flyby in a decade-long tour of the outer solar system. To date, the most recently published ephemeris describing Voyager's passage through the Neptune system is that of Jacobson et al. (1991). Reconstruction of the spacecraft trajectory using these results shows that Voyager approached the planet from an asymptotic planetocentric latitude of  $-29^\circ$  and phase angle of  $15^\circ$ , flew through the ring plane (ascending node) at a distance of  $\sim 85,200$  km and phase angle of  $25^\circ$ , passed within  $29,200$  km of the northern cloud tops of Neptune, flew again through the ring plane (descending node) at a distance of  $\sim 104,100$  km and a phase angle of  $155^\circ$ , and then left the system on a  $-24^\circ$  latitude asymptote at a phase angle of  $133^\circ$ . During this time, Voyager's cameras, ultraviolet spectrometer and polarimeter, and *in situ* particles and fields experiments all successfully acquired data on Neptune's rings and satellites. A far richer, though still incomplete, picture of this distant set of rings and its relation to the inner Neptunian satellites has consequently emerged.

This chapter reviews the current state of our knowledge regarding the

structure, particle properties, kinematics, dynamics, origin, and evolution of the Neptune rings. The reader should bear in mind that much work remains to be accomplished in all these areas, and what is presented herein is more appropriately considered a statement of progress rather than a complete and final assessment.

## II. RING STRUCTURE AND PARTICLE PROPERTIES

The ~800 images of the Neptune ring system collected by Voyager 2 constitute the largest data set presently available on Neptune's rings. The handful of positive detections of the Neptune arcs from groundbased observations during the 1980s, plus the single simultaneous Voyager Photopolarimeter (PPS) and Ultraviolet Spectrometer (UVS) stellar occultation arc detection, comprise a small but powerful contribution to this collection. In addition to these remote-sensing observations, *in situ* plasma and dust measurements were gathered by the Voyager Plasma Wave (PWS), Planetary Radio Astronomy (PRA), Cosmic Ray (CRS), and Low Energy Charged Particle (LECP) instruments as the spacecraft flew through the outer part of the ring region and over Neptune's north pole.

Each of these data types supplies important clues in understanding the Neptune ring system. Images provide the global two dimensional view of system structure and distribution of material, including satellites, while occultation data supply a direct measure of the optical depth and information on high-resolution radial structure. The combination of imaging and occultation data can be used to infer and/or constrain particle light scattering behavior, albedo, particle shape and size distribution. *In situ* measurements of micron-sized ring particles obtained at and between the two Voyager ring plane crossings (see Sec. II.A.4) provide information on particle masses, size distributions, number densities and extent above and below the mean ring plane. The picture of the Neptune ring system that has emerged from the synthesis of these varied data types is presented in this section.

### A. Ring System Structure

The low light levels at Neptune and the extremely low albedo of the rings (Sec. II.C) required uncommonly long exposures for imaging the rings with the Voyager cameras. The combination of the spacecraft's translational motion and the small irregular motions of the scan platform on which the cameras sit caused the vast majority of images to be badly smeared. In those cases when translational motion was the larger of the two contributing effects, an attempt was made to cancel it out during the exposure by deliberate rotation of either the scan platform or the spacecraft itself—a technique called target motion compensation. Those images having acceptably low smear constitute a very small subset of all Voyager Neptune ring images. Consequently, only a relatively small number of all frames has been useful for extracting detailed structural and geometric information on the rings.

Because of the geometry of the spacecraft's approach to and recession from Neptune, the bulk of Voyager imaging data on the rings falls primarily at two phase angles:  $\phi \sim 15^\circ$  (inbound) and  $\phi \sim 135^\circ$  (outbound). However, the highest-resolution ring images were taken through the narrow angle camera between  $-12.6$  and  $+18.3$  hr from closest approach to the planet, when the spacecraft-ring geometry and phase angle were rapidly varying. These narrow angle images, along with an occasional accompanying wide angle frame, were targeted specifically to the arcs after previous imaging observations had been used to determine their positions and orbital motion. Another set of images was motion-compensated and acquired at phase angles  $154 \lesssim \phi \lesssim 160^\circ$ , while the spacecraft-ring range was  $\lesssim 120,000$  km, including three images taken near the second ring plane crossing. Table I lists these images along with the following characteristics: the Voyager Flight Data System (FDS) identifier, the camera (narrow angle or wide angle), the exposure time, the spacecraft event time (UTC) at which the image was acquired, the range from the spacecraft to a point on the Adams ring closest to the center of the frame, and the image scale, the radial ring plane scale, and the phase angle at this point. Many of the frames in Table I were used in studying the high-resolution structure of the rings and arcs, and for determining the poles of the Adams, Le Verrier and Galle rings.

*1. Radial Structure from Voyager Imaging Data.* Neptune's ring system is notable for its large fractional abundance of fine, micron-sized "dust" particles and the low albedo of its macroscopic particles (Sec. II.C). Due to these circumstances, the rings are most easily seen, and their radial structure most readily characterized, in images taken at moderate to high phase angles at which fine material is highlighted by diffraction. Figure 1 is a pair of images taken at  $\phi = 134^\circ$  which illustrates the Neptune ring system; Fig. 2 is an image taken at  $\phi = 135^\circ$  of the region of the rings in the vicinity of the shadow of Neptune showing details not observable in Fig. 1. Figure 3 is a radial scan of the rings taken from FDS 11412.51 (Smith et al. 1989, fig. 14), a high phase image similar to Fig. 1, after the background scattered light from the disk of Neptune was removed (Showalter and Cuzzi 1992a). The official International Astronomical Union (IAU) names of the rings are indicated.

It is apparent from Figs. 1, 2 and 3 that the ring system consists of several continuous rings, three, and maybe four, of which are quite narrow (i.e.,  $\lesssim 100$  km wide). Figure 4 is a cartoon showing all presently known components of the Neptune ring system, along with its associated satellites (Sec. II.A.7). The Adams ring lies at a distance of  $62932.57 \pm 0.02$  km from Neptune (Porco 1991; Horanyi and Porco 1993); presumably its orbital semi-major axis is identical to that calculated for the arcs which orbit within it (Sec. III). The narrow Le Verrier ring is  $53200 \pm 20$  km from Neptune (Porco et al. 1992; Showalter and Cuzzi 1992b; Porco et al. 1995; Showalter and Cuzzi 1995). A third narrow feature (Showalter and Cuzzi 1992b) apparently occupies the same orbit as one of the Voyager-discovered satellites, Galatea,  $\sim 980$  km interior to the Adams ring. This unnamed feature is so faint in

**TABLE I**  
**Neptune Rings Imaging Sequence Near Closest Approach**

FDS no.	Camera N/W	Exposure Time (s)	Spacecraft Event Time <sup>a</sup>	Range <sup>b</sup> (km)	Image Scale <sup>b</sup> (km pixel <sup>-1</sup> )	Radial Scale <sup>b</sup> (km pixel <sup>-1</sup> )	Phase Angle <sup>b</sup> (deg)
11374.31	N	15.36	236 15 19 02	876,510	6.9	14.6	14.7
11374.38	N	30.72	236 15 24 30	870,670	6.8	14.3	14.8
11374.45	N	61.44	236 15 29 50	864,930	6.8	14.0	14.8
11374.50	W	15.36	236 15 30 14	864,270	50.8	103.9	14.9
11381.14	N	15.36	236 20 41 26	431,560	3.4	6.5	15.4
11381.20	N	15.36	236 20 46 14	426,440	3.3	6.5	15.4
11381.26	N	15.36	236 20 51 02	421,340	3.3	6.4	15.4
11381.31	W	15.36	236 20 51 02	421,380	24.7	47.8	15.4
11382.06	N	15.36	236 21 23 02	397,780	3.1	4.2	7.9
11382.12	N	15.36	236 21 27 50	392,280	3.1	4.2	7.9
11382.18	N	15.36	236 21 32 38	387,360	3.0	4.1	7.8
11382.23	W	15.36	236 21 32 38	387,250	22.7	31.1	7.8
11386.17	N	15.36	237 00 43 50	267,780	2.1	2.9	8.2
11386.22	W	15.36	237 00 43 50	267,850	15.7	21.9	8.2
11391.10 <sup>c</sup>	W	111.36	237 04 37 26	106,610	6.3	12.1	156.7

11391.14 <sup>c</sup>	W	103.68	237	04	41	113,170	6.6	13.7	158.4
11391.18 <sup>c</sup>	W	111.36	237	04	50	120,260	7.1	16.4	160.1
11391.55 <sup>d</sup>	W	15.36	237	05	14	43,250/154,660	2.5/9.0	5.4/18.8	156.0/155.7
11391.57 <sup>d</sup>	W	15.36	237	05	15	45,800/154,780	2.7/9.0	5.3/17.7	154.8/155.1
11391.59 <sup>d</sup>	W	15.36	237	08	17	48,450/153,910	2.8/9.0	5.2/16.6	153.6/154.5
11403.01	W	111.36	237	14	06	14	616,490	36.2	67.2
11403.17	W	255.36	237	14	17	50	623,690	36.6	97.8
11403.30	W	111.36	237	14	29	26	635,730	37.3	99.6
11403.43	W	111.36	237	14	39	50	646,590	38.0	101.0
11404.01	W	255.36	237	14	53	02	665,030	39.1	72.8
11404.17	W	255.36	237	15	05	50	673,540	39.6	105.1
11404.33	W	255.36	237	15	18	38	686,720	40.3	106.9
11404.46	W	111.36	237	15	30	14	698,830	41.0	108.4
11412.31	N	61.44	237	21	42	39	1,100,460	8.6	11.0
11412.38	N	61.44	237	21	48	15	1,106,160	8.7	11.1
11412.46	N	111.36	237	21	54	14	1,112,230	8.7	11.1
11412.51	W	111.36	237	21	54	14	1,112,720	65.3	82.9

<sup>a</sup> Time given is the midpoint of the exposure. Closest approach to Neptune occurred at 237/03:55:40.

<sup>b</sup> Measurement was made at a point on the Adams ring close to the center of the image, unless otherwise stated.

<sup>c</sup> Smear is >300 pixels in these high phase images. Radial midpoint of the smeared Adams ring falls off the frame in 11391.10 and 11391.18.

<sup>d</sup> Measurements on the ring plane crossing images refer to the near/far arms.

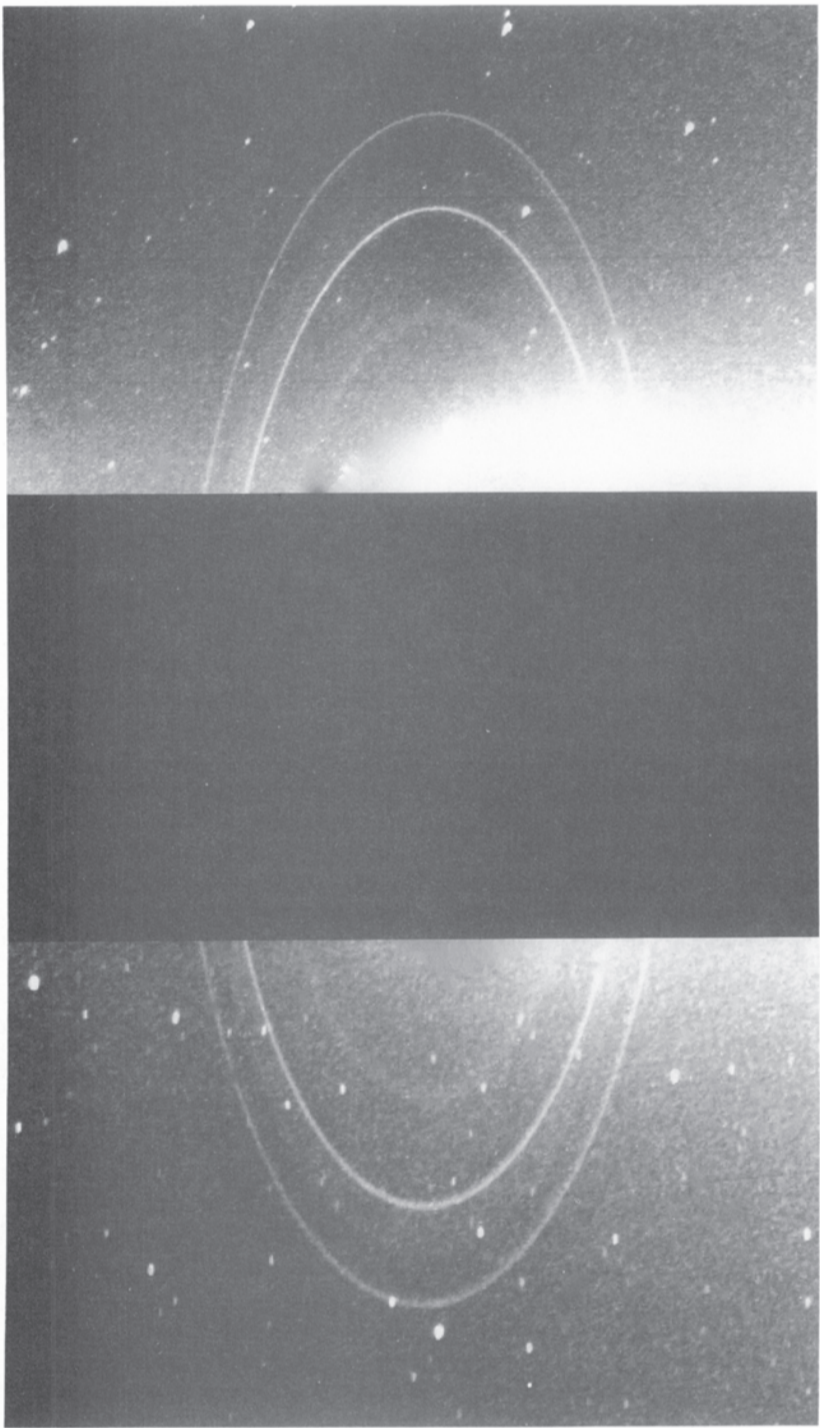


Figure 1. A pair of Voyager 591 s exposures (FDS 11446.21 and 11448.10) taken 1.5 hr apart through the clear filter of the Voyager wide angle camera at a phase angle of  $\phi \sim 134^\circ$  (figure from Smith et al. 1989). The arc region of the outermost Adams ring was not captured in either image.

Voyager images that it is unclear whether or not it is a continuous ring. Upper limits on radial widths of the narrow rings derived from Voyager images are not yet in hand. A radial width  $W \approx 110$  km has been determined from a possible detection of the Le Verrier ring in the Voyager PPS occultation scan (Sec. II.B.3).

The Neptune ring system also includes broad continuous rings. Extending out from the Le Verrier ring is the Lassell ring,  $\sim 4000$  km wide, bounded by the fourth narrow ring, Arago. Finally, the  $\sim 2000$  km wide Galle ring, at an orbital radius of 42,000 km, is the innermost of Neptune's known rings. Light from the disk of the planet scattered within the Voyager cameras during the minutes-long exposures required to see the rings prevents the unambiguous discrimination of ring material closer to the planet than Galle. Consequently, the existence of a broad sheet of dust extending inward from Galle is a possibility which cannot be confidently confirmed or refuted with the present data.

The narrowest ring structures radially resolved by Voyager instruments are the arcs within the Adams ring. The highest resolution Voyager ring image is FDS 11386.17, a narrow angle motion-compensated image retargeted to the trailing arc, Fraternité, in which the image scale is  $2.1 \text{ km pix}^{-1}$  (Table I). Unfortunately, foreshortening in the radial direction reduces the radial ring plane scale and, despite the efforts to reduce smear with motion-compensation techniques, some smear still remains. Consequently, the arc in this image, with a full width at half maximum (FWHM) brightness of 23 km (Porco et al. 1995), is likely unresolved. Smith et al. (1989) reported that the Fraternité arc imaged with the narrow angle camera in FDS 11412.46 was just barely resolved, with a radial width of  $\sim 15$  km.

The most reliable available information on arc radial widths comes from the occultation measurements, in particular the groundbased stellar occultation observations. Arc widths and normal optical depths inferred from occultation data are  $W \sim 15$  km and  $\tau_N \sim 0.1$  and are discussed in Secs. II.B.3 and II.B.4.

*2. Longitudinal Structure.* The arcs in the Adams ring, first noted in groundbased observations (Sec. II.B), are the most prominent, optically thick features within the Neptune ring system, and are clustered within a region of  $\sim 40^\circ$  in longitude (Porco 1991). Color Plate 15 is a Voyager wide angle image (FDS 11415.45) of the arc region taken at a phase angle of  $\phi \approx 135^\circ$  showing the five arcs so far observed in Voyager data; a radially averaged azimuthal scan taken through the arc region in this image is shown in Fig. 5. The zero of longitude is defined by the ascending node of Neptune's equatorial plane on the Earth's Mean Equator of 1950, and the measured longitudes have been mapped to the standard epoch of August 18, 1989, 12:00 ET, using the observed arc mean motion (see Sec. III). The center longitudes, full longitudinal lengths at half maximum brightness (FLHM) and the center-to-center separations of the arcs measured from the scan in Fig. 5 are given in Table II. [The names given by the IAU for the three arc features reported in Smith et al. (1989) are Liberté, Egalité, and Fraternité. With the discovery



Figure 2. Voyager image FDS 11404.17 taken through the clear filter of the wide angle camera from a phase angle is  $\phi \sim 135^\circ$ . The curved shadow of Neptune falls across the Le Verrier, Lassell, and Arago rings, but does not extend out to the Adams ring. Light scattered from the disk of Neptune is overexposed in the bottom portion of the frame. The bright streak on the right immediately interior to the Adams ring is Galatea smeared out by its orbital motion during this 255.36 s exposure. Close inspection reveals a distinct edge or perhaps a separate ring (Arago) forming the outer boundary of Lassell, and material in the orbit of Galatea.

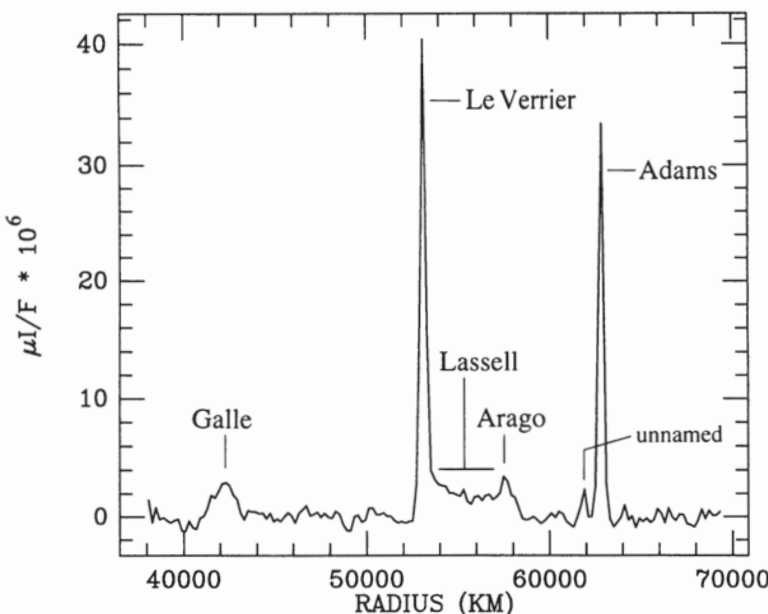


Figure 3. A radial scan of the Neptune ring system produced by azimuthally averaging the brightness along the rings in wide angle image FDS 11412.51, after the scattered light caused by Neptune-shine in the camera system was removed (figure courtesy of M. Showalter).

of two additional arcs, including the bifurcation of *Egalité* into two arcs, a temporary unofficial expanded nomenclature was adopted by Porco (1991). Since then, the IAU has assigned names to these two new arcs. The IAU names, along with the Porco (1991) designations, are shown in Table II.]

Azimuthal structure on scales smaller than the arcs'  $1^\circ$  to  $10^\circ$  lengths has also been observed (Smith et al. 1989; Porco 1991). Figure 6a is a wide angle image taken of *Fraternité*; Fig. 6b is a cartoon depicting the details seen in this image. Several long linear features are apparent in both the upper and lower portions of the image. These are believed to be discrete "clumps" or denser-than-average regions of the arc which have been trailed out by a combination of orbital motion along the ring and spacecraft motion projected across the ring. The clumps in the upper portion have typical separations of  $0.5^\circ$  to  $0.8^\circ$  and a total longitudinal extent of  $3.2^\circ$ ; the two prominent clumps in the lower portion are separated by  $\sim 1.8^\circ$ , but another clump may be present between these two. This latter group is at least  $2.6^\circ$  long; it appears to be truncated by the edge of the frame. Similar results have been found by Ferrari and Brahic (1991) for *Fraternité*. The *Liberté* arc, captured in an image taken as the spacecraft was receding from its second ring plane crossing (see Fig. 7a), also appears to be clumpy; Fig. 8 is a longitudinal scan, only one pixel wide in the radial direction, taken through the *Liberté* arc in Fig. 7a. The variations in

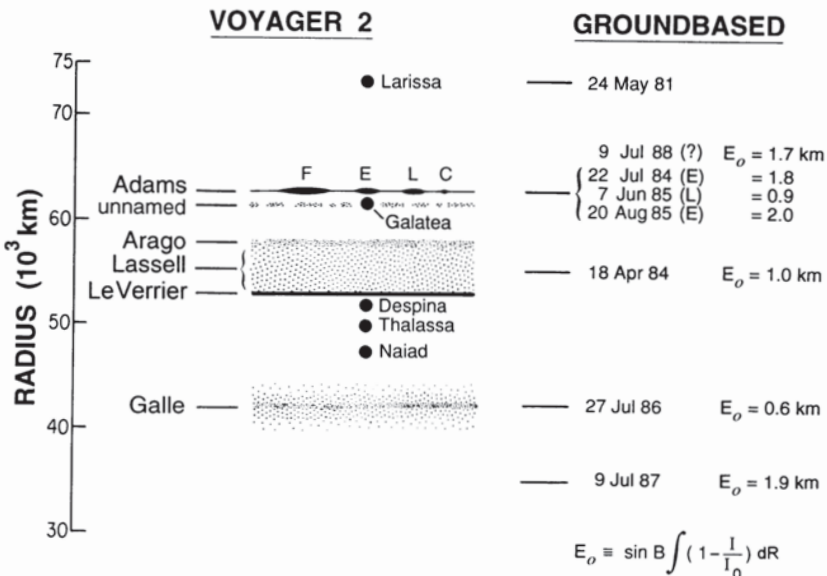


Figure 4. A diagram showing the locations of Neptune's rings and the satellites within the ring region, and the most statistically significant groundbased observations of arc-like material (and Larissa). Equivalent widths are given for groundbased observations (see Sec. II.B). The identifications (in parentheses) for the 3 reliable groundbased events which intercepted the arc region of the Adams ring assume an arc mean motion of  $820.1185^\circ \text{ day}^{-1}$ . The arcs are labeled C for Courage, L for Liberté, E for Fraternité.

brightness along the arc are statistically significant, with typical separations of  $0.4^\circ$  to  $0.6^\circ$  and a fractional amplitude of  $\sim 30\%$ . (The smear in this image is primarily perpendicular to the arcs and the clump separation measurements are not affected by it.) Finally, a single clump feature has been reported in a high-resolution image of the Courage arc (Porco et al. 1995).

The nature of these clumps is not presently clear. Smith et al. (1989) initially proposed that they may represent an accumulation of dust-sized particles around larger-than-average bodies within the arcs which provide the source of the dust through mutual vigorous collisions. This interpretation is consistent with the suggestion by Porco (1991) that the azimuthal distribution of arcs is determined by both corotational shepherding by Galatea and the libration of bigger "source" bodies around their corotation sites (Sec. IV). Another possibility offered by Porco (1991)—that the clumps are a kinematical effect created by the forced crossing of arc particle orbits near quadrature due to Lindblad shepherding by Galatea (Fig. 23 below)—appears less likely now, that clumps seem to be far more numerous than this model would predict.

On the largest azimuthal scale, the radially integrated brightness of the Adams ring is observed to vary by about a factor of 3, from a maximum near

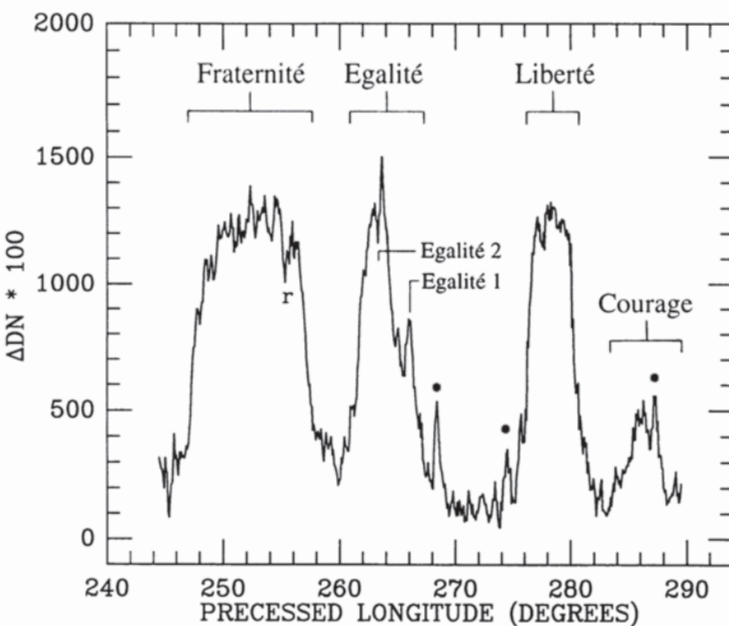


Figure 5. A radially averaged longitudinal scan of the arc region seen in Color Plate 15 and precessed to epoch August 18, 1989 under the arcs' mean motion,  $820.1185^\circ \text{day}^{-1}$ . The asterisks indicate the positions of stars; the symbol  $r$  indicates an incompletely removed camera reseau. The IAU nomenclature for all 5 arcs is shown.

and between the arcs to a minimum far from the arc region (Showalter and Cuzzi 1995). The Le Verrier ring, with no visible arcs, shows no small-scale or large-scale brightness variations.

*3. Three Dimensional Structure.* Characterizing the vertical extent of Neptune's ring system is important for understanding both the fate of small dust particles and their relationship to the extremely tilted magnetic field, and in ascertaining the processes controlling arc and dust dynamics. In general, the best images for addressing the question of vertical thickness are those acquired during the spacecraft's passage through the ring plane. Figures 7a and 7b are 2 motion-compensated 15.36 s exposures which were taken from a phase angle  $\phi \sim 155^\circ$  soon after Voyager passed through the plane of the rings (descending node) about 80 minutes after closest approach. Though radial foreshortening has compressed the entire ring system, the Galle, Le Verrier, Lassell and Adams rings can be recognized on the near arm in Fig. 7a. The viewing angle reckoned at a point on the near arm of the Le Verrier ring closest to the frame's center is  $-1.05^\circ$ , assuming the ring pole found by Porco et al. (1992) and Showalter and Cuzzi (1992b). In Fig. 7a, the Liberté arc is seen on the far arm of the Adams ring which is  $\sim 154,000$  km away and extremely compressed due to the very shallow viewing angle on this arm



of  $-0.42^\circ$ . Figure 7b was taken  $\sim 1.5$  min earlier. The viewing angle on the near arm of the Adams ring near the frame's center is  $\sim -0.53^\circ$ . Porco et al. (1995) have analyzed these images for the purpose of determining the geometry and vertical extent of the ring system. From these analyses, an upper limit of  $\lesssim 30$  km on the vertical extent of the Le Verrier and (non-arc) Adams rings was derived; for the more distant arc in Fig. 7a the limiting thickness is  $\lesssim 110$  km. These same images have provided useful information on the inclinations of the three main rings (Adams, Le Verrier and Galle) to

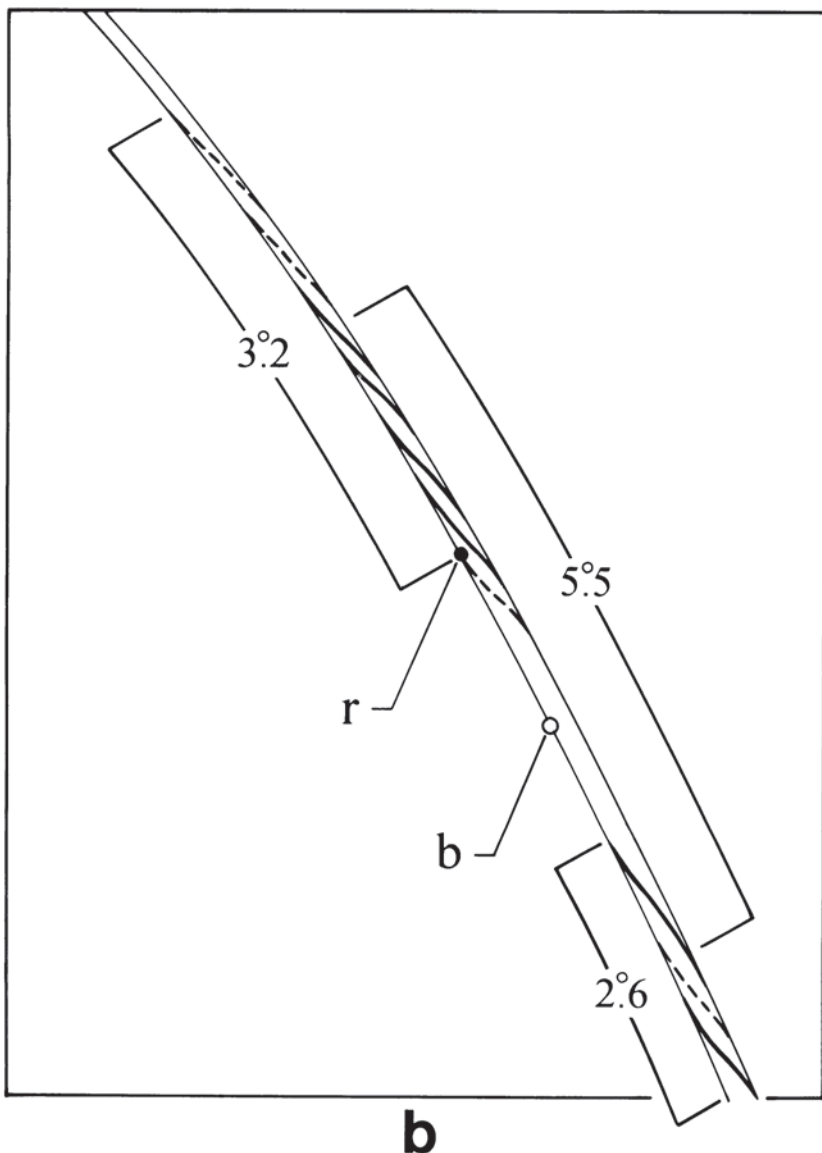
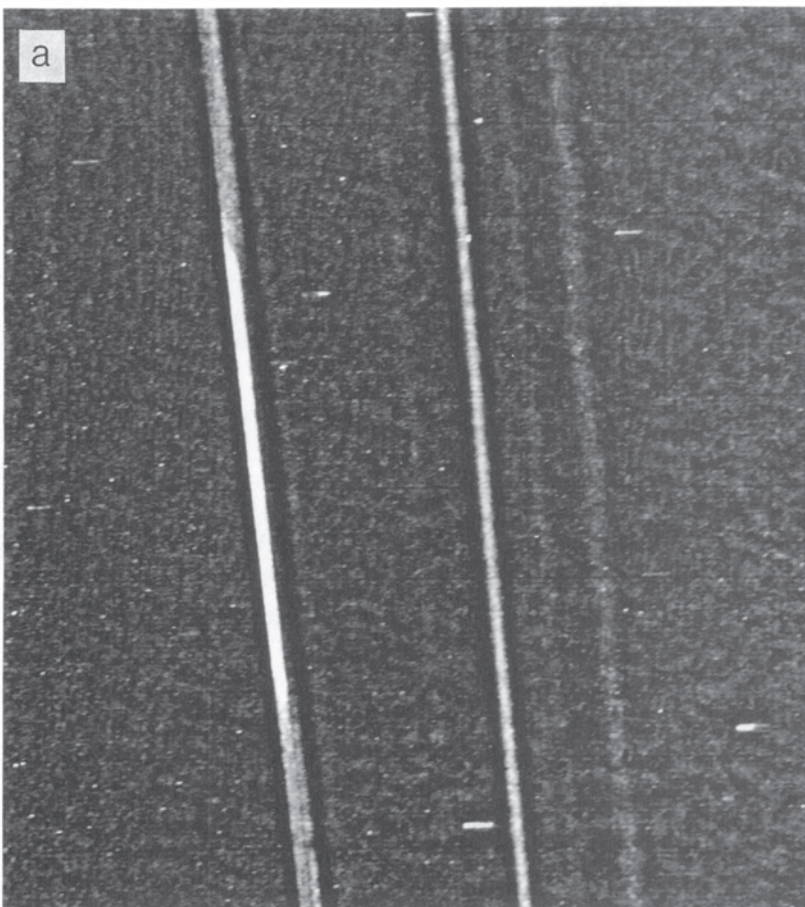


Figure 6. The complete Voyager narrow angle image FDS 11412.46 (a) showing two groups of clumps in the trailing (Fraternité) arc, and (b) a cartoon depicting the details in (a). Dashed lines indicate the presence in the image of what may be barely detectable streaked-out clumps. The symbol "r" indicates the position of a camera reseau; "b," the position of a blemish on the detector.

Neptune's nominal equatorial plane, as discussed in Sec. III.B. Information about the vertical extent of the ring system can also be obtained from *in situ* Voyager measurements of dust. These are discussed in Secs. II.A.4 and II.A.6.



*4. Ring Structure from Dust and Plasma Observations.* The Planetary Radio Astronomy (PRA) and Plasma Wave Spectrometer (PWS) experiments on Voyager provided *in situ* measurements of the distribution of microscopic dust by sensing voltage pulses produced by plasma clouds generated during particle impacts on the spacecraft (Gurnett et al. 1989; Warwick et al. 1989). The general principles used in inferring the abundance and size distribution of dust from observations of this type have been discussed by Meyer-Vernet et al. (1986), Gurnett et al. (1987, 1991), and Pedersen et al. (1991). Both experiments detect particles in two ways: direct count rates in occasional high-rate samples, and integrated mass fluxes inferred from smoothly varying antenna voltage measurements. Particles detected in these ways are in the

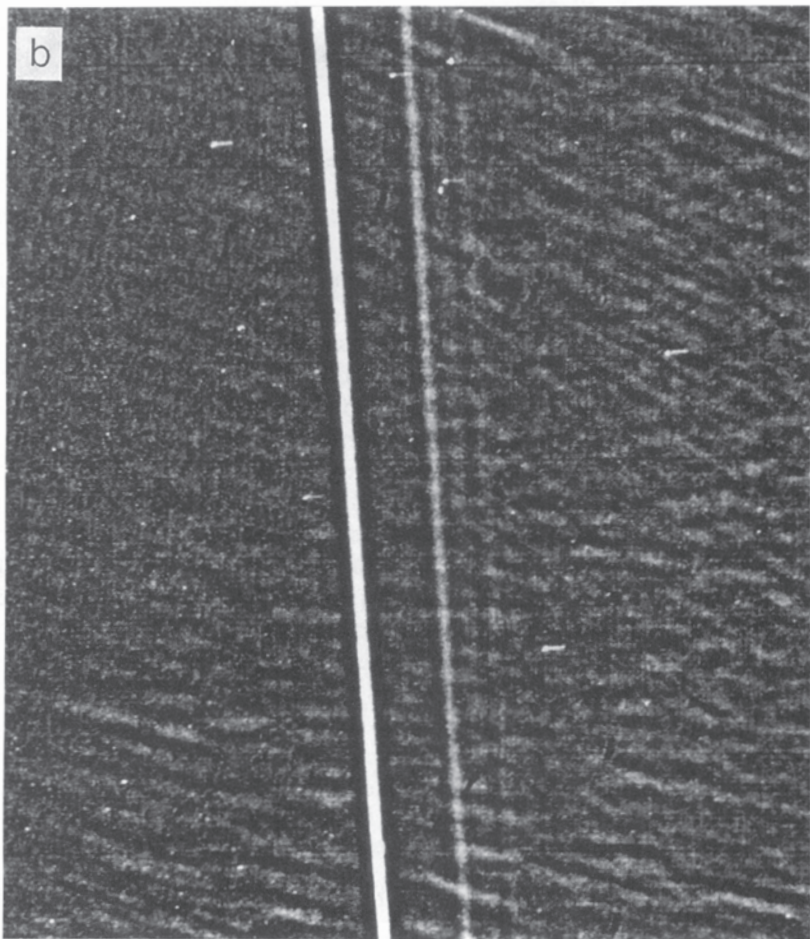


Figure 7. Two wide angle motion-compensated 15.36 s images obtained from a phase angle of  $\phi \sim 155^\circ$  as the Voyager spacecraft was receding from ring plane crossing (descending node) about 80 min after closest approach. (a) In FDS 11391.59, the spacecraft was 1100 km below the planet's equator plane (as determined by Jacobson et al. 1991) at a planetocentric latitude and distance relative to the planet center of  $-0.61^\circ$  and 106,850 km, respectively. The Liberté arc is seen on the far (left-hand side) arm of the ring system which is  $\sim 154,000$  km away and extremely compressed due to the very shallow viewing angle on this arm of  $-0.42^\circ$ ; the viewing angle on the near (right) arm is somewhat more substantial:  $-1.05^\circ$  at the Le Verrier ring. The Galle, Le Verrier, Lassell, and Adams rings can be seen. (b) Image FDS 11391.57, taken  $\sim 1.5$  min earlier than (a), when the spacecraft was 325 km below the equator at a planet-centered latitude of  $-0.21^\circ$ ; the spacecraft latitude, reckoned from the near (right) arm of the Adams ring, was  $-0.53^\circ$  and, from the near (right) arm of the Le Verrier ring, was  $-0.38^\circ$ .

mass range  $10^{-10}$  to  $10^{-8}$  g (corresponding to a radius range of 3 to 13  $\mu\text{m}$ , for a density of 1 g  $\text{cm}^{-3}$ ). These results may be divided into two spatial regimes, as noted below.

(a.) *Dust Concentrated Near the Ring Plane.* Near-equatorial dust was observed by the PRA and PWS both on Voyager's inbound and outbound trajectories (Gurnett et al. 1991; Pedersen et al. 1991). Relevant characteristics of the observations are summarized in Table III. Both PRA and PWS teams noted that the vertical and radial locations of the maximum dust density were offset from the location where the spacecraft crossed the equatorial plane of Neptune determined from the penultimate solution for Voyager's trajectory. The expected symmetry plane for particles on gravitationally dominated orbits is called the Laplace plane, and is not generally coincident with Neptune's equator plane because of perturbations from a massive, inclined Triton. This "plane"—it is actually a warped two-dimensional surface—is progressively tilted away from the planet's equator towards the orbital plane of Triton with increasing semimajor axis. The ascending node of the Laplace plane on Neptune's equator coincides with the descending node of Triton's retrograde orbit, so that it shares in the slow precession of Triton's node with a period of  $\sim 690$  yr (Jacobson et al. 1991). There is fairly good agreement between the observed location of the dust density maxima and the location of the Laplace plane calculated by Nicholson (1989; letter to members of Voyager science teams) at the times and longitudes of the two Voyager ring plane crossings. We note, however, that the Laplace plane inclinations at the spacecraft nodes ( $0.101^\circ$  inbound and  $0.276^\circ$  outbound) are comparable to the uncertainties,  $\sim \pm 0.15^\circ$ , in both the penultimate and the most recent determinations of the orientation of Neptune's equator plane (*Neptune Physical Constants, Version 8*, JPL, 11/1989; Jacobson et al. 1991). Consequently, this agreement may be fortuitous. A more careful analysis of the PRA and PWS data using the final reconstructed spacecraft trajectory might indeed provide a useful constraint on the pole of Neptune, independent of those derived from satellite and ring observations.

The results from the PRA and PWS differ in other regards, such as precise peak locations, vertical thicknesses, and dust volume number densities. For instance, the PWS observations indicate more vertically extended material than do the PRA observations, especially in the case of the outbound crossing. These differences might be due in part to variations in the size distribution of the grains (see the size distribution entry in Table III); the PWS and PRA experiments sense different moments of the particle size distribution.

The measured particle volume number densities differ as well (especially for the outbound crossing), leading to typical optical depths of  $\sim 3 \times 10^{-6}$  (inbound) and  $10^{-6}$  to  $10^{-7}$  (outbound), and typical surface mass densities of  $\sim 10^{-11}$  to  $10^{-8}$  g  $\text{cm}^{-2}$ . These quantities are inferred from the observed particle abundances and, less directly, particle sizes. These volume number and mass densities and dust optical depths are comparable to those of Saturn's G ring (Van Allen 1983; 1987; Gurnett et al. 1987; Meyer-Vernet et al.

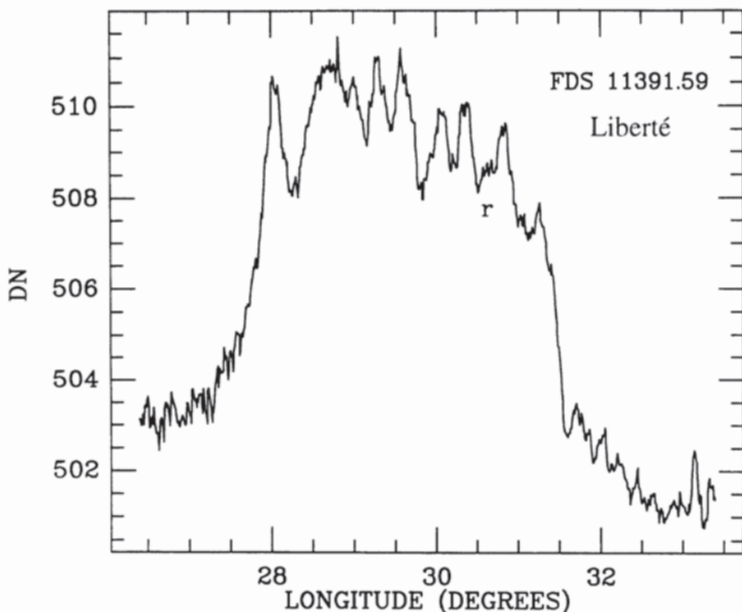


Figure 8. A longitudinal scan through the Liberté arc in Fig. 7a of one pixel width showing  $\sim 30\%$  variations in brightness of the arc with a typical spatial scale of  $0.4^\circ$  to  $0.6^\circ$ . These are similar to the clumps seen in Fig. 6 in the trailing arc.

**TABLE II**  
Arc Characteristics<sup>a</sup>

Name	Center (deg)	FLHM (deg)	Separation (deg)	Porco (1991) Designations
Courage	$285.03 \pm 0.05$	$1.0 \pm 0.1$	7.3	A1
Liberté	$277.73 \pm 0.05$	$4.1 \pm 0.1$	12.4	A2
Egalité 1	$265.4 \pm 0.5$	$1.0 \pm 0.5$	3	A3
Egalité 2	$262.6 \pm 0.5$	$3.0 \pm 0.5$	10.7	A4
Fraternité	$251.88 \pm 0.05$	$9.6 \pm 0.1$		A5

<sup>a</sup> Official IAU nomenclature, longitudinal centers, full lengths at half maximum brightness (FLHM), center-to-center arc separations, and the unofficial designations used in Porco (1991) for the five arcs within the Adams ring. Measurements taken from Fig. 5.

1986; Hood 1989; Showalter and Cuzzi 1993). Moreover, steep particle size distributions have been reported for both the G ring and the Neptune rings (Gurnett et al. 1987; Showalter and Cuzzi 1993, 1994; Pedersen et al. 1991).

**TABLE III**  
Neptune Dust Characteristics

Characteristic <sup>a</sup>	Inbound	Outbound
	PRA <sup>b</sup>	
	PWS <sup>c</sup>	
Voyager 2 crossing of Neptune equator plane <sup>d</sup>	85,290 km	103,950 km
Radial location of maximum dust density	85,400 km 85,400 km	105,500 km 104,000 km
Vertical location of maximum dust density <sup>e</sup>	+160 km +146±4 km	-700 km -948±65 km
Vertical (Gaussian half-width) of dust layer	280 km 270 km <sup>f</sup> ; 920 km	230 km 1,036 km
Grain size distribution	$dn/dm \propto m^{-2}$ ; $r_p > 1 \mu\text{m}$ $r_p \sim 5\text{--}10 \mu\text{m}$	
Optical depth	> $10^{-6}$ $4 \times 10^{-6}$	> $5 \times 10^{-8}$ $3 \times 10^{-6}$
Surface mass density ( $\text{g cm}^{-2}$ )	> $2 \times 10^{-10}$ $\sim 10^{-8}$	> $10^{-11}$ $\sim 10^{-8}$
Maximum number density ( $\text{cm}^{-3}$ )	$\sim 2 \times 10^{-7}$ $\sim 10^{-8}$	$\sim 2 \times 10^{-8}$ $\sim 10^{-9}$
Halo radial [vertical] extents ( $R_N$ ) <sup>g</sup>	1.6–6.5 [2] All regions inside 8 [2]	3–6.2 [2]
Halo number density ( $\text{cm}^{-3}$ ) (PWS only)	$10^{-10}\text{--}10^{-12}$	

<sup>a</sup> All vertical dimensions referenced to the Neptune equatorial plane (*Neptune Physical Constants, Version 8*, JPL, 11/1989).

<sup>b</sup> Pedersen et al. (1991).

<sup>c</sup> Gurnett et al. (1991).

<sup>d</sup> Stone and Miner (1991).

<sup>e</sup> Calculated vertical locations of Laplace plane relative to Neptune equator plane (Nicholson, letter to members of Voyager science teams, 1989); +150 km (inbound) and -500 km (outbound).

<sup>f</sup> The PWS experiment measured on inbound *two* distinct Gaussian distributions having different half-widths.

<sup>g</sup> 1  $R_N = 24,762 \text{ km}$ .

(b.) *High Latitude Dust.* The PRA and PWS teams also report a noticeable abundance of small grains at large distances from the ring plane. The dust volume number densities at these high latitudes are several orders of magnitude smaller than those observed close to the Laplace plane (Table III). Inspection of the results presented by both teams reveals some structure in the distribution of this vertically extended dust (Gurnett et al. 1991, fig. 2; Pedersen et al. 1991, fig. 1). Some of this structure might be related to the location of the magnetic equator (Pedersen et al. 1991): electromagnetic forces acting on charged grains could generate such large vertical excursions. Alternatively, these data might indicate the existence of polar rings tenuous

enough to have escaped detection in Voyager imaging data (Sec. II.A.5).

*5. Polar Rings.* The possible existence of polar rings around Neptune was first suggested by Dobrovolskis (1980). In the usual circumstance of an oblate planet with no large inclined moon, minima in the Hamiltonian or total energy for the orbit normal of a ring particle lie near the planet's poles. The poles of near-equatorial rings (either prograde or retrograde) precess about these polar minima. The presence of massive Triton in a significantly inclined orbit has two modifying effects: (1) the stable near-equatorial orbits are shifted into the Laplace plane, whose pole is intermediate between the planet's spin axis and Triton's orbit normal (see Sec. II.A.7); and (2) two new maxima are introduced in the Hamiltonian of the system, both of which lie near the node of Triton's orbit on the equatorial plane of Neptune. Dobrovolskis showed that, because orbit pole libration trajectories are curves of constant total energy encircling *any* extremum, polar rings could exist with poles lying near to, but not exactly at, these nodes. Initial objections to polar rings based on the expected energy damping in the presence of interparticle collisions, and the attendant evolution of the poles away from the energy maxima, were countered by Borderies (1989) and Dobrovolskis et al. (1989a, b), who showed that energy loss decreases the ring particles' semimajor axes without altering their orbit poles. Such rings are consequently stable, although their poles will precess slowly about Neptune's pole, tracking the node of Triton's orbit on the planet's equatorial plane, but with a slight phase lag. No other outer planet has a sufficiently large and inclined satellite to cause the requisite distortion of the curves of constant total energy. Polar rings have been studied in the context of galactic dynamics, and several good examples have been observed (see, e.g., Athanassoula and Bosma 1985).

The range of particle orbits most congenial to stable polar rings is between  $\sim 5 R_N$  and  $\sim 10 R_N$ , where  $1 R_N = 25,000$  km. In this region, the Laplace plane shifts from being almost coincident with Neptune's equator plane to lying essentially in Triton's orbit plane. The exact orientation of stable polar rings varies in node and inclination with distance from the planet, with prograde and retrograde rings lying in slightly different planes (Dobrovolskis 1980; Borderies 1989; Dobrovolskis et al. 1989a, b).

Dobrovolskis (1980) suggested that tidal disruption of a moon on a near-polar orbit could lead to the formation of a polar ring, citing the unusual orbits of Triton and Nereid as support for this possibility. The increasing realization of the importance of recent *collisional* disruption in the ring systems of the giant planets (see, e.g., Smith et al. 1981, 1982, 1986, 1989; Esposito and Colwell 1989; Colwell and Esposito 1990a, b, 1992a) demanded serious consideration of this possibility in the planning of Voyager ring imaging sequences. On its inbound trajectory through the Neptune system, the Voyager spacecraft flew nearly parallel to the polar ring planes described by Dobrovolskis (1980); Dobrovolskis et al. 1989a, b) and Borderies (1989, figs. 4 and 5). During this period, Voyager imaging observations were targeted to search for material in these planes, the spacecraft view of which would have been no more than

10 to 20° from edge-on. Several of the best Voyager images taken during this period show no evidence of ring material above the level of the noise. The upper limiting optical depth is  $\sim 10^{-5}$  (Smith et al. 1989). However, further image analysis might profitably be done in light of the dust detected by Voyager at high inclinations (Sec. II.A.4).

*6. Ring Structure from Charged Particle Absorptions.* Jupiter's ring was first detected by its depletion of the Jovian magnetosphere (Acuña and Ness 1976); particulate material has been detected in a similar manner at a variety of places in the Saturn system (see, for a review, Van Allen [1984], especially his Table II). The overall situation at Neptune is reviewed by Mauk et al. [1991; see especially their figs. 10 and 11], Paranicas and Cheng [1991], and in the Chapter by Mauk et al. In general, one expects that for an offset, tilted dipole field, material in eccentric orbits will deplete charged particles in four distinct corotating magnetospheric regions: two where the offset field samples apoapsis and two where periapsis is sampled (cf., also Paonessa and Cheng 1987). Unfortunately, the magnetic fields of Uranus and Neptune are more strongly tilted and offset than Jupiter's (and far more complex than Saturn's neatly aligned dipole), making it difficult to associate observed magnetospheric depletions with orbiting material at specific radial locations. Further complications arise from the fact that the spacecraft sampled only one trajectory in this complex, three-dimensional, time-varying environment.

Several workers have reported a magnetospheric absorption in the orbit of Proteus (see Mauk et al. 1991; Selesnick and Stone 1991, 1992). Selesnick (1992) has utilized the Proteus absorption signature to constrain several parameters of the standard "O8" magnetic field model (Connerney et al. 1991). More recently, Selesnick (see, e.g., the Chapter by Mauk et al.) has modeled the diffusion coefficients of electrons and relevant ion species; the absorptions in the orbit of Proteus can apparently be explained by the sweeping action of Proteus itself, and no additional co-orbiting material is needed. This recent work addresses concerns formerly raised by Cheng et al. (1992).

Paranicas and Cheng (1991) point out that the Neptunian ring system should be more effective as an absorber than the inner Neptunian satellites. Mauk et al. (1990, 1991) discovered one distinct region of depletion of ions and electrons with near-equatorial gyrations (a "90 degree pitch-angle bite-out"), as well as discrete absorption signatures at locations connected with orbital radii in the general vicinity of the Galle ring. The region of pitch-angle-dependent depletion does straddle the magnetic equator, indicating that electromagnetic effects rather than particulate absorption might be responsible in this case (Chapter by Mauk et al.). Mauk et al. (1992) believe that evidence for depletion by the Adams ring is to be found in an absorption at 0323 UT on August 25, 1989; figs. 10 and 11 of Mauk et al. (1991) indicate another possible absorption associated with the Adams ring near 0439 UT. These unique observations are worthy of closer scrutiny and may yield independent information on particle volume number densities in the vicinities of these rings, as well as improved constraints on the magnetic field.

*7. Small Satellites Associated with the Rings.* A total of six small inner satellites of Neptune were discovered in Voyager images, five of which orbit interior to the synchronous distance and four within the ring system itself (Smith et al. 1989). Similar retinues of small "ring moons" orbit Jupiter (Synnott 1984), Saturn (Synnott et al. 1981; Yoder et al. 1989; Showalter 1991), and Uranus (Owen and Synnott 1987). Because of the large number of images available, spanning a period of almost three months, the orbits of all six satellites are unusually well-determined (Owen et al. 1991). Many of these images were taken in deliberate searches either for the ring arcs or for small satellites, so the coverage is particularly complete. The principal characteristics of these bodies are summarized in Table IV, based on the orbit determinations by Owen et al. (1991). Mean radii are taken from the companion Chapter by Thomas et al., to which the reader is referred for further details on the physical properties of these satellites.

Especially noteworthy for our purposes is the close proximity of Galatea to the Adams ring (mean separation 980 km), and Despina to the Le Verrier ring (mean separation 674 km). In each case, the satellite is found interior to the ring. Thalassa and Naiad orbit in the wide gap between the Le Verrier and Galle rings, but well removed from both (see Fig. 4). For any reasonable density, the four inner moons are interior to their Roche limits (see the Chapter by Lissauer et al.). The orbits of all six moons have small eccentricities ( $\lesssim 10^{-3}$ ) and five have inclinations ( $0.04\text{--}0.20^\circ$ ) comparable to those of the inner satellites of Uranus (Owen and Synnott 1987) and of the Uranian rings (French et al. 1988). An interesting exception is the  $4.7^\circ$  inclination of Naiad, which may be a remnant of passage through a mean-motion resonance with Despina (Banfield and Murray 1992). Similar resonances are, or may have been in the past, responsible for the inclinations of Mimas ( $1.5^\circ$ ) and Miranda ( $4.4^\circ$ ) (Sinclair 1972; Tittemore and Wisdom 1989; Dermott et al. 1989).

The inclinations listed for the satellites in Table IV are calculated relative to the Laplace plane at the satellite's orbit. Full expressions for the orientation of the Laplace plane are given by Owen et al. (1991), who calculated the inclinations of the Laplace plane for each satellite relative to Neptune's equator,  $i_L$ , also given in Table IV. In determining the absolute orientation of the Laplace plane in space, Owen et al. adopted the precessing Neptune pole model of Jacobson et al. (1991), which is based on a combination of Earth-based observations of Triton and Voyager optical and radio navigation data.

For small deviations from the equatorial plane, appropriate for mean distances  $a \lesssim 6 R_N$ , the inclination of the Laplace plane relative to the planet's equator is given approximately by (Dobrovolskis 1980):

$$\sin i_L \simeq \frac{\dot{\Omega}_T \sin i_T}{\dot{\Omega}_N + \dot{\Omega}_T - \dot{\eta}} \quad (1)$$

TABLE IV  
Orbits of Neptune's Small Satellites<sup>a</sup>

Name	Proteus	Larissa	Galatea	Despina	Thalassa	Naiad
IAU designation	1989N1	1989N2	1989N4	1989N3	1989N5	1989N6
$a_{\text{calc}}$ (km)	117647.1	73548.3	61952.7	52526.0	50074.6	48227.3
$n_s$ ( $d^{-1}$ ) <sup>b</sup>	320.7654	649.0534	839.6598	1075.7342	1155.756	1222.844
$e$	0.0004	0.0014	0.0001	0.0001	0.0002	0.0003
$i$ ( $^{\circ}$ ) <sup>c</sup>	0.04	0.20	0.05	0.07	0.21	4.74
$d\omega/dt$ ( $^{\circ}d^{-1}$ )	0.0789	0.3931	0.7160	1.2768	1.5099	1.6991
$d\Omega/dt$ ( $^{\circ}d^{-1}$ )	-0.0773	-0.3922	-0.7148	-1.2749	-1.5076	-1.7141
$i_L$ ( $^{\circ}$ ) <sup>d</sup>	0.5475	0.0479	0.0197	0.0084	0.0066	0.0054
$\langle R \rangle$ (km)	208	96	74	79	[40] <sup>e</sup>	[29] <sup>e</sup>

<sup>a</sup> Owen et al. (1991).

<sup>b</sup> Sidereal mean motion.

<sup>c</sup> Inclination relative to Laplace plane.

<sup>d</sup> Laplace plane inclination relative to Neptune's equatorial plane.

<sup>e</sup> Radius calculated from observed brightness and an assumed geometric albedo,  $p = 0.06$  (see the Chapter by Thomas et al.).

where

$$\dot{\Omega}_T = -\frac{1}{4} \frac{m_T}{M_N} \beta^2 b_{3/2}^{(1)}(\beta) n \quad (2)$$

is the contribution to the nodal regression rate at distance  $a$  due to Triton, with  $\beta = a/a_T$ ,  $\dot{\eta} = +0.52^\circ \text{yr}^{-1}$  is the nodal precession rate of Triton's orbit (Jacobson et al. 1991),  $n$  is the orbital mean motion of the test particle, and

$$\dot{\Omega}_N \simeq -\frac{3}{2} J_2 (R_N/a)^2 n \quad (3)$$

is the nodal regression rate at  $a$  due to Neptune's oblateness. The function  $b_{3/2}^{(1)}(\beta) \simeq 3\beta + O(\beta^3)$  is a Laplace coefficient (Brouwer and Clemence 1961). The mass, orbital semimajor axis and inclination of Triton are denoted by  $m_T$ ,  $a_T$  and  $i_T$ , respectively. From these expressions, we find values of  $i_L = 0.023^\circ$  at the Adams ring and  $0.010^\circ$  at the Le Verrier ring. These small corrections must be taken into account if the rings are used in the future to infer an improved Neptune pole direction.

Of particular importance to dynamical studies of the rings is the fact that the inner satellites' orbit planes, in combination with observations of the rings themselves, may eventually provide the most accurate determination of the orientation of Neptune's equatorial plane, independent of that derived from observations of Triton or Voyager navigation (Jacobson et al. 1991). The instantaneous satellite orbit poles determined by Owen et al. (1991) from Voyager data are (except for Thalassa and Naiad) generally accurate to  $\sim \pm 0.015^\circ$ , which is approximately ten times better than the accuracy with which Neptune's pole is known (Jacobson et al. 1991). (This implies that there are undoubtedly errors in the tabulated satellite inclinations attributable to errors in the planetary reference pole.) In fact, a comparison of the orbit pole of Galatea with that determined for the Adams ring by Porco (1991), for the Le Verrier ring by Showalter and Cuzzi (1992b) and Porco et al. (1992), and for the Galle ring by Showalter and Cuzzi (1995), shows a tight cluster offset  $\sim 0.06^\circ$  to the east of the nominal Neptune pole (Porco et al. 1995). This suggests strongly that an average of these three ring poles, corrected for the Laplace plane offsets, may provide the most accurate estimate of the true Neptune pole direction.

## B. Occultation Observations

Occultation measurements have proven to be a powerful tool in deciphering details of ring radial structure, in defining ring orbits, and (in the case of spacecraft radio occultations in particular) in determining the particle size distribution. Occultation studies of the Saturnian and Uranian ring systems are reviewed by Cuzzi et al. (1984), Esposito et al. (1984, 1991), and French et al. (1991). However, occultation observations, by their very nature, are limited in azimuthal coverage and to ring regions of moderate to high optical depth, roughly in the range  $0.01 < \tau < 5$ . At lower optical depths, such as those

of the tenuous Jovian rings, the Saturnian E and G rings, and the broad dusty bands in the Uranian system ( $10^{-6} < \tau < 10^{-4}$ ), the attenuation of the stellar or radio beam is negligible and the rings are generally undetectable.

The Neptunian rings fall in an intermediate category, posing unique difficulties to occultation studies. Although the arcs within the Adams ring, with typical optical depths of  $\sim 0.1$ , were first detected in Earth-based stellar occultations, the lower optical depth continuous regions of the Adams and Le Verrier rings apparently fall just at or below the threshold for stellar or radio occultation observations. Moreover, the limited azimuthal extent of the arcs ( $\sim 5\%$  of the total circumference of the Adams ring) combined with uncertainties in the predicted occultation tracks, further reduce the opportunity for successful measurements. The entire data base of Earth-based occultation measurements for the Neptunian rings, despite a decade of intensive observations, has thus yielded only three, and possibly four, detections of the Adams ring arcs, and one marginal detection of the Le Verrier ring. In addition the Voyager PPS and UVS experiments recorded a single stellar occultation profile of the Liberté arc, and may also have detected the Le Verrier ring. These data, while meager, provide the best estimates of arc widths and optical depths, restrictive upper limits on the radially integrated optical depths of the continuous rings, and (together with Voyager imaging data) an accurate determination of the arcs' mean motion (Sec. III).

In this section we first review the Earth-based observations of the arcs and the accompanying limits on the continuous rings, then describe the Voyager observations, and finally provide a summary of ring and arc physical and geometric parameters derived from the occultation data. We begin, however, by introducing some necessary terminology, to be used throughout this section. Parts of this discussion are drawn from the review by French et al. (1991), and based on treatments by Elliot et al. (1984), Holberg et al. (1987) and Sicardy et al. (1991).

Because of the combined effects of diffraction and finite stellar angular diameter, Earth-based occultation profiles of narrow rings or arcs are controlled primarily by the radially integrated fraction of starlight blocked by the ring, and generally do not resolve structure in the ring below a resolution limit of a few to ten kilometers. Typical Fresnel zones for Earth-based occultations by the Neptunian rings observed at a wavelength of  $2.2 \mu\text{m}$  are  $\sqrt{2\lambda D} \simeq 4.4 \text{ km}$ , where  $\lambda$  is the wavelength of light, and  $D$  is the distance to the planet from the observer. Projected stellar diameters range from 1 to 15 km. The most direct measure of total light removed from the incident stellar beam by a ring is the equivalent width, defined by Elliot et al. (1984) and Holberg et al. (1987) as

$$E_o = \mu \int [1 - I(R)/I_0] \, dR \quad (4)$$

where  $I(R)/I_0$  is the normalized attenuated stellar flux,  $R$  denotes radius in the ring plane and  $\mu = \sin B$ , where  $B$  is the inclination of the ring plane to

the line of sight (typically  $B \simeq 20^\circ$  for Earth-based Neptune occultations). The factor of  $\mu$  is introduced to correct approximately for the effect of varying incidence angle on the observed ring transmission. The subscript 0 is used here to denote an occultation-derived equivalent width, to distinguish this quantity from the analogous integrated ring brightness derived from imaging data,  $E_i$ , introduced in Sec. II.C below.

The equivalent width is *independent* of the smearing effects of diffraction and stellar angular diameter, and whether or not the ring is partially resolved, making it the most reliable quantitative characteristic of a ring occultation observed from Earth. For a narrow ring of radial width  $W$  and uniform line-of-sight transmission  $f_0$

$$E_o = \mu W(1 - f_0) = \mu W(1 - e^{-\tau/\mu}) \quad (5)$$

where we have introduced the normal optical depth,  $\tau = -\mu \ln f_0$ . Note that it is possible to determine the equivalent width of an unresolved ring or arc from Eq. (4), even if the actual width  $W$  and transmission  $f_0$  are indeterminate. The equivalent widths derived from Earth-based observations of the Neptunian arcs, listed in Table V below, range from 0.9 to 2.0 km. For the nine major Uranian rings,  $E_o$  ranges from a minimum of 0.7 km for rings  $\eta$  and 6 to a maximum of 60 km for the  $\epsilon$  ring at apoapse (French et al. 1986).

In the case of well-resolved rings, where the internal structure is visible and can be used to calculate the radial optical depth profile  $\tau(R) = -\mu \ln f_0(R)$ , it is possible to determine the radially integrated normal optical depth, or equivalent depth:

$$A = \int \tau(R) dR = -\mu \int \ln f_0(R) dR. \quad (6)$$

The equivalent depth is most readily determined from spacecraft occultation data, in which the smearing effects of diffraction and stellar diameter are negligible. For a narrow ring of uniform transmission  $f_0 = e^{-\tau/\mu}$ , we have

$$A = W\tau = -\mu W \ln f_0. \quad (7)$$

Using this expression, the equivalent depth may be estimated from square-well diffraction model fits to groundbased occultation profiles, where now  $W$  is the best-fitting radial width of the ring and  $f_0$  is the fitted transmission (French et al. 1986). For further discussion of the relation between  $E_o$  and  $A$ , and the motivation behind their specific definitions, the reader is referred to the review by French et al. (1991). For our present purposes, we are concerned only with rings and arcs for which  $\tau << 1$ , so that Eqs. (5) and (7) imply that  $E_o \simeq A = W\tau$ . This approximation leads to an underestimate of  $\tau$  by  $\lesssim 15\%$  for typical Neptune arc/ring values of  $\tau \lesssim 0.10$  and  $\mu = 0.3$ . Although we will use the correct terms here, for most practical purposes  $E_o$  and  $A$  may be treated interchangeably in the case of Neptune.

**TABLE V**  
Summary of Reported Neptune Ring and Arc Occultations

Date/Expt. <sup>a</sup>	JED <sup>b</sup>	Radius <sup>c</sup>	Radius <sup>d</sup>	$\lambda^e$	$\lambda_0^f$	$E_o$ [A] <sup>g</sup>
Adams Ring Arcs						
8/20/85	6297.61661	62857±53	63011	36.61°	263.93°	1.95
7/22/84*	5903.56715	[65300]	[65300]	151.6°	265.95°	1.79
6/07/85	6224.23845	62900±27	62944	349.19°	275.29°	~0.9
7/09/88+	7351.70768	63170±28	63204	171.60°	279.33°	1.7±0.3
PPS	7763.47618	62818±10	62904	191.14°	279.90°	0.77±0.13
UVS	7763.47617	62825±10	62911	191.15°	279.91°	0.66±0.12
Date/Expt. <sup>a</sup>	JED <sup>b</sup>	Radius <sup>c</sup>	Radius <sup>d</sup>	$\lambda^e$	$W^i$	$E_o$ [A] <sup>g</sup>
Le Verrier Ring						
8/20/85	6297.54027	52929±35	53055	194.04°	135	052±0.06
PPS	7763.49306	53070±20	53125	180.63°	113	0.70±0.20

Data <sup>j</sup>	JED <sup>b</sup>	Radius <sup>c</sup>	$\lambda^e$	Other Features	$W^i$	$E^g$	Comments
4/18/84	5808.72961	55192±40	181.63°		9.4	1.03	within Lassell
7/27/86I	6638.72900	42265±13	357.09°	<16	~0.6		within Galle ring?
7/27/86P	6638.72745	42172±13	357.22°	4.5	~0.6		
6/22/87	6968.6180	245800			10.1	0.6	near Triton's orbit
7/09/87P	6985.68423	35226±31	141.06°	~25	1.8		interior to Galle ring
7/09/87M	6985.68383	35185±30	142.45°	~9	1.9		

+ This feature may not be part of the Adams ring.

\* The astrometry for this event is uncertain:  $R = 65,300 \pm 3,000$  km,  $144.5^\circ \leq \lambda \leq 154.5^\circ$ .

<sup>a</sup> PPS = Voyager Photopolarimeter Subsystem; UVS = Voyager Ultraviolet Spectrometer.

<sup>b</sup> Julian ephemeris date at Neptune—244 0000.

<sup>c</sup> Radius calculated with the Jacobson et al. (1991) Neptune pole; uncertainties are exclusive of pole errors.

<sup>d</sup> Radius calculated with the Adams ring pole (Porco 1991).

<sup>e</sup> Longitude measured from the ascending node of the ring plane on the Earth's mean equator of 1950.0.

<sup>f</sup> Longitude precessed to epoch (JED 244 7757.0), for an assumed mean motion of  $820.1185^\circ \text{ day}^{-1}$ .

<sup>g</sup> Equivalent width ( $E_o$ , km) for Earth-based events, or equivalent depth ( $A$ , km) for Voyager events. See text for definitions.

<sup>h</sup> Radius calculated using the Le Verrier ring pole (Porco et al. 1992; Showalter and Cuzzi 1992b).

<sup>i</sup> Estimated radial width (km).

<sup>j</sup> Station codes: P = Palomar; I = IRTF; M = MMT.

In comparing occultation-derived optical depths with information obtained from images, or even in comparing Earth-based and spacecraft occultation data, it is necessary to take into account the effective “occultation” efficiency  $Q_{\text{occ}} = \sigma/\sigma_g$ , where  $\sigma$  is the occultation extinction cross section for a typical ring particle and  $\sigma_g = \pi r^2$  is its geometric cross section (Cuzzi 1985) with  $r$  equal to the particle’s radius. In general,  $\sigma$  is dependent on both the particle size and the particular experimental geometry. Given a differential particle size distribution  $n(r)$ , integrated normal to the ring plane, the normal occultation optical depth at wavelength  $\lambda$  is given by

$$\tau(\lambda) = \int n(r) Q_{\text{occ}}(r, \lambda) \pi r^2 dr. \quad (8)$$

If all the light absorbed and scattered by the particle is completely removed from the incident beam, we may write  $Q_{\text{occ}} = Q_{\text{ext}}$ , the particle’s extinction efficiency. For particles which are very large compared with the wavelength of observation,  $Q_{\text{ext}} \approx 2$ , where the factor of 2 arises because the amount of light diffracted by the particle out of the direct beam into a narrow cone of angular width  $\theta_d \approx \lambda/2r$  is equal to that which is geometrically intercepted. For particle sizes  $r \lesssim \lambda$ , the relationship between  $Q_{\text{ext}}$  and particle radius is complicated and must be derived using Mie theory or its variants (van de Hulst 1981).

However, in situations where either the projected angular width of the ring at the observer,  $\theta_{\text{ring}} \gtrsim \theta_d$ , starlight is diffracted by nearby particles into the detector and this extra light can exactly replace the light removed by diffraction from the direct beam. (This is strictly true only when  $\theta_{\text{ring}}$  is also smaller than the acceptance cone of the detector.) In this case,  $Q_{\text{occ}} \approx 1$  for particles with  $r \gg \lambda$  (Cuzzi 1985). Analysis of occultation data for the narrow Uranian rings has shown clearly that, as anticipated for rings composed primarily of centimeter- to meter-sized particles (Ockert et al. 1987; Espaço et al. 1991),  $\theta_{\text{ring}} \gtrsim \theta_d$  and  $Q_{\text{occ}} \approx 1$  for the Voyager stellar occultation experiments, while  $\theta_{\text{ring}} < \theta_d$  and consequently  $Q_{\text{occ}} = 2$  for Earth-based occultations (Holberg et al. 1987; French et al. 1991). In fact, Holberg et al. used the observed ratios of Earth-based to Voyager optical depths to set a lower limit on the average radius of particles in the  $\epsilon$  ring of  $r \approx \lambda/2\theta_{\text{ring}} \approx 0.3$  cm. The narrower  $\gamma$  and  $\delta$  rings yielded even larger lower limits on the mean particle sizes. A similar situation holds for observations of reflected sunlight from the rings, where the angular extent of the source  $\theta_s \gtrsim \theta_d$  and the narrow cone of diffracted light is indistinguishable from the unscattered beam; it is common in this context to ignore the highly forward scattered light and to assume  $Q = 1$  for particles with  $r \gg \lambda$ . In this case it is also necessary to adjust the phase function to exclude the diffracted light component.

Note that  $Q_{\text{occ}} \approx Q_{\text{ext}} < 1$  for  $r < \lambda$ , so very small particles do not contribute significantly to the optical depths measured in occultation experiments. There are thus three important regimes of particle size for occultations by point

sources, which are dependent on the experimental geometry as well as the wavelength of observations: (i)  $r < \lambda$  with  $Q_{\text{occ}} < 1$ ; (ii)  $\lambda \leq r \leq \lambda/2\theta_{\text{ring}}$  with  $Q_{\text{occ}} \approx 2$ ; and (iii)  $r \geq \lambda/2\theta_{\text{ring}}$  with  $Q_{\text{occ}} \approx 1$ .

For the Neptunian rings, we again expect that  $Q_{\text{occ}} = 2$  for Earth-based occultation data, so long as the mean particle size is substantially larger than the wavelength of observation ( $2.2 \mu\text{m}$ ). For the Voyager stellar occultations, however, the situation is more problematic. At a distance of  $3.3 \times 10^5 \text{ km}$  and a typical arc width of 15 km, only for ring particles larger than  $\sim 1 \text{ cm}$  do we expect to find  $Q_{\text{occ}} \approx 1$  for the PPS or UVS occultations for which  $\lambda \approx 0.2 \mu\text{m}$ . For particle radii less than  $\sim 0.3 \text{ cm}$  but much larger than the wavelength, we find that  $Q_{\text{occ}} \approx 2$ . In fact, photometric observations suggest that most Neptunian ring particles are sub-centimeter in size (see Sec. II.C), so that we have  $Q_{\text{occ}} \approx 2$ . The situation is thus in marked contrast to that which obtains for the Uranian rings. This is at variance with the interpretation of the PPS data by Horn et al. (1990), who assume that  $Q_{\text{occ}} = 1$ .

Although some authors have corrected for the effective occultation efficiency by reporting "geometric" or "diffraction-corrected" values of ring optical depth or equivalent depth, i.e.,  $\tau_g = \tau/2$  or  $A_g = A/2$  (Holberg et al. 1987; Sicardy et al. 1991), we prefer here to quote the *actual measured values*, and to account explicitly for  $Q_{\text{occ}}$  when comparing occultation and imaging results in Sec. II.C. Any corrected values will be explicitly denoted  $\tau_g$  or  $A_g$ .

*1. Earth-based Arc Observations.* Dates, observing sites, and references for the 30 Earth-based Neptune occultations known to have been successfully observed to date are listed in Table VI. A cross ( $\times$ ) in this table identifies those events for which an occultation potentially due to circum-Neptune material was observed, with an asterisk indicating the four occasions on which such a secondary feature was observed at two or more telescopes. The probable identifications of these events with the known components of Neptune's visible ring system are indicated in Fig. 4, including the chance occultation of satellite Larissa = 1989N2 = 1981N1 on May 24, 1981 (Reitsema et al. 1982; Smith et al. 1989). With only very few exceptions, Earth-based occultation measurements have been made at an effective wavelength of  $2.2 \mu\text{m}$ . Table V summarizes the principal characteristics of the reported occultation detections of either rings or arcs in the Neptune system, grouped by the ring with which each feature has been identified (see Fig. 4). Included here are the Voyager occultations discussed in Sec. II.B.3.

Figure 9 illustrates the sky plane trajectories for those Earth-based Neptune stellar occultations showing events thought to be caused by ring or arc material, while Fig. 10 shows the occultation profiles for the four events associated with the Adams ring arcs. The geometry of the first confirmed arc observation on July 22, 1984 is shown in Fig. 9a; the apparent path of the star just missed the northern limb of Neptune. Because of this unfortunate circumstance the reconstruction of the occultation geometry is uncertain and the radius of the feature in Neptune's equatorial plane remains poorly known.

**TABLE VI**  
Neptune Stellar Occultations: 1968 to 1992

Star ID <sup>a</sup>	Date	K mag. <sup>b</sup>	Stations <sup>c</sup>	Events <sup>d</sup>	References <sup>e</sup>
N23	4/07/68	10.6	MSO, Japan (2)	—	FL70, KL69
N28	8/21/80	5.9	MSO	x	NJ80
N28	5/10/81	—	MSO, AAO, IRTF, UH	—	E81
N29	5/24/81	—	CTIO	—	E81
N29	5/24/81	9.7	CAT, ML	—	R82, H86b
N30	6/15/83	6.9	KAO, IRTF, UH, AAO	—	E85
			Australia (2), Taiwan	—	H85
			CFH	—	S91
n84-62	4/18/84	9.6	PAL	x	N90
n84-70	5/11/84	8.2	PAL	—	N90
N34	7/22/84	4.2	CTIO, ESO	*	H86a, S91
N36	6/07/85	8.8/9.4	SAAO	x	C86
n85-06	6/25/85	10.3	SAAO	—	C86
n85-34	7/30/85	12.4	PAL, IRTF	—	N90
n85-38	8/10/85	11.0	IRTF	—	N90
n85-39	8/20/85	5.9	IRTF, LOW, MWO	*	N90
			CFH, ESO, CTIO	*	S91
N39	4/23/86	12.4	CFH, IRTF, UH	—	S91, (Buie)
N40	5/04/86	9.6	KPNO, ESO	—	(Hubbard)
n86-66	7/27/86	9.9	IRTF, UH, PAL	*	N95, (Buie)
n86-83	8/23/86	13.3	IRTF, UKIRT, UH	—	(Buie)

N41	5/23/87	11.5	PAL, IRTF	N95, (Buie)
n1006	6/22/87	10.1	ESO	S91
n1008	7/09/87	11.3	PAL, MMT, KPNO, UKIRT	H92, N95
n1012	8/29/87	10.4	IRTF (?)	(Buie)
n1028	5/26/88	11.6	IRTF (?)	(Buie)
N48	7/09/88	10.4	PAL, MMT	H92, N95
N49	8/02/88	10.5	ESO	S91
n1038	8/25/88	10.3	CFH, IRTF	S91, (Buie)
N51	9/12/88	6.8	OPMT, OHP	S91
N55	7/08/89	5.5	ESO, OPMT	S91
n1077	7/11/90	11.4	ESO	(Sicardy)
N3749	8/18/91	12.1	IRTF	(French)
N4174	7/11/92	11.7	PAL, CTIO, ESO	F93

<sup>a</sup> Codes from Klemlola et al. (1978); Mink et al. (1981); Mink and Klemlola (1985); Nicholson et al. (1988); Klemlola and Mink (1991); and unpublished star lists by Nicholson (1983,1984).

<sup>b</sup> Measured stellar magnitude at  $\lambda 2.2 \mu\text{m}$ .

<sup>c</sup> Station codes: AAO = Anglo-Australian Observatory; CAT = Catalina Station; CFH = Canada-France-Hawaii Telescope; CTIO = Cerro-Tololo Interamerican Observatory; ESO = European Southern Observatory; IRTF = Infrared Telescope Facility; KAO = Kuiper Airborne Observatory; KPNO = Kitt Peak National Observatory; LOW = Lowell Observatory; ML = Mt. Lemmon; MMT = Multiple Mirror Telescope; MSO = Mount Stromlo Observatory; MWO = Mount Wilson Observatory; OHP = Observatoire de Haute Provence; OPMT = Observatoire du Pic du Midi; PAL = Palomar Observatory; SAAO = South African Astronomical Observatory; UH = University of Hawaii 88"; UKIRT = United Kingdom Infrared Telescope.

<sup>d</sup> — denotes no apparent occultations;  $\times$  denotes a report of a possible arc occultation; \* denotes a confirmed report by two or more stations; + indicates an event near the orbit of Triton.

<sup>e</sup> Reference codes: C86 = Covault et al. (1986); E81 = Elliot et al. (1981); E85 = Elliot et al. (1985); F93 = French et al. (1993); FL70 = Freeman and Lyngaa (1970); H85 = Hubbard et al. (1985); H86a = Hubbard (1986); H86b = Hubbard et al. (in preparation); KL69 = Kovalevsky and Link (1969); NJ80 = Nicholson and Jones (1980); N90 = Nicholson et al. (1990); N95 = Nicholson et al. (1995); R82 = Reitsma et al. (1982); S91 = Sicardy et al. (1991); and names in parentheses indicate holders of unpublished data.

Original estimates placed the ring at  $67,000 \pm 4000$  km (Hubbard et al. 1986), but subsequent analysis based on the post-Voyager Neptune pole orientation (Jacobson et al. 1991) and photographic plates taken shortly before the occultation yield a radius of  $65,300 \pm 3000$  km (Sicardy et al. 1991) consistent with the Adams ring. A radial width  $W = 15$  km and an average normal optical depth  $\tau \simeq 0.13$  were derived from diffraction models (Manfroid et al. 1986; Hubbard et al. 1986; Sicardy et al. 1991). Calculations of the mean motion for the arcs utilizing groundbased and Voyager observations (Nicholson et al. 1990; see Sec. III.A.2) indicate that this event was probably caused by the Egalité arc. No corresponding feature was seen when the star's track crossed the same radial range on the opposite side of the planet, leading Hubbard et al. (1986) to propose the term "arc" for the feature.

The second probable detection of an arc involved the occultation of a binary star, observed at a single station in South Africa in June 1985 (Covault et al. 1986). A notable feature of this occultation is that only a single member of the binary was occulted by the arc, although the second star crossed the same equatorial radius only  $5.9^\circ$  or 6500 km away in longitude. The estimated  $W \simeq 8$  km and  $\tau \simeq 0.11$  were comparable to that of the feature observed in 1984. The geometry is illustrated in Fig. 9b, and the profile in Fig. 10b. Reconstruction of the geometry using the post-Voyager Neptune pole yielded an equatorial plane radius of  $62,853 \pm 27$  km for an occultation of star A, within 80 km of the mean radius of the Adams ring, and a probable identification with the Liberté arc (Nicholson et al. 1990). An occultation of star B would have corresponded to an equatorial radius of  $64,577 \pm 32$  km, well outside the limits of the known rings.

The third sighting of a Neptunian arc, and the second to be confirmed by independent observations, occurred on August 20, 1985 when an occultation by an unusually bright star was observed at several sites in the western hemisphere. Although no ring-like dips were observed in California, Arizona or Chile, both the IRTF and CFH telescopes on Mauna Kea recorded simultaneous, virtually identical features in their egress lightcurves (Nicholson et al. 1990; Sicardy et al. 1991; see Figs. 9b and 10c). Square-well diffraction models independently fitted to the data by Nicholson et al. and Sicardy et al. yielded very similar results: either  $W = 26.0 \pm 0.7$  km and  $\tau = 0.070 \pm 0.003$ , or  $W = 16.4 \pm 1.0$  km and  $\tau = 0.118 \pm 0.002$ . The ambiguity arose from the uncertain angular diameter of the star, for which the fits gave two equally acceptable values. Narayan and Hubbard (1988) have argued that the spikes observed in the atmospheric lightcurve are more consistent with the larger stellar diameter, and thus the narrower, more opaque ring model. The equatorial radius of this feature is particularly sensitive to Neptune's pole direction, which led initially to a very wide radius range of 54,000 to 63,000 km. Independent post-Voyager reconstructions of the geometry yielded radii of  $62,840 \pm 53$  km (Nicholson et al. 1990) or  $63,160 \pm 200$  km (Sicardy et al. 1991), again compatible with the Adams ring, and a probable identification with the Egalité arc, the same feature observed in July 1984.

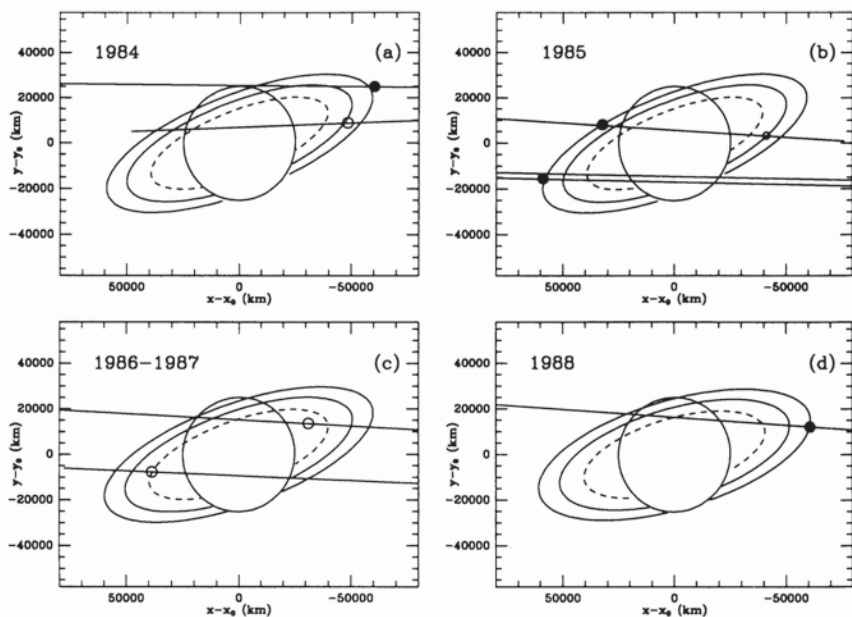


Figure 9. Sky-plane trajectories for Neptune stellar occultations showing those events thought to be due to ring or arc material. The ellipses represent the locations of the Adams, Le Verrier, and Galle rings, for the Neptune pole determined by Jacobson et al. (1991). (a) The occultations of July 22, 1984 (top) and April 18, 1984; (b) August 20, 1985 (top) and June 7, 1985, the latter showing the double track of the binary star's two components; (c) July 9, 1987 (top) and July 27, 1986; and (d) July 9, 1988. The individual events are described in Table V. Filled circles show occultations attributed to arcs embedded in the Adams ring, while open circles indicate the locations of other events listed in the Table. Coordinates  $x - x_0$  and  $y - y_0$  are measured from the center of the planet towards the East and North, respectively.

The fourth and most recent Earth-based occultation to show evidence of a feature which might correspond to one of the Adams ring arcs was observed in July 1988 at Palomar Observatory in California and at the Multiple-Mirror Telescope (MMT) in Arizona (Nicholson et al. 1994; Hubbard 1994; see Fig. 9d). Although dips are seen with equal equatorial radii in both lightcurves, only the feature in the Palomar data is statistically significant and the event cannot be regarded at this point as a confirmed arc detection. While the longitude matches that of the Liberté arc, and the  $W \simeq 11$  km and  $\tau \simeq 0.09$  are compatible with the previous observation of this arc (see Fig. 10d), its equatorial radius of  $63,170 \pm 28$  km places this feature  $\sim 240$  km outside the known mean radius of the Adams ring. The identification of this event with the Adams ring thus remains questionable.

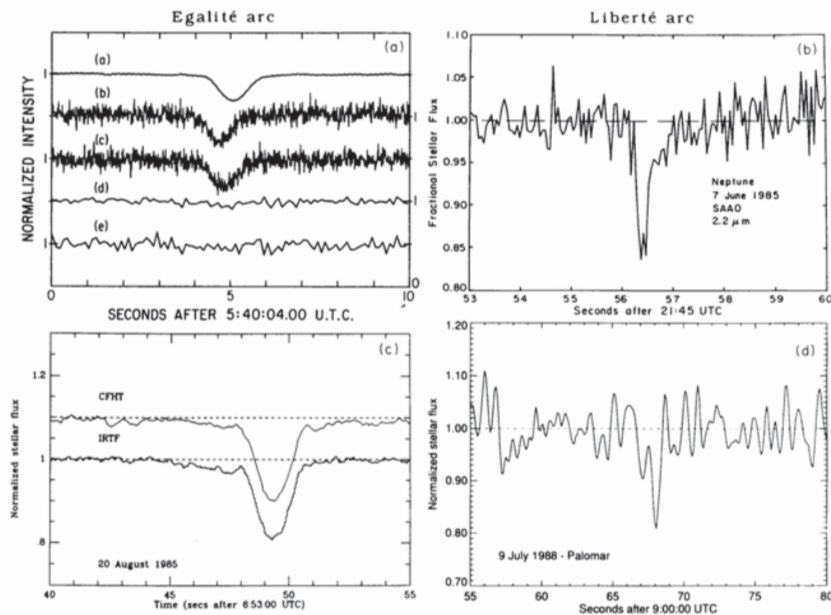


Figure 10. Earth-based occultation profiles for the Adams ring arcs. (a) The egress occultation of July 22, 1984 (cf., Fig. 9a), showing lightcurves from (top to bottom) the ESO 1-m and 0.5-m telescopes ( $\lambda 2.2 \mu\text{m}$  and  $0.81 \mu\text{m}$ ), and the CTIO 0.9-m telescope ( $\lambda 0.88 \mu\text{m}$ , broadband visible, and  $0.44 \mu\text{m}$ ). The absence of a drop in signal in the visible and blue channels is expected for those spectral regions in which the light from Neptune swamps the stellar signal. The delay in the top trace is instrumental in origin (figure from Hubbard et al. 1986). (b) The binary star egress occultation of June 7, 1985, observed from SAAO at  $\lambda 2.2 \mu\text{m}$  (cf., Fig. 9b). Note the shoulder at the outer edge of the arc (figure from Covault et al. 1986). (c) The egress occultation of August 20, 1985, showing  $\lambda 2.2 \mu\text{m}$  lightcurves from the CFHT and IRTF telescopes on Mauna Kea, Hawaii (cf., Fig. 9b). Note the prominent shoulder at the inner edge of the arc, extending for  $\sim 50$  km in radius, and the possible weaker shoulder at the outer edge (data from Nicholson et al. [1990] and Sicardy et al. [1991]). (d) The ingress occultation of July 9, 1988, observed from Palomar Observatory at  $\lambda 2.2 \mu\text{m}$  (cf., Fig. 9d). Although noisy, the lightcurve shows signs of a shoulder at the arc's outer edge (data from Nicholson et al. 1995). The arc identifications correspond to the nominal mean motion of  $820.1185^\circ\text{day}^{-1}$ .

We should finally take note of several other reports of occultations by Neptunian arc-like features at equatorial radii which are clearly *not* associated with the Adams ring (cf., Fig. 4). These include a curious triple event observed in April 1984, within the broad Lassell ring at a radius of  $55,192 \pm 40$  km (Nicholson et al. 1994; see Fig. 9a); a single arc-like feature observed at both Palomar and the IRTF in July 1986 at a radius of  $42,220 \pm 50$  km, essentially coincident with the Galle ring (Nicholson et al. 1990; Fig. 9c); an event observed at Palomar and the MMT in July 1987 at a radius of  $35,205 \pm 40$  km,

interior to any known component of the Neptunian ring system (Hubbard, personal communication 1994; Fig. 9c); as well as a single unusual event seen in June 1987 at ESO near where the stellar track crossed the orbit of Triton (Sicardy et al. 1991). It is unclear at present whether any of these additional features are truly due to occultations by circum-Neptune material (though all except the April 1984 event are statistically significant and otherwise unexplained). If so, they suggest that arc-like clumps of material, or equivalently kilometer-sized bodies, may exist in the Neptune system in other locations besides the Adams ring. A careful scrutiny of Voyager images currently offers the best hope of confirming the existence of some or all of these features, unless they are very short-lived.

#### NEPTUNE RING OCCULTATIONS

$$n = 820.1185 \text{ day}^{-1}$$

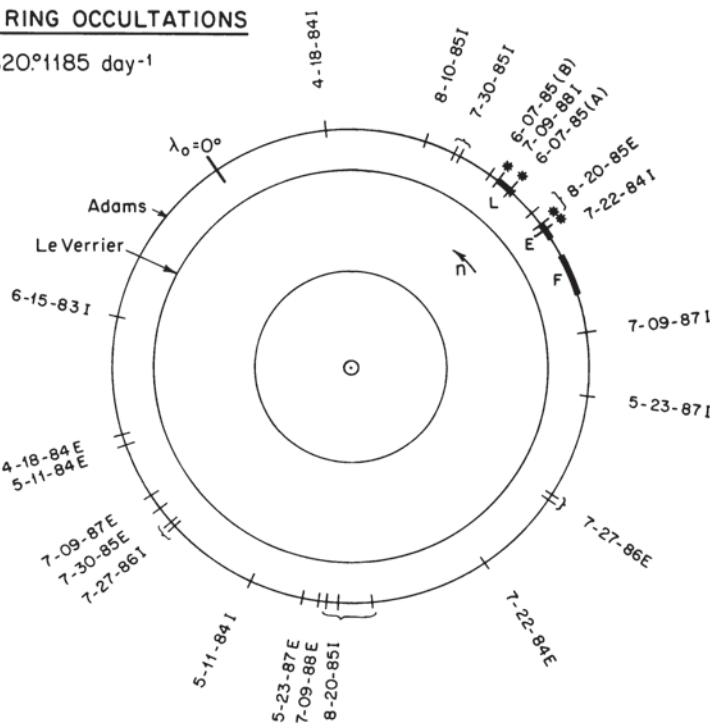


Figure 11. Earth-based occultation cuts across the Adams ring, corrected to a common epoch using an assumed prograde mean motion of  $820.1185 \text{ day}^{-1}$  (I = ingress, E = egress). The corresponding locations of the principal ring arcs, Liberté, Egalité, and Fraternité are indicated. Asterisks denote the four putative arc occultations shown in Fig. 10 (figure from Nicholson et al. 1995).

Figure 11 shows the distribution in longitude of most reported Earth-based occultation cuts across the Adams ring, translated to a common epoch using the arc mean motion of  $820.1185 \text{ day}^{-1}$  determined by Nicholson et al. (1990) (see Sec. III.A.2). The corresponding locations of the three principal

arcs, Liberté, Egalité and Fraternité, are also shown.

Klemola and Mink (1991) have predicted future Neptune occultations through the year 1999, for which Mink et al. (1992) calculated the probabilities of arc crossings. An occultation on July 11, 1992 was predicted to cross the arc region, but observations at Palomar and at CTIO failed to show any dips at the predicted times and reconstruction of the geometry showed that the star passed between the Courage and Liberté arcs (French et al. 1993).

*2. Limits on Continuous Rings* The occultations of particularly bright stars on June 15, 1983, July 22, 1984 and August 20, 1985, for which data of very high signal-to-noise ratio were obtained at multiple telescopes, provide the most promising lightcurves in which to search for evidence of the continuous rings discovered in the Voyager images. Sicardy et al. (1991) and Nicholson et al. (1995) have re-analyzed these (and other) data sets with a view to detecting, or setting upper limits on, the equivalent widths of the continuous rings. These investigations have led to restrictive upper limits on the radially integrated optical depths for the Adams and Le Verrier rings (Sicardy et al. 1991), and to a tentative detection of the Le Verrier ring by Nicholson et al. (1995), as described below.

Sicardy et al. (1991) performed an objective search for statistically significant features in the lightcurves from nine occultations observed between 1983 and 1989. A window of fixed radial length (typically 50 km) was moved through each lightcurve, and a local baseline was fitted to a 1000 km data segment at each window position to remove low-frequency noise due to telescope guiding errors, atmospheric extinction, etc. The equivalent width within the window,  $E_o(R)$ , was then computed for successive positions of the window along the data segment, and the result plotted as a function of radius in Neptune's equatorial plane. Examples of their results are shown in Fig. 12; note the prominent arc events of July 22, 1984 and August 20, 1985 which show clearly here as positive spikes in equivalent width. An important advantage of this approach over simple visual inspection of lightcurves is that it provides an empirical statistical distribution of  $E_o$  against which any suspected events can be tested. One disadvantage is that features much wider than the integration window tend to be suppressed, and in extreme cases eliminated, by the baseline removal process.

Two high-quality data sets analyzed by Sicardy et al. (1991) led to stringent  $5\sigma$  upper limits on the equivalent widths of undetected *narrow* (i.e.,  $\leq 50$  km) rings of  $E_o \leq 200$  m and  $E_o \leq 350$  m (or  $\tau \leq 0.004$  to 0.007, averaged over the 50-km window width), the former limit applying to radii in the range 52,000 to 90,000 km, with the latter extending down to a minimum radius of 28,000 km. In the immediate vicinity of the Adams and Le Verrier rings, Sicardy et al. set an even tighter upper limit of  $E_o < 150$  m on the existence of any *correlated* narrow feature occurring at the same radius (within astrometric uncertainties) in four different high-quality lightcurves. These results represent firm upper limits, at a wavelength of  $2.2 \mu\text{m}$ , on the equivalent width of the Le Verrier ring and regions of the Adams ring well away from the arcs.

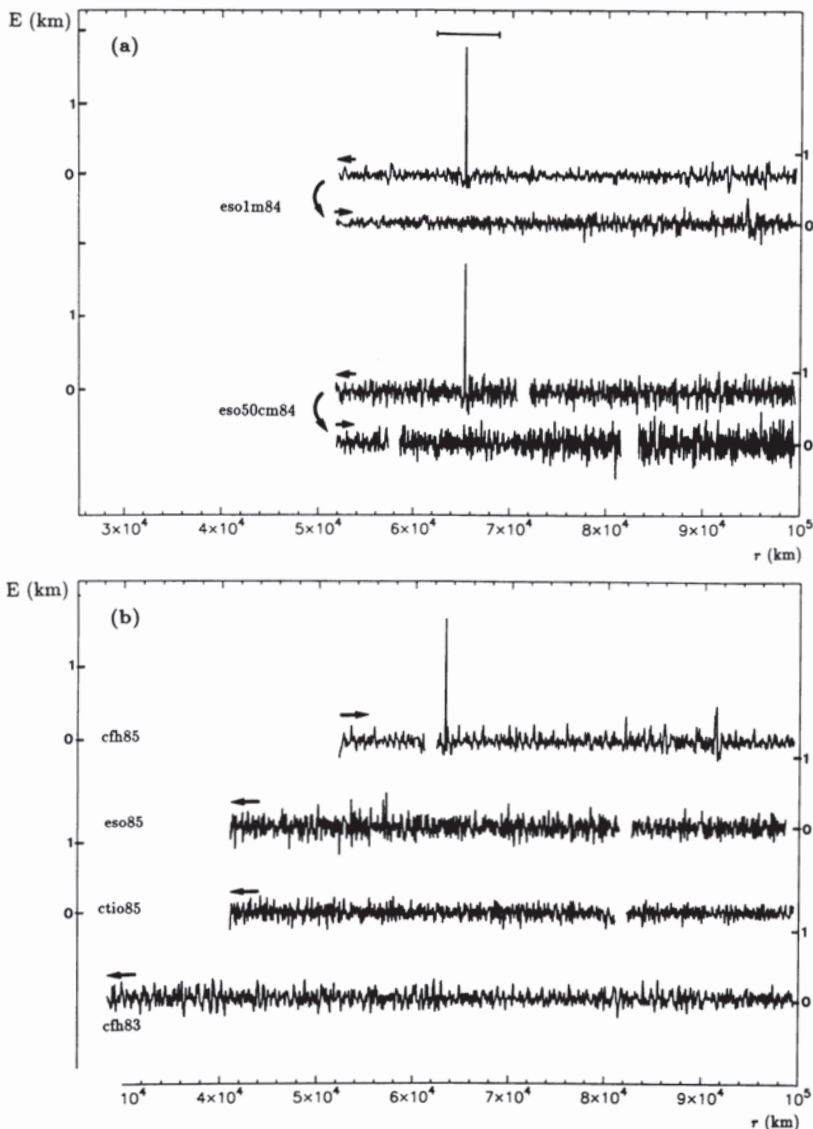


Figure 12. Profiles of equivalent width derived from the occultations of June 15, 1983 (CFH83), July 22, 1984 (ESO1m84, ESO50cm84), and August 20, 1985 (CFH85, ESO85, CTIO85). A window of radial width 50 km was used for all profiles. The prominent spikes at 63,000 km in the July 22, 1984 and CFH85 profiles correspond to the arc occultations shown at higher resolution in Fig. 10a and 10c. Arrows indicate ingress and egress light curves, and the minimum radius reached during the July 22, 1984 event. The other curves are terminated inward by planetary ingress or egress. The horizontal error bar over the 1984 arc indicates the astrometric uncertainty in the radial scale, due to the lack of a planetary occultation (figure from Sicardy et al. 1991).

(Because only correlated features were searched for, it is possible that either ring is inhomogeneous, with an equivalent width  $>150$  m at some longitudes.) The corresponding upper limit on the optical depth for narrow ( $<50$  km) rings is  $\tau \leq 0.003(50/W)$ , where  $W$  is the true ring width in km. Finally, Sicardy et al. used the best raw lightcurve, that of July 22, 1984, to set an upper limit of  $\tau < 0.008$  on the optical depth of any *broad* (i.e.,  $W > 50$  km) ring component in the vicinity of the Adams or Le Verrier ring.

Nicholson et al. (1995) report a similar study of data from eight occultations observed between 1985 and 1988. They employed the same equivalent width technique introduced by Sicardy et al., but used a narrower 15 km wide window chosen to match the observed width of the arcs. This has the effect of maximizing the signal-to-noise ratio of any positive narrow ring detections, by reducing the influences of terrestrial atmospheric scintillation and telescope guiding noise on the derived equivalent widths. Data from the August 20, 1985 ingress occultation, shown in Fig. 13, yielded a  $3\sigma$  upper limit on the equivalent width of the Adams ring of  $E_o \leq 75$  m ( $\tau \leq 0.005$  over the 15-km window) at a location  $\sim 115^\circ$  behind the Fraternité arc. With a 50 km wide window, the corresponding upper limit is 210 m ( $\tau \leq 0.004$ ), consistent with Sicardy et al. (1991). The egress track on this date crossed the Egalité arc, as described in Sec. II.B.1.

The ingress data from this occultation show a marginally significant ( $3.6\sigma$ ) feature at a radius of  $\sim 52,900$  km, quite close to the expected crossing of the Le Verrier ring (Fig. 13, top panel). Although the maximum equivalent width is  $\sim 90$  m in a 15 km wide processing window, the overall radial width of the feature is  $\sim 135$  km and its full equivalent width is  $E_o = 520 \pm 55$  m, corresponding to an average normal optical depth of  $\tau = 0.004$ . At an equatorial radius of  $53,055 \pm 35$  km, as calculated using the Le Verrier ring pole (Porco et al. 1992; Showalter and Cuzzi 1992b) and precessed back to 1985, the feature lies  $\sim 150$  km interior to the mean radius of the Le Verrier ring derived from the Voyager images. Both the width and optical depth are comparable to those found for this ring in the Voyager PPS occultation, described in Sec. II.B.3. Unfortunately, the egress crossing of the same radius for this occultation coincided with a brief interruption in the observations following Neptune egress, so that no independent confirmation of its reality was possible. As a cautionary note, we point out that no comparable feature at the radius of the Le Verrier ring is seen in the data sets analyzed by Sicardy et al. (1991; see Fig. 12). In attempting to reconcile these apparently contradictory results, Nicholson et al. (1995) concluded that the Le Verrier ring may vary by as much as a factor of 2 in equivalent width on scales of  $\sim 10^\circ$  in longitude, though the Voyager images show no evidence for such variations (Showalter and Cuzzi 1995).

Figure 14 shows the combined upper limits ( $3\sigma$ ) found by Nicholson et al. (1995) and Sicardy et al. (1991) on the equivalent width of the Adams ring as a function of corotating longitude, together with the measured arc equivalent widths. Note, however, that the processing window widths differ for the two

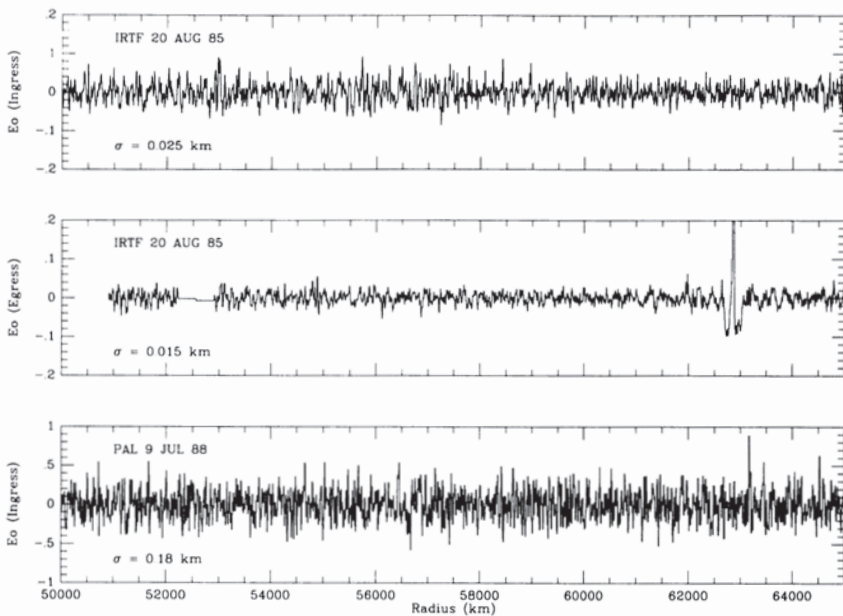


Figure 13. Equivalent width profiles derived from IRTF observations of the August 20, 1985 occultation (egress and ingress), and the July 9, 1988 Palomar ingress occultation. A window of radial width 15 km was used. The spike at 62,900 km in the IRTF ingress data is due to the arc occultation seen at higher resolution in Fig. 10c, while the spike at 63,200 km in the Palomar data is shown in Fig. 10d. Rms equivalent widths are 25 m, 15 m, and 180 m, respectively. Note the weak feature ( $E_{\max} = 90$  m) at 52,900 km in the IRTF ingress data, tentatively identified with the Le Verrier ring. The gap in the egress data at the same radius is due to a telescope guiding check (figure adapted from Nicholson et al. 1995).

analyses. The tightest upper limits of 75 and 120 m apply to chords which crossed the Adams ring at longitudes at least  $75^\circ$  away from the arc region. Closer to the arcs, a  $3\sigma$  limit of 300 m is provided by the August 10, 1985 occultation (for a 15 km window) at a corotating longitude of  $299^\circ$ , only  $14^\circ$  ahead of the Courage arc. Combining data from the best four data sets with accurate geometric reconstructions, and assuming a uniform equivalent width for the Adams ring well away from the arc region, Nicholson et al. (1995) found a 90% probability that  $E_o \leq 90$  m for a radial width of up to 50 km. The corresponding upper limit on the average optical depth of the ring is  $\tau \leq 0.002(50/W)$ , where  $W$  is the true radial width in km.

*3. Voyager Occultations.* Following close approach to Neptune on August 25, 1989, the Voyager Radio Science team conducted dual-frequency radio occultation probes of the rings and the atmosphere of Neptune (Tyler et al. 1989). No extinction by ring material was detected, down to a limit of  $\tau = 0.01$  at  $\lambda 3.6$  cm and at a radial resolution of 2 km (i.e.,  $A \leq 20$  m). However, only the region of the Adams ring was probed on both ingress and egress, and

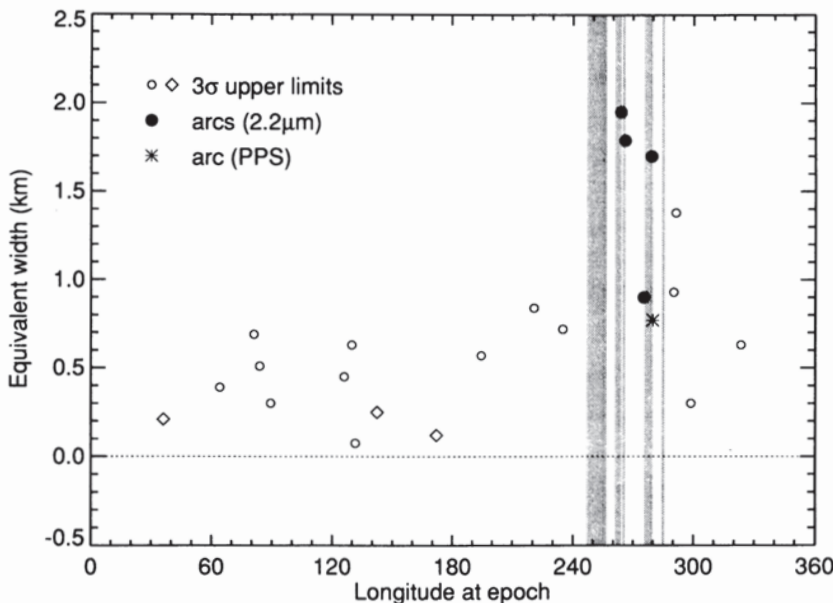


Figure 14. Azimuthal distribution of  $3\sigma$  upper limits on equivalent width derived from Earth-based occultation data for the Adams ring (open circles—Nicholson et al. 1995; diamonds—Sicardy et al. 1991) compared with measured equivalent widths from the arc occultations shown in Fig. 10 (filled circles) and the Voyager PPS occultation (asterisk). Vertical bands indicate the locations of the ring arcs Courage, Liberté, Egalité, and Fraternité (right to left), as determined by Porco (1991) (figure from Nicholson et al. 1995).

these data were affected by the radio beam's traversal of Neptune's ionosphere at the same time. The region of the Le Verrier ring was probed on egress only, and that of the Galle ring not at all. The ingress and egress radio cuts crossed the Adams ring 60° and 95° from the arc region, respectively (Tyler et al. 1989).

Both the Voyager Photopolarimeter (PPS) and Ultraviolet Spectrometer (UVS) instruments successfully observed an ingress occultation of the Neptunian ring system by the star  $\sigma$  Sgr, ~5 hr before Neptune closest approach (Lane et al. 1989; Broadfoot et al. 1989). Effective wavelengths for the two experiments were  $0.26 \mu\text{m}$  (PPS) and  $0.11 \mu\text{m}$  (UVS). Observations of the  $\sigma$  Sgr occultation began at a radius in Neptune's equatorial plane of 76,056 km and ended at a radius of 42,414 km, very near the minimum radius point on the occultation chord across the rings. The data thus span the regions of the Adams and Le Verrier rings, but stop just short of the Galle ring. Radial velocities at the ring crossings were  $-7.29 \text{ km s}^{-1}$  (Adams) and  $-5.97 \text{ km s}^{-1}$  (Le Verrier), resulting in raw PPS sampling intervals of 73 m and 60 m.

The Adams ring was clearly detected in both PPS and UVS data, within

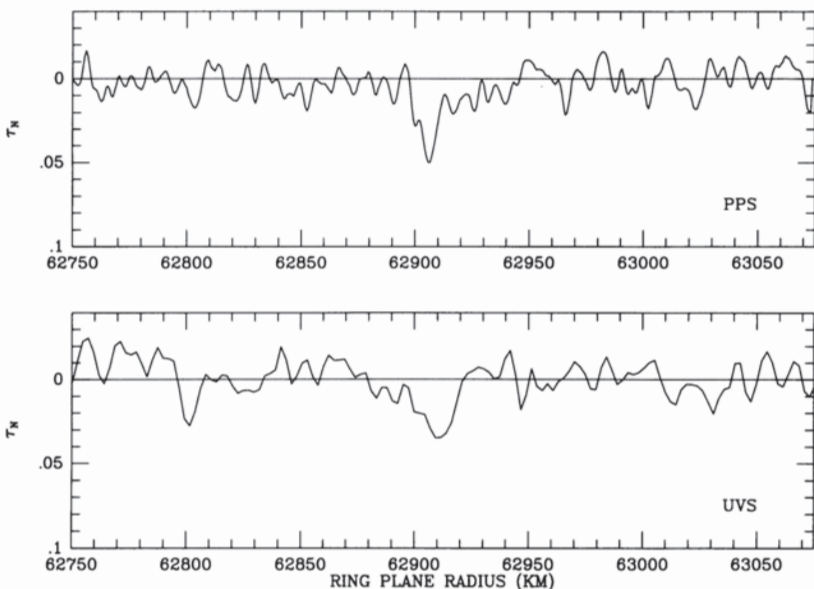


Figure 15. Occultation profiles of the Adams ring obtained by the Voyager PPS and UVS instruments on August 24, 1989, at  $\lambda=0.26\text{ }\mu\text{m}$  and  $0.11\text{ }\mu\text{m}$ . The  $\sigma$  Sgr occultation chord cut through the leading edge of the Liberté arc (cf., Fig. 14). (a) The PPS data, averaged to a radial resolution of 5 km. Note the 14 km-wide core and 30 km-wide exterior shoulder. (b) The UVS data, at the full resolution of 2.3 km. Only the core is visible in this somewhat noisier data set. The data have been geometrically calibrated using the Adams ring pole determined by Porco (1991). (Data provided by the PPS and UVS Science Teams.)

$\sim 20$  km of the expected radius (Fig. 15 above). Furthermore, reconstruction of the event geometry shows that the occultation crossed the Liberté arc at a corotating longitude  $\lambda_0 = 279.9^\circ$ , essentially coincident with the leading edge of this feature in the Voyager images (see Fig. 5 above). Both PPS and UVS profiles shown in Fig. 15 reveal a “core” component of width  $W \sim 14$  to 15 km. In addition, the PPS data show a broader, more transparent exterior component 20 to 30 km in width, consistent with the groundbased observations of this arc shown in Fig. 10. [While the UVS data (Fig. 15b) seem to indicate the presence of a  $\sim 30$  km *interior* component, this feature is probably not statistically significant.] The PPS profile was produced by binning at a sampling interval of 1.5 km and smoothing the data further to an effective resolution of 5 km. Analysis of this feature by Horn et al. (1990) indicates a core of width 14.3 km and a mean normal optical depth (uncorrected for diffraction) of  $0.034 \pm 0.005$ , and a shoulder of width 28.6 km and mean

optical depth of  $0.018 \pm 0.003$ . The overall equivalent depth of the arc is  $A = 0.77 \pm 0.13$  km, of which roughly 50% is in the core. The UVS data, shown in Fig. 15b, have a radial resolution of 2.3 km and show an overall equivalent depth of  $A = 0.66 \pm 0.12$  km (Broadfoot et al. 1989), statistically identical with the PPS result. This suggests that very little of the arc's total cross sectional area is in particles in the  $0.1 \mu\text{m}$  size range. As noted previously, these optical depths must correspond to  $Q_{\text{occ}} \approx 2$ , unless the average ring particle is cm-sized or larger. Because the  $\sigma$  Sgr occultation track probed the leading edge rather than the central part of the Liberté arc, the above numbers may underestimate the average optical depth of this arc in the ultraviolet.

A blind statistical analysis of the PPS data by Horn et al. (1990) showed that the Adams ring occultation is the only unambiguous non-random event. The second-largest feature (either positive or negative) in the PPS lightcurve, however, falls within about 100 km of the expected location of the Le Verrier ring, using the Jacobson et al. (1991) pole. Although only marginally significant in a total data set of 540,000 points, the probability that this feature should occur within such close proximity to the known radius of the Le Verrier ring is very small. The profile of this feature is shown in Fig. 16b, smoothed to a radial resolution of 5 km. For comparison, the only other occultation detection of the Le Verrier ring, in the August 20, 1985 groundbased occultation, is shown in Fig. 16a, smoothed to a radial resolution of  $\sim 8$  km. No core such as that shown by the Adams ring is apparent, and the very low signal-to-noise ratio implies that even the width of the ring is in some doubt. Horn et al. (1990) estimate a width of 113 km, and an average optical depth of  $0.0062 \pm 0.0015$ , corresponding to an equivalent depth of  $A = 700 \pm 200$  m. The Le Verrier ring has apparently not been identified in the UVS data, although no detailed analysis of these data has been published to date.

Unlike the case for Earth-based occultations, the geometry of the Voyager experiment can be reconstructed with an accuracy limited only by that of the spacecraft trajectory (a few km), and our knowledge of the ring pole direction. If we use the Adams ring pole determined by Porco (1991) from the analysis of Voyager images and the UVS datum (Sec. III), we obtain a radius for the core of the arc of 62,904 km, in excellent agreement with the resonant perturbation model of Porco (see Sec. III.A.2). Porco et al. (1992) and Showalter and Cuzzi (1992b) have independently determined the pole direction of the Le Verrier ring from Voyager images; using this pole we obtain a mean radius from the PPS cut across this ring of 53,125 km, or 75 km less than that derived from the Voyager imaging data. [Projected into Neptune's equatorial plane, as determined by Jacobson et al. (1991), the mean radii of the PPS profiles of the Adams arc and Le Verrier ring are 62,818 km (core) and 53,070 km, respectively. The UVS mid-time (Broadfoot et al. 1989) for the Adams arc corresponds to an equatorial radius of 62,825 km.]

*4. Summary of the Occultation Data.* Table V summarizes the principal characteristics of reported occultation detections of the Neptunian rings and arcs, including the Voyager occultation data discussed in Sec. II.B.3. In

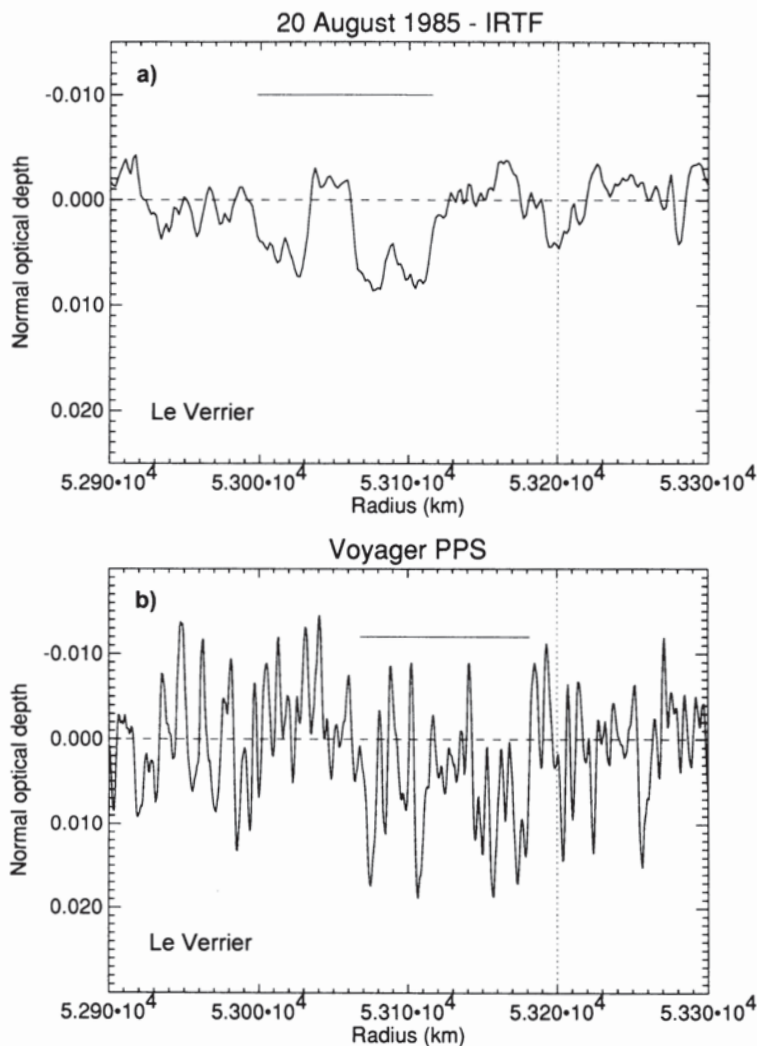


Figure 16. A comparison of optical depth profiles for the Le Verrier ring obtained from the August 20, 1985 and Voyager PPS occultations, on a common radial scale. The assumed ring plane pole is that given by Showalter and Cuzzi (1992b), based on Voyager images. The groundbased and PPS data have been averaged to radial resolutions of 8 km and 5 km, respectively. The overall widths and average optical depths of the two profiles are similar, although both are close to the noise level in their respective data sets. There is some evidence in both profiles for a two-component structure. The image-derived mean radius for this ring of  $53,200 \pm 20$  km (Porco et al. 1992) is indicated by the dotted line. The systematic astrometric uncertainty in the groundbased data is  $\sim 35$  km, while that in the PPS data is  $\sim 5$  km (figure from Nicholson et al. 1995).

addition to the calendar date of each observation, the table gives the Julian Ephemeris Date, backdated by the ring-to-observer light travel time, the radius and longitude of the feature in Neptune's equatorial plane, and either the measured equivalent width  $E_o$  for groundbased occultations or equivalent depth  $A$  for spacecraft data. The latter quantities are defined in Eqs. (4) and (6) above.

(a.) *Geometry.* Equatorial radii and longitudes in Table V correspond to the Neptune pole direction determined by Jacobson et al. (1991), including the effects of precession of the planet's spin axis during the period between each observation and the epoch of Voyager observations. [Neptune's pole precesses about the invariable pole of the Neptune-Triton system with a period of  $\sim 690$  yr and an obliquity, inferred from the Voyager radio science determination of Triton's mass, of  $0.506^\circ$ ; the Neptune pole position at the time of the Voyager encounter derived by Jacobson et al. is  $\alpha_p = 298.8575 \pm 0.15^\circ$ ,  $\delta_p = 42.8118 \pm 0.05^\circ$  (1950.0). The corresponding location of the invariable pole is  $\alpha_{IP} = 298.9526 \pm 0.15^\circ$ ,  $\delta_{IP} = 43.3135 \pm 0.10^\circ$  (1950.0).] Longitudes are measured in the invariable plane from the ascending node of this plane on the Earth's mean equator of 1950.0 to the ascending node of Neptune's equator on the invariable plane, and thence in Neptune's equatorial plane to the occultation point. (Longitudes measured directly from the ascending node of Neptune's equator on the Earth mean equator of 1950 are greater by  $0.065^\circ$ .)

For occultation events attributed to the Adams ring or to the Le Verrier ring, the table also lists separate *ring plane* radii calculated using the poles determined by Porco (1991) for the Adams ring and by Porco et al. (1992) and Showalter and Cuzzi (1992b) for the Le Verrier ring. As discussed in Sec. II.A.7, these ring poles differ slightly from the Jacobson pole (by  $0.062^\circ$  and  $0.080^\circ$ , respectively), although both lie within the error ellipse of the latter. We have implemented these ring poles by treating their offsets from the nominal Neptune pole as adjustments to the invariable pole, retaining the Jacobson model for pole precession due to Triton; over the period of five years separating the earliest arc occultation observation from the Voyager encounter, the planet's spin axis has precessed by a non-negligible  $0.024^\circ$ . At the Voyager epoch, the Adams ring pole is at  $\alpha_p = 298.9398 \pm 0.006^\circ$ ,  $\delta_p = 42.8249 \pm 0.002^\circ$  (1950.0), while the Le Verrier ring pole is at  $\alpha_p = 298.965 \pm 0.027^\circ$ ,  $\delta_p = 42.800 \pm 0.010^\circ$  (1950.0). For the Adams ring events, we have also determined the corotating longitude at the Voyager reference epoch, JED 244 7757.0 (Owen et al. 1991; Porco 1991), denoted  $\lambda_0$ , to facilitate locating the occultation cuts relative to the longitudinal imaging profile shown in Fig. 5. For this calculation, we have assumed an arc mean motion of  $820.1185 \text{ day}^{-1}$ , as determined by Nicholson et al. (1990) and discussed in Sec. III.A.2 below.

We note here that the corotating longitudes for the Adams ring arcs given in Table V are dependent on the adopted arc mean motion. Nicholson et al. (1990) noted a second possible value for the mean motion of  $\sim 820.1110 \text{ day}^{-1}$ , which also fits the available observations, but which

changes the identification of the arcs observed in 1984 and 1985 from Liberté and Egalité to Egalité and Fraternité, respectively. (Because of the close proximity in time of the Voyager imaging and occultation observations, there is no such uncertainty in the identification of the PPS/UVS observation with the Liberté arc.) Updating their earlier results to include a redetermination of the geometry for the July 22, 1984 event and the arc positions determined by Porco (1991), Nicholson et al. (1995) found slightly revised mean motion solutions of either  $820.1194 \pm 0.0006 \text{ day}^{-1}$  or  $820.1118 \pm 0.0006 \text{ day}^{-1}$  (see Fig. 20 below). The adjustments to the values of  $\lambda_0$  listed in Table V if we were to use the revised value are at most +1.9°.

(b.) *Widths and Internal Structure.* Square-well diffraction models fitted to the observations of the Egalité arc on July 22, 1984 and August 20, 1985 yield consistent values of  $W = 15$  to 17 km, if we assume the larger star diameter for the 1985 occultation (Sicardy et al. 1991). A width of ~8 km was inferred for the Liberté arc from the June 7, 1985 occultation, though no square-well model fits have been published for this lower-quality data set. The inferred radial width from the July 9, 1988 event, with a longitude which matches, but a radial distance which differs from, the Liberté arc was ~15 km. These results are roughly consistent with the arc "core" widths of 14 to 15 km derived for the Liberté arc from the PPS and UVS occultation observations.

Almost no reliable information on the internal structure of the arc cores is available from the present occultation data. Diffraction limits the resolution of Earth-based occultations at Neptune's distance of 29 AU to ~4 km at  $\lambda 2.2 \mu\text{m}$ , but the highest signal-to-noise profiles of the arcs are further limited in resolution by projected stellar diameters of 10 to 15 km. The arc widths inferred from these data are in fact comparable to the stellar diameters, and the smooth appearance of the occultation profiles consequently says little about what underlying structure may be present. A cautionary example of this is provided by the narrower Uranian rings, whose complex internal structure was revealed only by the Voyager stellar and radio occultation experiments (see French et al. 1991). In the case of Neptune's rings, however, the low optical depth of the arc reduces the effective signal-to-noise ratio of the PPS data to the point where, although the ring is clearly resolved, little if any of the apparent internal structure is statistically significant.

A noteworthy feature common to three of the four Earth-based occultation profiles in Fig. 10, as well as the PPS profile in Fig. 15a, is a shoulder which extends up to ~50 km from the core of the arc. These shoulders appear consistently on the exterior edge of the Liberté arc (assuming the interior "shoulder" feature in the UVS occultation of the Liberté arc [Fig. 15b], is statistically insignificant), but on the interior edge of the August 20, 1985 profiles of Egalité. No shoulder is apparent in the July 22, 1984 observation of this arc. The average optical depth of the Egalité interior shoulder is ~0.008, and there is a suggestion that it is separated from the main ring by a narrow gap (Nicholson et al. 1990). It is possible that there is also a more tenuous exterior shoulder in this profile, but this feature is apparent only in the

CFHT data and may not be real. These “shoulders” are somewhat reminiscent of the tenuous components exhibited by the Uranian  $\delta$  and  $\eta$  rings (Gresh et al. 1989; French et al. 1991), and by Saturn’s F ring (Lane et al. 1982). In the case of the Uranian rings, the optical depths of the tenuous features seem to be independent of wavelength, suggesting the presence of large particles rather than leakage of dust-sized particles from the main rings. This is not true, however, for the F ring’s fainter component, which disappears completely at centimeter wavelengths (Marouf et al. 1986). Although no comparable information exists for the shoulders of the Neptunian arcs, the F ring model seems more likely to be applicable on dynamical grounds (see Sec. III.A.3).

(c.) *Optical Depths.* The equivalent widths derived for each arc are rather consistent, given the azimuthal inhomogeneity seen in the highest-resolution Voyager images (Sec. II.A.2). The two Earth-based cuts of the  $4^\circ$  long Egalité arc are separated by  $2.0^\circ$  in corotating longitude, but yield equivalent widths (including any shoulders) which differ by less than 10%. This similarity is supported by the optical depths derived from square-well model fits to the arc cores of 0.13 to 0.15 and 0.12 to 0.14 for the July 22, 1984 and August 20, 1985 data, respectively (Hubbard et al. 1986; Sicardy et al. 1991; Nicholson et al. 1990). [All of the optical depths quoted in this section correspond to  $Q_{\text{occ}} = 2$ ; geometric equivalent depths  $A_g$  and optical depths  $\tau_g$  are expected to be approximately one-half of these values.]

The two poorer-quality Earth-based observations of the region near the  $4^\circ$  long Liberté arc are separated by  $4.0^\circ$  in longitude (though the orbital radii differ by  $\sim 240$  km). The equivalent widths from these occultations are  $E_o = 0.9 \pm 0.3$  km (for June 7, 1985) and  $E_o = 1.7 \pm 0.3$  km (for July 9, 1988) at  $\lambda 2.2 \mu\text{m}$ . (For the alternate mean motion, the June 7, 1985 observation actually refers to the Egalité 1 arc rather than to Liberté.) The Voyager PPS/UVS occultation gives an average ultraviolet equivalent depth for the Liberté arc of  $A = 0.71 \pm 0.13$  km. (As noted above,  $Q_{\text{occ}} \approx 2$  for both the Earth-based and Voyager occultations, unless most of the particles have radii  $\gtrsim 1$  cm, which seems unlikely.) In all three cases the quoted equivalent width or depth includes the substantial exterior shoulder, which accounts for 30 to 50% of the total. Equivalent widths for the “core” are estimated at 1.1 km (July 9, 1988) and 0.5 km (PPS), with average core optical depths of  $\sim 0.08$  and 0.034, respectively.  $E_o$  and  $\tau$  for the June 7, 1985 occultation are not available, though inspection of Fig. 10b indicates  $E_o(\text{core}) \sim 0.75 E_o(\text{full}) \sim 0.7$ . One may interpret the smaller equivalent widths, either for the core or the full arc, inferred from the PPS and June 7, 1985 observations, compared with those of July 9, 1988, along with the discrepant orbital radius for the latter event, as confirmation that the July 9, 1988 occultation did *not* cut the Adams ring. Alternatively, these differences may be genuine. In this regard, it is worth recalling the azimuthal brightness variations apparent in Voyager images of the arcs (Sec. II.A.2): occultation chords which sample different longitudes of the same arc may well produce different values of equivalent and optical depths. In particular, the apparent track of the star in the PPS occultation

grazed the leading edge of this arc, where the optical depth is almost certainly smaller than at the arc's center. It may be possible to use the longitudinal brightness profile of the arc (cf., Fig. 5) to correct the PPS equivalent depth to the center of the arc.

Because of the above complications, the only unambiguous data on wavelength dependence in the arc optical depths come from the July 22, 1984 occultation, where observations at both  $\lambda=0.8$  to  $0.9\text{ }\mu\text{m}$  and at  $\lambda=2.2\text{ }\mu\text{m}$  were obtained (Hubbard et al. 1986), and from the comparison of Voyager PPS and UVS  $\sigma$  Sgr results. Model fits to the 1984 data gave nearly identical estimates of ring width and mean optical depth at both wavelengths (0.12–0.13, corrected to a ring inclination of  $19.3^\circ$ ). (All remaining Earth-based observations were made at  $\lambda=2.2\text{ }\mu\text{m}$ .) Additionally, as noted above, the PPS and UVS equivalent depths are also statistically indistinguishable, with the shorter wavelength UVS value actually being slightly less than the PPS measurement, opposite to the trend expected for most particle size distributions. Both sets of results are surprising, given the substantial amounts of sub-micron sized dust inferred to exist in the arcs from imaging observations (see Sec. II.C), although Showalter et al. (1987) have shown that a power-law dust size distribution with index  $q \simeq 3$  can lead to optical depths which are nearly independent of wavelength.

The situation for the Le Verrier ring is much more uncertain, with only two tentative occultation detections listed in Table V. Nevertheless, the data at least marginally support the notion that the equivalent depth in the ultraviolet is somewhat higher than that in the near-infrared. The PPS equivalent depth, integrated over a ring width of 113 km, is  $700 \pm 200\text{ m}$  (Horn et al. 1990), compared with an equivalent width of  $520 \pm 55\text{ m}$  obtained for the 135 km wide feature in the August 20, 1985 data, and the upper limit of  $E_o \leq 150\text{ m}$  for correlated features up to 50 km wide established by Sicardy et al. (1991). The corresponding mean optical depths are  $0.0062 \pm 0.0015$  for PPS and  $0.0038 \pm 0.0004$  for the Earth-based (near-infrared) observation.

### C. Ring Particle Properties

Imaging and occultation data may be used together to derive constraints on the properties of Neptune's ring particles, complementary to those obtained by *in situ* measurements of  $\mu\text{m}$ -sized ring particles (Sec. II.A.5). The derivation of such characteristics as single scattering albedo  $\tilde{\omega}_0(\lambda)$  and phase function  $P(\phi, \lambda)$  from measurements of ring brightness  $I/F(\phi, \lambda)$  and optical depth  $\tau(\lambda)$  has been reviewed elsewhere (Cuzzi et al. 1984). In summary, the reflectivity of an optically thin ( $\frac{\tau}{\mu} \ll 1$ ) ring—the only case applicable to Neptune's rings, viewed from an emission angle  $\epsilon$  to the normal, is given by

$$I/F(\phi, \lambda) = \frac{\tilde{\omega}_0(\lambda) P(\phi, \lambda) \tau(\lambda)}{4\mu} \quad (9)$$

where  $\mu = \cos \epsilon$  and  $\phi$  is the solar phase angle. The phase function is

normalized over all solid angles such that

$$\int P(\phi) d\Omega = 4\pi. \quad (10)$$

The optical depth may be written (cf., Eq. 8) as

$$\tau(\lambda) = \int n(r) Q_{\text{ext}}(r, \lambda) \pi r^2 dr \quad (11)$$

where  $r$ ,  $Q_{\text{ext}}(r, \lambda)$ , and  $n(r) = n(r_0)(r_0/r)^q$  are the particle radius, extinction efficiency, and vertically integrated differential size distribution, respectively.

Note that the optical depth appropriate to an observation of scattered light may differ from that measured in an occultation experiment (cf., Eq. 8 above), due to differences in wavelength and in the effective extinction efficiency. Formally,  $Q_{\text{ext}} = 2$  for macroscopic ( $r >> \lambda$ ) particles, but for this size regime it is common to neglect in light scattering calculations the exceedingly narrow forward-scattering peak due to diffraction, and to set  $Q_{\text{ext}} = 1$ . This requires that both  $P(\phi)$  and  $\tilde{\omega}_0$  are defined consistently in a way which excludes the diffracted component of the scattered light for macroscopic particles. In this situation, we shall use the explicit notation  $\tau_g$ , defined in Sec. II.B.

In general, with a stellar occultation determination of  $\tau(\lambda)$  and measurements of  $I/F(\phi, \lambda)$  determined from imaging data at a range of phase angles for the same point on a ring, one can deduce both  $\tilde{\omega}_0(\lambda)$  and  $P(\phi, \lambda)$ . Ockert et al. (1987) followed such an approach for the narrow Uranian rings, as did Cooke (1991) and Dones et al. (1993) for Saturn's C and A rings. From these quantities, particle properties such as composition, size distribution and shape may be inferred and/or constrained. A complicating factor for the Neptunian rings is the azimuthal inhomogeneity of the Adams ring and its arcs, and the resulting difficulty in relating imaging and occultation measurements.

Alternatively, one may begin by restricting the range of likely particle albedos and phase functions and use imaging data alone to deduce  $\tau$ . Showalter et al. (1987, 1991; Showalter and Cuzzi 1993) employed this approach in studying the Jovian and faint Saturnian E and G rings. Smith et al. (1989) and Showalter and Cuzzi (1995) assume particle albedos and phase functions based partly on analogy with other ring systems in order to infer optical depths and dust fractions for the various components of the Neptunian ring system. We review both approaches below, finding generally consistent optical depths and albedos from these two disparate methods.

*1. Ring and Arc Photometry from Imaging Data.* As described in Sec. II.A, the bulk of Voyager imaging data on the Neptune rings falls at two well-separated geometries,  $\phi \approx 135^\circ$  and  $\phi \approx 14^\circ$ , which sample the light scattered from two well-characterized particle size regimes, respectively: microscopic particles with  $10^{-1} < r/\lambda < 10^2$ , and macroscopic particles with  $r/\lambda > 10^3$ . (Particles smaller than  $0.1\lambda$  are inefficient scatterers and may be neglected, unless the particle size distribution is very steep; in fact such

steep distributions have been inferred for some very dusty rings (Showalter et al. 1992; Showalter and Cuzzi 1993). Microscopic particles exhibit fairly diagnostic forward scattering behavior, and can be modeled with a combination of Mie scattering and simulated phase functions, applicable to realistic irregular particles (Pollack and Cuzzi 1980; Smith et al. 1989; Showalter and Cuzzi 1995). Macroscopic particles are predominantly backscattering, with phase functions similar to those of individual moons, and are assumed to have  $Q_{\text{ext}} = 1$ , as discussed above. The angular scattering of light by particles in the intermediate size regime is not so well characterized (cf., Dones et al. 1993; Cooke 1991), due to a transitional behavior that is neither strongly forward scattering nor backscattering. Furthermore, these intermediate-sized particles span roughly one decade in particle radius ( $r \sim 50$ – $500 \mu\text{m}$ ), compared to the three decades spanned by microscopic particles and the six decades spanned by macroscopic particles. For both these reasons, one probably introduces only small errors in inferred particle properties by neglecting their contribution to light scattering at low or high phase angles, barring an unusual size distribution which strongly weights their abundance.

As discussed in Sec. II.A, Voyager image smear and inherent resolution limitations varied widely and almost always prevented resolution of the narrower rings and the arcs. These image blurring effects are circumvented in a fashion similar to that used in stellar occultation studies by constructing a smear-invariant equivalent width,  $E_i$ . In the case of imaging measurements,  $E_i$  is the radial integral of the ring reflectivity, corrected to normal viewing geometry:

$$E_i = \mu \int (I/F) \, dR. \quad (12)$$

For the optically thin case (Eq. 9),

$$E_i = \frac{\langle \tilde{\omega} P \rangle}{4} \int \tau_{\text{vis}} \, dR. \quad (13)$$

Writing  $f = \tau_{\text{dust}}/\tau_{\text{vis}}$  as the optical-depth weighted fraction of microscopic dust, the albedo-phase function product may be written schematically as:

$$\langle \tilde{\omega} P \rangle = f \tilde{\omega}_{\text{dust}} P_{\text{dust}} + (1 - f) \tilde{\omega} P_L \quad (14)$$

and  $\tau_{\text{vis}} = \tau_{g,L} + \tau_{\text{dust}}$ . Here,  $\tilde{\omega}$ ,  $P_L$  and  $\tau_{g,L}$  refer to the single scattering albedo, phase function and geometric optical depth of the large particles, while for the microscopic particles we may write (cf., Eq. 11):

$$\frac{1}{4\mu} \int_0^{r_*} \tilde{\omega}_0(r, \lambda) P(r, \lambda) n(r) Q_{\text{ext}}(r, \lambda) \pi r^2 \, dr \simeq \frac{\tilde{\omega}_{\text{dust}} P_{\text{dust}}}{4\mu} \tau_{\text{dust}} \quad (15)$$

where  $r_*$ , the upper cutoff for small particles, is  $\sim 50 \mu\text{m}$ . None of the factors on the right-hand side of Eq. (15) is rigorously meaningful individually,

because of the complex wavelength and size dependences of  $\tilde{\omega}$ ,  $P$  and  $Q_{\text{ext}}$ , but this approach does provide a convenient way to parameterize the overall scattering behavior of a ring when relatively little phase data are available. Note, specifically, that while  $\tau_{g,L}$  is well defined,  $\tau_{\text{dust}}$  is not easily related to the geometric cross section of the small particles without detailed calculations. Nevertheless, for a given set of assumed large- and small-particle phase functions,  $\tau_{\text{vis}}$  is the quantity determined photometrically.

With measurements at widely separated phase angles, and assumptions concerning the phase functions and albedos for small and large particles, these equations can be solved for  $f$  and  $\int \tau_{\text{vis}} dr$  for the various ring elements. Note that all of the *angular* dependence in Eq. (13) above arises from the (composite) phase function, which is in turn determined by the particle size distribution (Eq. 14). In forward scattering, the dominant scattering is size-dependent and, with observations taken over a range of scattering angles, one may fit for the *form* of the distribution of the forward-scattering dust component alone, independent of the normalization constant (see, e.g., Fig. 17). Light is backscattered by all particle size regimes to different degrees (see, e.g., the Appendix of Cuzzi et al. [1984]; also Fig. 18). With this information as a constraint, one may then determine the particle abundance, or radially integrated optical depth, which matches the observed intensities (Fig. 19, left panel). In those instances when independent knowledge of the physical radial width  $W$  of a ring exists from either occultation or high-resolution imaging data, one may then obtain the average optical depth,  $(\int \tau dr)/W$ , for each region at the observed wavelength. This leads to results such as those in the right panel of Fig. 19.

Recent work deducing the photometric properties of the Neptune rings, improving on the data reduction techniques of Smith et al. (1989), has been presented (Showalter and Cuzzi 1992b; Ferrari and Brahic 1991), and is being continued by Showalter and Cuzzi (1995) and Ferrari and Brahic (1994). Below we summarize the current state of understanding.

(a.) *Variations in Particle Size Distributions.* Results from Showalter and Cuzzi (1992b, 1995), comparing the observed phase variation of  $E_i$  with theoretical predictions for various differential *small* particle size distributions,  $n(r) = n(r_0)(r_0/r)^q$ , are shown in Figs. 17 and 18. The  $E_i$ 's in these figures differ significantly in some cases from those derived in Smith et al. (1989). Smith et al. (1989) assumed a dust power law size distribution ( $n(r) \propto r^{-2.5}$ ) similar to that found for the Jovian and Uranian rings (Showalter et al. 1987; Ockert et al. 1987). However, recent studies have raised the possibility that dust particle size distributions in Saturn's F and G rings might be much steeper than in the Jovian and Uranian cases (Showalter et al. 1992; Showalter and Cuzzi 1993). For the F and G rings, very steep power laws ( $q = 4.5$  and  $q = 6$ , respectively) are observed, with scattering dominated by extremely tiny particles. Furthermore, recall that the *in situ* particle size distribution measurements of Pedersen et al. (1991) showed  $n(m) \propto m^{-2}$ , or for particles whose density is independent of size,  $n(r) \propto r^{-4}$  (see Sec. II.A.4).

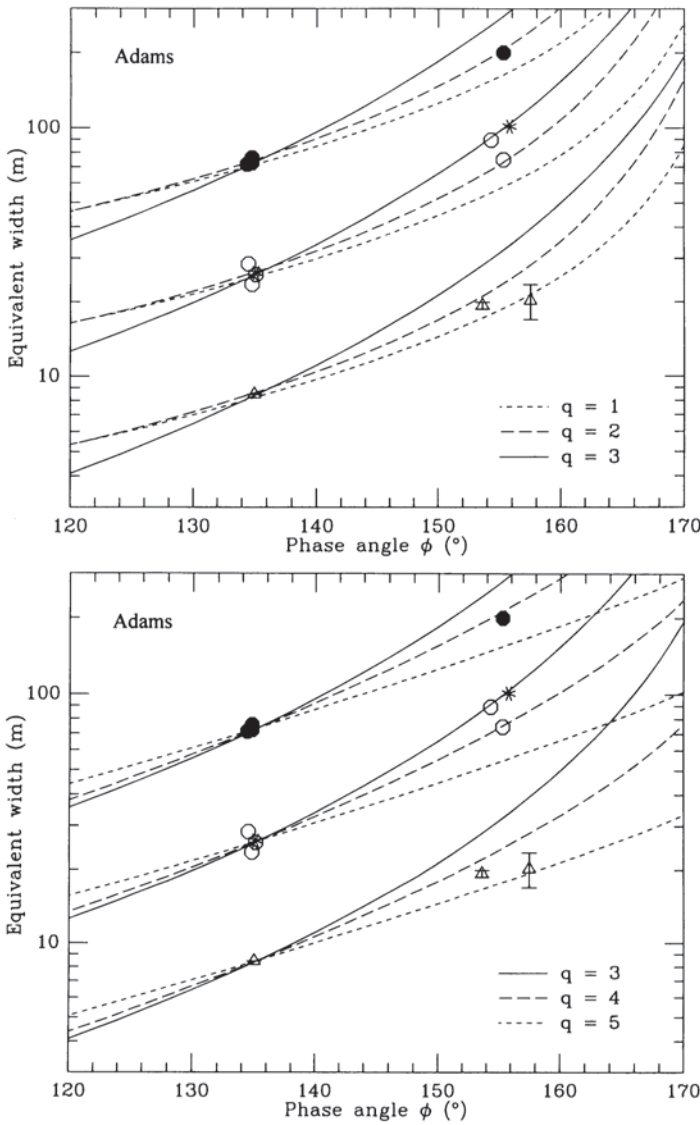


Figure 17. Photometric measurements of the Adams ring (Showalter and Cuzzi 1992b, 1995), including data with phase angles higher than those utilized by Smith et al. (1989), and various *dust* particle size distributions of the form  $n(r)dr = n_0(r_0/r)^q dr$ . Filled circles—arcs; open circles—inter-arc regions; triangles—location of minimum brightness in non-arc regions; asterisks—the Courage arc. (See Sec. II.A.2 for a discussion of the Adams ring azimuthal structure.) Note the ambiguity between powerlaw indices  $q = 2$  and  $q = 4$ , and between  $q = 1$  and  $q = 5$  over the region of phase angle sampled. This ambiguity has implications for modeling the low phase angle brightness of the ring. (Distributions steeper than  $q = 3$  are dominated by the smallest particles in the dust distribution; those flatter than  $q = 3$  are dominated by the largest dust particles.) Figure courtesy of M. Showalter.

Comparisons of observations and modeling in Figs. 17 and 18 show that it is impossible to rule out such steep distributions in the Neptunian case (Showalter and Cuzzi 1995). In the case of the arcs, the similarity of PPS ( $\lambda 0.26 \mu\text{m}$ ) and UVS ( $\lambda 0.11 \mu\text{m}$ ) optical depths argues against such steep distributions, but the same cannot be assumed to apply to the continuous rings.

For the Lassell Ring, preliminary photometric results (Showalter and Cuzzi 1995) indicate a different mix of particle sizes than for the Adams and Le Verrier rings; either Lassell has a significantly larger fraction of macroscopic particles, or it is predominantly composed of tiny Rayleigh scatterers ( $r << \lambda$ ). (Compare the top and bottom panels of Fig. 18.) Along similar (rather qualitative) lines, Ferrari and Brahic (1991, 1994) and Showalter and Cuzzi (1992b, 1995) have noted that the Courage arc is noticeably less forward scattering than the remaining arcs, with implications similar to those for the Lassell ring. Showalter and Cuzzi (1992b, 1995) also note that Fraternité is slightly more forward scattering than Liberté or Egalité. Ferrari and Brahic (1994) find that the arcs are less forward scattering than the Adams ring proper, and that the clumps in the arcs have similar scattering properties to the non-clump arc material. However, more detailed modeling of light scattered from the planet onto the rings, which complicates the analysis of many Voyager ring images, must be completed before these results may be interpreted in terms of particle properties.

(b.) *Optical Depths and Dust Fractions.* Large particle albedos and phase functions, and small particle size distributions, similar to those of the Uranian ring particles (Ockert et al. 1987) were adopted by Smith et al. (1989) to calculate  $f$  and  $\int \tau_{\text{vis}} dR$  from measurements of  $E_i$  and then to derive average optical depths for an assumed common ring width of 15 km. The results of Smith et al. (1989) are updated in Fig. 19, following Showalter and Cuzzi (1992b). In the left-hand panel, the narrow rings and arcs appear more strongly forward scattering, with steeper slopes in brightness vs phase angle, than do the broad rings. Showalter and Cuzzi (1992b) show that the uncertainties given by Smith et al. (1989) for the very small  $I/F$  of the Galle and Lassell rings at low phase angles were underestimated.

Updated optical depths and dust fractions are shown in the right-hand panel of Fig. 19. The boundaries of each diamond-shaped region are the solutions  $(f, \tau_{\text{vis}})$  associated with  $\tilde{\omega}_L \approx 0.01$  and 0.02, and dust particles of silicate and coal composition. These are model fits of two parameters to only two observations, and thus are not overdetermined. It is worth noting, however, that a differential power law size distribution with  $q = 2.5$  was assumed in producing Fig. 19, while Figs. 17 and 18 indicate that either a higher or lower  $q$  might be more appropriate. A  $q$  differing from that assumed would tend to increase the value of  $f$ .

The resulting  $\tau$  for the arcs is on the order of  $10^{-1}$ , roughly consistent with that observed in most occultation observations. The optical depths shown here for the narrow continuous rings appear larger than the upper limits more recently determined from the groundbased stellar occultation observations

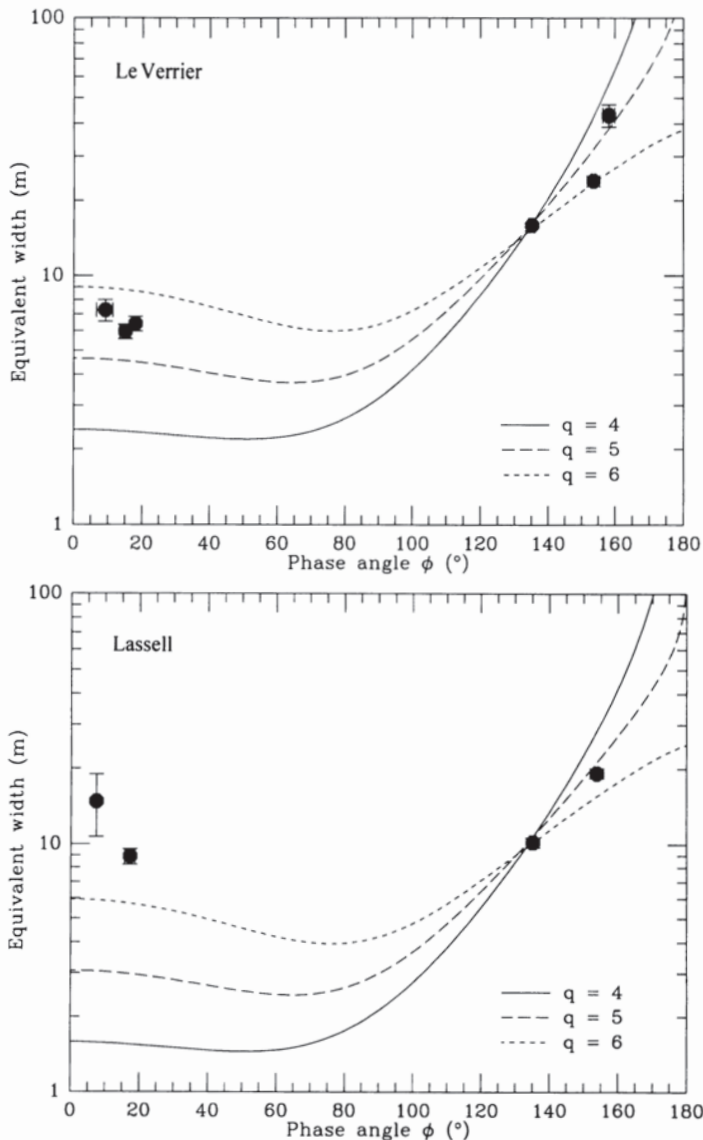


Figure 18. Phase variation of the reflectivity of the Le Verrier ring (top) and Lassell (bottom) (Showalter and Cuzzi 1992b, 1995). Various dust particle size distributions are shown. As discussed in the text, Lassell may have a different particle size distribution than the Le Verrier ring (figure courtesy of M. Showalter).

(see Secs. II.B.2 and II.B.4), but this is largely due to the narrow ring widths of  $W = 15$  km assumed here; for  $W = 50$  km, the inferred  $\tau_{\text{vis}}$  for the Adams ring is  $\sim 0.0045$ , comparable with the upper limits set by Sicardy et al. (1991) and Nicholson et al. (1995) of  $\tau_{\text{occ}} \leq 0.003(50/W)$  and  $\tau_{\text{occ}} \leq 0.002(50/W)$ ,

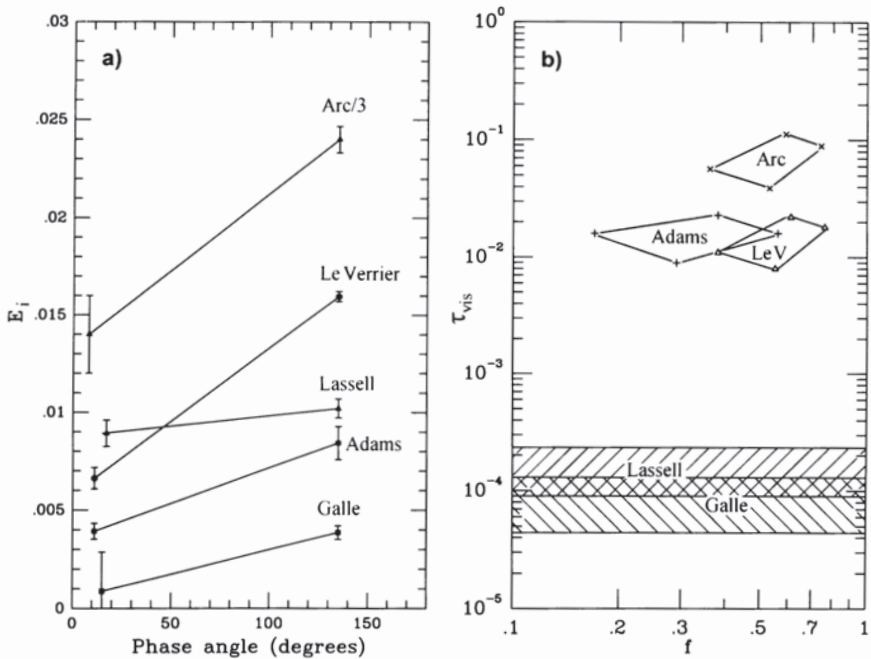


Figure 19. Implications and uncertainties in the properties of different ring regions as constrained by Voyager photometry alone. (a) Measured values of equivalent width  $E_i$  taken from Voyager imaging data. The value for the arcs has been divided by 3 (figure is modified from Smith et al. 1989 following Showalter and Cuzzi 1992b). (b) The boundaries of each diamond-shaped region are the solutions ( $f, \tau_{\text{vis}}$ ) associated with  $\tilde{\omega}_L \approx 0.01$  and 0.02, and dust particles of silicate and coal composition. A differential power law size distribution of the form  $n(r) \propto r^{-2.5}$  has been assumed. The uncertainty in both ring reflectivity and particle size distribution for the Galle and Lassell rings leaves the dust fraction in these rings unconstrained at present (cross-hatched regions). The optical depths for the narrow rings appear larger than the upper limits recently determined from the groundbased stellar occultation observations (see Secs. II.B.2 and II.B.4), largely because the ring widths of 15 km assumed for the Adams and Le Verrier rings in the photometric analysis differ from those assumed in deriving the optical depths from occultation data. (See text.)

respectively. If the true width of the Le Verrier ring is as great as  $\sim 120$  km, as suggested by the occultation data, then the inferred  $\tau_{\text{vis}} \approx 0.002$ . Further analysis of the Voyager imaging data to constrain the physical width, and thus the optical depths, of the Adams and Le Verrier rings is highly desirable. Ferrari and Brahic (1994) obtain similar dust fractions for the Adams and Le Verrier rings, but in contrast to the results shown in Fig. 19, they believe that these rings have quite similar scattering properties. These differences are unresolved at present.

The uncertainties in particle size distribution and in the low phase angle measurements of the Galle and Lassell rings prevent a reliable determination

of dust fractions for these rings at this time.

(c.) *Composition.* Ferrari and Brahic (1994) have used the previously described information on ring arc optical depths to derive added constraints on the refractive indices of the ring particles; their conclusion is that the ring particle refractive indices best match a “dirty ice” composition (imaginary refractive index less than  $10^{-1}$  or so), rather than a highly absorbing carbon-rich material. Because a refractive index of this magnitude is appropriate for a large variety of silicates, we would expect that silicate particles would also be candidates, even though the specific set of refractive indices denoted “silicates” by Ferrari and Brahic does not provide a good fit to the data. The color of the ring particles was another constraint explored by Showalter and Cuzzi (1992b). Although no specific observations were obtained in any of the Voyager color filters, a good mix of wide angle and narrow angle images was obtained through their respective clear filters, which actually have slightly different wavelength responses (cf., also Doyle et al. 1989). The effective wavelengths for the Voyager WA and NA clear filters are  $0.51\text{ }\mu\text{m}$  and  $0.47\text{ }\mu\text{m}$ , respectively. Based on consistent differences between the ring brightness in the wide angle and narrow angle images, Showalter and Cuzzi (1995) concluded that the Neptune ring particles are as red as Amalthea or the Jovian ring—much redder than the main Uranian rings (Porco et al. 1987).

*2. Particle Properties Derived from Imaging and Occultation Data.* As discussed in Sec. II.B, stellar occultations provide estimates of, or upper limits on, Neptune ring and arc optical depths. Because of uncertainty in the arc mean motion, however, there remains some doubt as to exactly which arc each Earth-based occultation profile represents (cf., Fig. 20). There is only one case in which this association is unequivocal: the Voyager PPS/UVS  $\sigma$  Sgr occultation of the Liberté arc. In this case, unfortunately, the star’s path grazed the leading edge of the arc, resulting in an optical depth which is probably uncharacteristic of the central portion of the arc where imaging measurements are most reliable. Small-scale clumpiness observed within the arcs (Smith et al. 1989; Porco 1991; Ferrari and Brahic 1994) further complicates the association of occultation measurements with average arc optical depths. With these caveats, Ferrari and Brahic (1994) used “typical” arc optical depths obtained from stellar occultations to infer “typical” particle dust fractions and composition, as discussed above.

Here we adopt a somewhat different approach, and attempt to infer directly the albedo of the large ring particles, independent of *a priori* compositional assumptions. While the forward scattering observations constrain the small particle size distribution in the rings, as shown in Fig. 17, the brightness of the rings in backscatter may be determined primarily by the single scattering albedo of the larger particles,  $\tilde{\omega}_L$ , and the component of the overall optical depth due to “large” particles,  $\tau_L$  ( $r \gtrsim 500\text{ }\mu\text{m}$ , roughly). (This will not be true for large values of  $f$ , or for very steep particle size distributions.) The optical depths obtained from stellar occultation observations, as discussed in Sec. II.B.4, apply to particles of radii  $r \geq \lambda/3 \sim 0.7\text{ }\mu\text{m}$ , roughly. We as-

sume here, in the absence of detailed knowledge of the size distributions, that the occultation optical depths provide a direct measure of the large particle population.

Because of resolution limitations in both the imaging and occultation data, we compare only radially integrated quantities. From Eqs. (6) and (13) we see that the imaging and occultation equivalent widths are related by

$$E_i(\phi) \simeq \frac{1}{4} \langle \tilde{\omega} P(\phi) \rangle \left( \frac{\tau_{\text{vis}}}{\tau_{\text{occ}}} \right) A. \quad (16)$$

Because  $E_o \simeq A$  for  $\tau << 1$ , the imaging equivalent width at zero phase angle is

$$E_i = p(1-f) \left( \frac{\tau_{\text{vis}}}{\tau_{\text{occ}}} \right) E_o \quad (17)$$

where  $p = \langle \tilde{\omega}_L P_L(0) \rangle / 4$  is the average geometric albedo of the large ring particles and we have neglected the contribution of small ( $r \lesssim 500 \mu\text{m}$ ) particles to the backscatter brightness. If we further assume that the occultations essentially measure the optical depth in large particles, then  $(1-f)\tau_{\text{vis}}/\tau_{\text{occ}} = \tau_L/\tau_{\text{occ}} \simeq Q_{\text{ext}}/Q_{\text{occ}} = 0.5$ , where we have taken  $Q_{\text{ext}} = 1$  for the macroscopic particles, as discussed above. (This assumption may not be valid if there is a large fraction of particles in the 1 to  $500 \mu\text{m}$  range, i.e., if there is a very steep particle size distribution.)

Extrapolating the measured values of  $E_i$  between  $7.8$  and  $18.4^\circ$  (Showalter and Cuzzi 1995) to  $\phi = 0^\circ$  using a typical large particle phase function derived from observations of icy satellites (cf., Dones et al. 1993)\*, and using the measurements of  $E_o$  from Table V for the Egalité arc and the Le Verrier ring, we obtain the values of  $\tilde{\omega}_L$  and  $p$  listed in Table VII. For the Le Verrier ring, we have used the tentative detection of Nicholson et al. (1995) discussed in Sec. II.B.2, while for the non-arc region of the Adams ring we have used the upper limit of  $E_o \leq 150 \text{ m}$ , set by Sicardy et al. (1991); see Sec. II.B.2 for regions  $75^\circ$  or more away from the arcs. (Showalter and Cuzzi [1995] find a factor of 3 variation in  $E_i$  for the Adams ring from a maximum in the arc region to a minimum which is reached  $\sim 180^\circ$  away from the arcs.)

TABLE VII  
Large Particle Albedos<sup>a</sup>

Ring Region	Egalité Arc	Adams Ring	Le Verrier Ring
$E_i(\text{m})^b$	$52 \pm 2.5$	$5.4 \pm 0.6$	$8.4 \pm 0.8$
$E_o(\text{m})^c$	$1900 \pm 100$	$< 150$	$520 \pm 55$
$\tilde{\omega}_L$	$0.038 \pm 0.003$	$> 0.05$	$0.022 \pm 0.002$
$p$	$0.055 \pm 0.004$	$> 0.07$	$0.032 \pm 0.003$

<sup>a</sup> Based on several assumptions; see caveats in text.

<sup>b</sup> From the measured visible  $I/F$ , extrapolated to zero phase (Showalter and Cuzzi 1995).

<sup>c</sup> Measured occultation equivalent width, or upper limit, at  $\lambda 2.2 \mu\text{m}$ .

\*  $P_L(\phi) = C_n(\pi - \phi)^n$ , with  $n = 3.33$  and  $C_n = 0.1273$ , for which  $P_L(0) = 5.759$ .

From these results, we see that the data for the *Egalité* arc and the Le Verrier ring are consistent with  $\tilde{\omega}_L \simeq 0.04$  and 0.02, respectively (or  $p \simeq 0.06$  and 0.03). However, the lower limit obtained for the non-arc region of the Adams ring is rather larger than that of the arcs, provided that the (unknown) width of this ring is no greater than 50 km. This result also can be seen more directly from the ratio of ring to middle arc brightness of  $\geq 0.10$  found by Showalter and Cuzzi (1995) vs the comparable ratio of occultation equivalent widths of  $\leq 0.05$  found by Nicholson et al. (1995) and  $\leq 0.08$  found by Sicardy et al. (1991). There is thus a suggestion that the large particle albedo in the Adams ring is greater than that of the arcs or the Le Verrier ring, though this must be regarded as a provisional result pending a more complete photometric analysis. Alternatively, small ( $r \lesssim 500 \mu\text{m}$ ) particles may make a more significant contribution to the backscatter brightness of the Adams ring away from the arcs. This is compatible with the view that the main body of this ring is composed of particles "leaking away" from the arcs, where larger particles are gravitationally confined (see Sec. III.A).

The above results carry several assumptions. It is assumed that (a) the maximum Adams ring width is 50 km (a ring width greater than 50 km would lead to an underestimate of the true  $E_o$ , and thus an overestimate of the albedo); (b)  $\mu\text{m}$ - to mm-sized particles do not contribute significantly to either the occultation optical depth or the visible reflectivity at low phase of the rings; (c) the scattering efficiency for large particles is  $Q_{\text{ext}} = 1$ ; and (d) the Adams ring outside of the arc region is azimuthally smooth. Neither (a) nor (b) is supported by any data, and (b), in particular, could well be violated. This should be borne in mind when interpreting the error bars quoted in Table VII.

The results presented in this section could be strengthened (or altered) considerably by additional occultation detections of the Le Verrier ring, by a determination from Voyager images of the radial width of the Adams ring away from the arcs, and by a comprehensive photometric analysis incorporating both imaging and occultation observations.

### III. KINEMATICS AND DYNAMICS

The greatest dynamical challenge presented by the Neptune ring system, and the only one which received attention prior to Voyager's arrival at Neptune, lies in explaining the longitudinally limited arcs which, if unconfined, would spread into a complete ring in a matter of years. The suite of pre-Voyager models of arc confinement which has proven most promising in the post-Voyager era proposes the resonant radial and azimuthal confining action of nearby satellites as an explanation for the arcs.

A fruitful search for dynamical associations between ring edges and nearby satellites requires high precision in the orbital elements of both: in particular the mean motions, and concomitantly, the semimajor axes. This is because of the demonstrated importance of mean motion commensurabilities in the confinement of rings (see, e.g., Porco et al. 1984*a, b*). Specifically, a ring

edge and candidate resonance must be coincident to within the natural width of the resonance, which in turn must be greater than the uncertainties in both the ring and satellite radial locations. As an example, the relative uncertainty in the mean motion  $n$  and semimajor axis  $a$  of the Uranian satellite Ophelia, which confines the outer edge of the  $\epsilon$  ring via a Lindblad resonance (Porco and Goldreich 1987), is  $\delta n/n \sim \delta a/a \sim 10^{-5}$  (Owen and Synnott 1987). The uncertainty in the location of the ring's outer edge is comparable (French et al. 1988). The relative resonance width is  $\sim 10^{-4}$ .

For a full dynamical study, the whole suite of orbital elements, including eccentricity, inclination, and the rates of change and positions of the nodes and apses, are generally necessary. This type of information on Neptune's rings and arcs was unavailable until the Voyager encounter. Measurements taken from both Voyager and groundbased observations have now been used to derive a likely value for the arcs' mean motion, and measurements taken from Voyager observations alone have been used to determine the arcs' geometry and orbital kinematics, and the locations and orientations of the Le Verrier and Galle rings. In this section, we discuss the construction of kinematic and geometric models of the Neptunian rings, and the dynamical scenarios which might account for the rings' appearances. In Sec. III.A, we concentrate on current models for the arcs, implicitly assuming that the orbital plane of the arcs is identical to that of the entire Adams ring. In Sec. III.B, we present the results in hand for the Le Verrier and Galle rings, and in Sec. III.C, current ideas regarding the occurrence of dust on high-inclination orbits within the Neptune rings are discussed.

### A. The Arcs and the Adams Ring

*1. Dynamical Models for the Arcs.* A dynamically unconfined arc of particles in an unperturbed Keplerian orbit about a planet would spread at the rate:

$$\frac{d(\Delta\theta)}{dt} = \frac{3}{2} \frac{\Delta a}{a} n \quad (18)$$

where  $\Delta\theta$  is the azimuthal extent (angular length) of the arc in radians;  $\Delta a$  is the full spread in the orbital semimajor axes of the ring particles, usually assumed to be identical to  $W$ , the radial width of the ring;  $n$  is the mean orbital angular frequency of the ring particles; and  $a$  is the mean ring semimajor axis. Assuming an arc width  $W = \Delta a = 15$  km, the particles at the inner edge of Neptune's arcs would make one more orbit of Neptune than those at the arc's outer edge, thereby completely destroying the arcs, in 3.4 yr. In fact, the Kepler shear across a 15 km ring is sufficiently large that an arc should lengthen by  $0.3^\circ \text{day}^{-1}$ , a rate which would have been observable in Voyager data. A consistent interpretation of all the data currently available on the arcs, groundbased and Voyager included, is that the arcs observed by Voyager in the Adams ring are similar, if not the same, structures seen from the ground up to 5 yr earlier (Sec. II.B). The arcs are evidently persistent features, requiring

a mechanism capable of perturbing ring particle orbits in such a way as to create azimuthal variations which last over time scales of years and longer.

A number of possibilities have been considered in explaining the persistent appearance of the arcs in the Adams ring. These fall into two basic categories: internal and external mechanisms.

(a.) *Internal Mechanisms.* Internal mechanisms which rely on instabilities in the ring to produce stable azimuthal structure are easily discounted as explanations for the Neptune arcs. Such instabilities have already been proposed as the causes of radial and azimuthal structures observed in Saturn's ring system (see, e.g., Franklin and Colombo 1978; Ward 1981; Stewart et al. 1984), and while no specific models of formation of arc rings by instabilities have yet been published, general considerations are illuminating.

Instabilities can be either gravitational, which rely on the self-gravity of the rings, or viscous, which depend on collisional properties of ring particles. Gravitational instabilities are unlikely to be important for Neptune's rings because the rings are within Neptune's Roche limit and have fairly low optical depth,  $\tau \sim 0.05$ . This can be demonstrated by examining Toomre's parameter  $Q$  which is a measure of the ratio of the effects of Kepler shear plus particle random motions to that of ring self-gravity:

$$Q \equiv \frac{c\kappa}{\pi G \sigma} \sim \frac{\rho_N}{\rho_r} \left( \frac{R_N}{a} \right)^3 \frac{h}{\tau \bar{r}} \quad (19)$$

where  $c$  is the velocity dispersion of the ring particles,  $\kappa$  is the epicyclic (radial) frequency (which is almost equal to the orbital frequency, as the potential is nearly Keplerian),  $G$  is the gravitational constant,  $\sigma$  is the surface density,  $\rho_N$  and  $\rho_r$  are the mass densities of Neptune and the ring particles, respectively,  $R_N$  is the radius of Neptune,  $a$  is the ring's orbital distance,  $h$  is the scale height of the ring and  $\bar{r}$  is the typical particle size. Though  $Q$  only provides a rigorous criterion for assessing the likelihood of the development of axisymmetric instabilities—i.e., when  $Q > 1$ , the growth of these instabilities is suppressed—non-axisymmetric disturbances such as wakes are also strongly suppressed when  $Q \gtrsim 2$  (Julian and Toomre 1966; Salo 1991). In the case of the Adams ring,  $Q \sim h/(10\tau \bar{r}) \gtrsim 2$ , the lower limit applying to a monolayer ring for which  $h/\bar{r} \sim 1$ . It is far more likely in the case of the arcs, which are largely dust, that  $h/\bar{r}$  is several orders of magnitude, making  $Q$  quite large. Thus, gravitational instabilities are not a viable mechanism for creating and maintaining the arcs in Neptune's rings.

Collisional instabilities are much more difficult to analyze in general terms than are those caused by ring self-gravity because of the difficulty in adequately characterizing the collisional environment and physical properties of the ring particles. However, most models of the production of radial variations in planetary rings due to collisional effects require much higher optical depths than are observed even in the arc regions of Neptune's Adams ring (see, e.g., Ward 1981; Stewart et al. 1984; Salo 1991). Such instabilities are thus not likely to be important in explaining Neptune's arcs.

Another suggestion is that all particles have almost exactly the same orbital semimajor axis, eliminating the need for confinement altogether. Three-dimensional braided ring structures consisting of “collisionless, co-orbiting” particles have been suggested for some of the structure observed in Saturn’s rings (Michel 1981). Such configurations are clearly unstable to perturbations and to slight changes in initial conditions, and thus do not present a viable morphological model for Neptune’s arcs. Two-dimensional (i.e., co-planar) eccentric particle orbits, sharing the same epicyclic guiding center, have been specifically suggested to explain the arcs, but these would have a longitudinal length to radial width ratio of 2/1, and thus are also not successful arc models.

However, a merged chain of unresolved epicyclic vortices might have the same aspect ratio as the observed arcs in the Adams ring. Motivated by the observations of small clumps within the arcs (Sec. II), Gor’kavyj (1991) hypothesized, and Gor’kavyj et al. (1991) and Gor’kavyj and Taidakova (1991) considered in more detail, relatively long-lived ensembles of 1 to 100 m radius objects, or “epitons,” which consist of particles having the same semi-major axis but a range of eccentricities, thereby executing nested epicyclic motion. However, as with Michel’s (1981) model, it is difficult to see how such structures come about and how they would persist in the presence of vigorous interparticle collisions, unless relative particle velocities were quickly damped. Gor’kavyj and collaborators mention both gravitational instability (in denser pre-existing material) and/or highly perturbed shear flows (perhaps due to Galatea’s forcing) as possible initiating and stabilizing circumstances, but the viability of these suggestions is presently untested. Moreover, it is unclear if the damping needed to stabilize epitons is quantitatively consistent with the physical environment of the Adams ring.

(b.) *External Mechanisms.* Several dynamical mechanisms, all invoking resonant perturbations on ring particles, have been proposed to explain the arcs. One of these hypotheses for arc maintenance proffered acoustic oscillations within Neptune as a source of an azimuthally varying gravitational potential perturbation on the ring particles (Lin et al. 1987). This mechanism, which has been shown to produce perturbations and torques on rings equivalent to those produced by satellite resonances (Marley and Porco 1993) was definitively refuted after the Voyager encounter with Neptune on the basis of a gross mismatch between the predicted angular speed of the requisite potential and the angular frequency of the arc particles (Marley et al. 1989). Also, the short arc lengths ( $\sim 4^\circ$ ) require impausibly large distortions in the very high harmonics of the planet’s gravity field.

The dusty nature of the Adams ring and the arcs opens up the possibility that the tiny ring particles might be confined to the arc locations via resonances with Neptune’s rotating and tilted magnetic field. However, the Adams ring is too narrow and not close enough to a Lorentz resonance (Sec. III.C) for this effect to be important in radial arc confinement, and there are no Lorentz resonance analogs to corotation resonances.

Other external mechanisms capable of confining ring material invoke

gravitational perturbations arising from corotation and Lindblad resonances of nearby satellites. The discovery of Galatea, and in particular the radial distortion traveling through the arcs attributable to Galatea (Sec. III.A.2), call for a brief discussion of these resonances.

Corotation resonances occur at radial locations where the mean orbital motion  $n$  of the perturbed particle equals the pattern speed  $\Omega_{\text{pat}}^c$  of the perturbing potential. Such resonances lead to slow libration around a mean orbit guiding center, or corotation site, by exciting small periodic variations in semimajor axis  $a$  and in longitude  $\theta$ . In the frame rotating with the pattern speed, the trajectory of a particle making a *small* amplitude libration takes the form of an ellipse, the minor axis of which may be identified with the range in particle orbital semimajor axes. (When the amplitude is large, the simple elliptical approximation no longer strictly applies. See Sec. III.A.3.) The strongest corotation resonances produced by a satellite are associated only with the satellite's orbital frequency  $n_s$ , i.e.,  $\Omega_{\text{pat}}^c = n_s$ . These are the familiar triangular Lagrange points,  $L_4$  and  $L_5$ , which lead and trail the satellite in its orbit by  $60^\circ$ . The next strongest corotation resonances are those associated with either satellite eccentricity only (CER) or satellite inclination only (CIR). For example, CIR resonances falling at radial locations outside the satellite's orbit (the geometry appropriate for Galatea and the arcs) have pattern speeds obeying the relation

$$m_c \Omega_{\text{pat}}^c = (m_c - 1)n_s + \dot{\Omega}_s \quad (20)$$

where  $\dot{\Omega}_s$  is the satellite nodal precession rate and the positive integer,  $m_c$  is the corotation resonance wavenumber.

The  $2m_c$  stable equilibrium points distributed around the orbit of a corotation inclination resonance are potential maxima. Interparticle collisions, and the attendant loss of energy, would cause any ring material which had collected near these equilibrium sites to spread in radius and, consequently, in azimuth. All pre-Voyager arc hypotheses proposed a nearby Lindblad resonance as the energy source which maintains the system of colliding particles in libration around a corotation site. Lindblad resonances excite variations in the particle's longitude of perapse  $\tilde{\omega}$ , and eccentricity  $e$ . The strongest Lindblad resonances always have pattern speeds equal to the mean motion of the satellite,  $\Omega_{\text{pat}}^L = n_s$ , and for an interior satellite are located where

$$m_L \Omega_{\text{pat}}^L = (m_L + 1)n - \dot{\tilde{\omega}}. \quad (21)$$

Here,  $\dot{\tilde{\omega}}$  is the particle's apsidal precession rate. The Lindblad resonance delivers the orbital energy required to maintain ring particle libration around the corotation site by exerting repulsive torques on the ring material; those particles on the satellite-side of their libration trajectories feel a larger repulsion than do those on the anti-satellite side. The resulting differential torque

across the corotation site serves to stabilize the material there and form a ring arc.

The gravitational tug of a moon can influence the dynamics of a nearby ring in a variety of ways (see, e.g., Goldreich and Tremaine 1979; Lissauer et al. 1981; Showalter and Burns 1982; Dermott 1984; Cuzzi and Scargle 1985; Showalter et al. 1986; Lissauer and Peale 1986; Borderies et al. 1989; Kolvoord and Burns 1992; Horanyi and Porco 1993). Ring particles falling near a Lindblad resonance experience perturbations which force their eccentricities and excite variations in their apses. As a result of these resonant perturbations, the apsidal lines of the orbits are aligned and phased such that the maximum (or minimum) possible radial separation occurs when a particle passes through conjunction with the moon. This phasing produces a scalloped pattern with symmetry number  $m_L$ , which remains stationary in the frame rotating with the moon. The radial amplitude of this pattern, determined by the satellite forcing, is given by:

$$ae \approx 0.53 \frac{M_s}{M_p} \left( \frac{m_L + 1}{m_L} \right)^2 \frac{a_s^2}{a - a_{\text{res}}} \quad (22)$$

where  $a_s$  and  $M_s$  are the satellite's semimajor axis and mass, respectively,  $(a - a_{\text{res}})$  is the distance of the ring from exact resonance, and  $M_p$  is the mass of the planet. Scalloped patterns produced by such resonances have been detected at the outer edges of Saturn's A and B rings (Smith et al. 1982; Porco et al. 1984b). Note that with a measurement of  $ae$  and  $a - a_{\text{res}}$ , and the assumption that the only force perturbing the ring particle orbits is that due to the satellite's resonant perturbations, one may derive an estimate for  $M_s/M_p$ . (See Sec. III.A.2.)

An analogous sinusoidal wavy pattern or wake can be produced by "short-period" perturbations after a single passage of Galatea. The wavelength of a wake would be nearly identical to that of a resonantly produced wave, but the phase of the pattern would be shifted by  $90^\circ$  (cf., Eq. 63 of Goldreich and Tremaine 1982). Also, wakes are by definition limited in azimuthal extent, due to the damping of particle eccentricities when the perturbed streamlines of ring material intersect between successive encounters with the satellite. The amplitude of the forced eccentricity of a wake would be (Julian and Toomre 1966):

$$ae \approx 2.24 \frac{M_s}{M_p} \left( \frac{a}{a - a_s} \right)^2 a. \quad (23)$$

*(c.) Lagrange-point Satellite Model.* Lissauer (1985) first demonstrated that two moons could together confine ring particles to a long narrow arc for extended periods of time via a combination of corotation and Lindblad resonances. One moon would share the orbit of the ring particles, which would librate about the moon's  $L_4$  or  $L_5$  triangular Lagrangian point, in a situation analogous to that of the Trojan asteroids and Jupiter, as well as to

several Saturnian moons. The maximum spread  $\Delta a_{\max}$  in semimajor axis of particles librating in such a configuration, and thus presumably the maximum width of the arc, is related to closest angular approach  $\theta_{\min}$  to the Lagrange moon by the formula:

$$\Delta a_{\max} = 4a \sqrt{\frac{2}{3} \frac{M_L}{M_P} [f(60^\circ) - f(\theta_{\min})]} = 4a \sqrt{\frac{2}{3} \frac{M_L}{M_P} |f(\theta_{\min}) + 0.5|} \quad (24)$$

where  $M_L$  is the mass of the Lagrange moon and

$$f(\theta) \equiv \cos(\theta) - \frac{1}{2 \sin(\frac{\theta}{2})} \quad (25)$$

(Lissauer 1985). The angular extent of the arc is given by:

$$\Delta\theta = \theta_{\max} - \theta_{\min} \quad (26)$$

where the maximum angular separation  $\theta_{\max}$  between the particle and the Lagrange moon is a solution of  $f(\theta_{\max}) = f(\theta_{\min})$ .

To overcome the dissipative effects of the inelastic collisions which arc particles would undoubtedly undergo, Lissauer (1985) added a second satellite on a nearby orbit to provide through its Lindblad resonances the torque and energy necessary to balance the collisional losses. The width of these resonances, for the case where the ring's self-gravity is unimportant (a likely case for the arcs) is given by  $W_L \sim (M_s/M_P)^{1/2} a_s$ , where  $M_s$  is the mass of the second shepherding satellite and  $a_s$  is that satellite's orbital semimajor axis. This model predicts one stable arc radius per Lagrange moon, and places much stronger constraints on the mass of the Lagrange moon than on that of the shepherding moon: i.e., while the former constrains the shape of the arc, the latter is merely a long-term energy source, resupplying the losses due to collisions. Although Voyager discovered a satellite (Galatea) sufficiently massive and close to serve as the shepherd moon, the upper bounds placed on a possible Lagrange-point moon by Voyager ( $r \lesssim 6$  km; Smith et al. 1989), effectively eliminate this model as a viable contender, but only under the assumption that the spread in semimajor axes of arc particle orbits is equal to the observed width of the ring, 15 km. Also eliminated are variants of the same model in which the shepherding moon lies on a more distant but resonant orbit (Lin et al. 1987; Sicardy 1988, 1991).

To accommodate the nonexistence of a large Lagrange moon while still assuming that  $\Delta a = 15$  km, Sicardy and Lissauer (1992) modified the Lagrange-point model to include the effects of two small co-orbiting Lagrange moons instead of one large one, each librating about one of the other's triangular Lagrangian points. In this modified theory, arc particles are trapped between the two moons with particle trajectories being reversed in the frame rotating with the mean angular velocity of the moons during a relatively close encounter.

Two such moons as small as 5 km in radius could provide azimuthal confinement of a ring of radial width 15 km by reversing particle motions relative to the mean motion of the arcs. However, such reversals would require close approaches, leading to a complex and possibly chaotic dynamical interplay (Hénon and Petit 1986; Greenzweig and Lissauer 1990). Moreover, the two moons confining the arc region would at times be much closer than 60° from each other, and thus would be forced apart by 3-body gravitational effects. Under this scenario, it would have to be assumed that we are observing the system at a very special moment. Finally, one or two additional moons would be needed between each arc. Such a configuration seems to require an unreasonably large number of hypothesized satellites just below the Voyager detection limit (Sicardy and Lissauer 1992).

(d.) *Single Satellite Model.* Goldreich et al. (1986) developed an alternative model which also relies on corotation and Lindblad resonances, but arising from the *same* nearby satellite. In their model, the corotation resonances required are those involving the higher-order components of the gravitational potential of a moon on an inclined (CIR) or eccentric (CER) orbit. The corotation resonance perturbation potential is

$$\Phi_c = -i_m^2 A_c \cos \Psi_c \quad (27)$$

with coefficient

$$A_c = \frac{M_s}{M_P} n_s^2 a_s^2 V, \quad \text{for } m_c > 0 \quad (28)$$

where  $i_m$  is the mutual inclination of the orbits of the satellite and the ring,  $\Psi_c$  is the critical argument of corotation, and  $V = \beta^2 b_{3/2}^{(2m+1)}(\beta)/8$ , where  $b_{3/2}^{(2m+1)}$  is a Laplace coefficient (see, e.g., Brouwer and Clemence 1961), and  $\beta \equiv a/a_s$  (Goldreich et al. 1986). For  $m_c > 1$ , each corotation resonance of this type is situated very near a Lindblad resonance of the same satellite. The Lindblad resonance wavenumber  $m_L$  differs from the wavenumber  $m_c$  of the nearest corotation resonance by  $\pm 1$ . The Lindblad resonance perturbs the libration of particles around the corotation site by causing the orbit of the libration center to become elliptical, while providing the torque and energy required to stabilize the arc against collisional dissipation. Because a satellite's orbital eccentricity would be expected to damp tidally on a time scale much shorter than would its inclination, Goldreich et al. favored (and developed) the theory for arc maintenance via CIRs.

2. *Arc Kinematics and Orbit Geometry.* The Adams ring is one of a few narrow rings having longitudinally discrete features whose motion can be observed, measured and in principle used to determine the ring's orbital elements in the same way that positional measurements of a satellite may be used to arrive at its elements (Owen et al. 1991). Such measurements of the Adams ring arcs are easily accomplished in Voyager images in which a continuous sweep of orbital longitude is easily seen in a single image, allowing the selection of a particular "benchmark" location, e.g., the leading or trailing

edge of an arc, for measurement of longitude and radius. Calculation of the arcs' mean motion from positional measurements in the highest resolution Voyager imaging data spanning 6.5 days (Smith et al. 1989) yielded a value of  $n = 820.12^\circ \pm 0.06^\circ \text{day}^{-1}$ , precise enough to identify the arc responsible for the stellar occultation observed by the Voyager PPS/UVS experiments (Sec. II), but not precise enough to determine which of the arcs was responsible for the successful groundbased stellar occultation events observed 4 and 5 yr earlier. This circumstance precludes the unique assignment of any single groundbased occultation event to a particular Voyager arc, and renders impossible a direct calculation of arc mean motion from combined groundbased and Voyager data analysis.

This problem may be circumvented by searching through an array of mean motions for that value which, when used to precess all arc observations to a single epoch, has the greatest success in matching the positive, as well as negative, groundbased occultation results to the Voyager arc observations. This analysis was first performed by Nicholson et al. (1990) who concluded on the basis of such pattern-matching that the most likely value of arc mean motion is  $820.1185 \pm 0.0004^\circ \text{day}^{-1}$ . (The subsequent discovery of Courage, and the bifurcation of Egalité into two arcs, Egalité 1 and Egalité 2, does not alter this conclusion significantly.) A diagram first presented by Nicholson et al. illustrating this point, modified to include the full repertoire of groundbased observations in the vicinity of the Adams ring and to account for the discovery of two additional arcs, is reproduced in Fig. 20. The revised mean motion estimate of  $820.1194 \pm 0.0006^\circ \text{day}^{-1}$  is not statistically different from the earlier estimate. Although a second possible value for the mean motion of  $\sim 820.1118^\circ \text{day}^{-1}$  also fits the available observations (and changes the identification of the arcs observed in 1984 and 1985 from Liberté and Egalité to Egalité and Fraternité, respectively), the larger value is considered preferable on the basis of the consistency in equivalent widths  $E$  of the individual arcs detected in the 4 groundbased occultation events (Sec. II.B.4(c) and Fig. 4) and on the dynamical grounds presented in Sec. III.A.3. The semimajor axis of the arcs' orbit calculated from the preferred mean motion assuming no perturbations is 62,932.31 km; the smaller value corresponds to 62,932.69 km.

Horanyi and Porco (1993) have recently shown that short-period perturbations by Galatea on the arc particles' mean motion amount to  $0.0039^\circ \text{day}^{-1}$ , ten times larger than the uncertainty quoted by Nicholson et al. (1990). While this result suggests that the values given above correspond to an *effective* mean motion which includes the perturbations by nearby Galatea, and that the true semimajor axes are therefore larger by 0.20 km, theoretical resonance locations are subject to the same correction and there remains no net effect on the kinematical and dynamical models so far devised for the orbits of the Adams ring arcs (Porco 1991).

Despite the fact that groundbased observations in the 1980s were successful in detecting the Neptune ring arcs (Sec. II.B), the uncertainty in ascertaining both the center and spin pole direction of Neptune rendered these

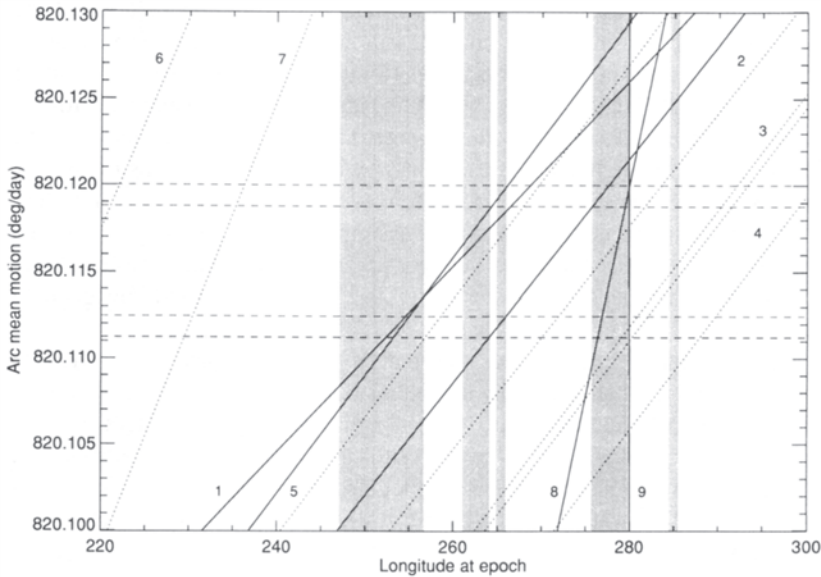


Figure 20. The longitudes of stellar occultation cuts across the Adams ring, precessed to the epoch August 18, 1989 (JD 244 7757.0), as a function of assumed arc motion. Solid lines indicate the positive arc detections shown in Figs. 10, and 15 (1 = July 22, 1984, 2 = June 7, 1985, 5 = August 20, 1985, 8 = July 9, 1988, and 9 = Voyager PPS/UVS), while dotted lines indicate observations for which no arc event was seen in the vicinity of the Adams ring. There is a  $10^\circ$  uncertainty in the longitude of the July 22, 1984 track (Sicardy et al. 1991). The gray bands indicate the locations of the five Voyager arcs, based on imaging measurements (Porco 1991; see also Table II). Horizontal dashed lines show two possible solutions for the mean motion which are consistent with positive and negative observations:  $820.1194^\circ \pm 0.0006^\circ$  and  $820.1118^\circ \pm 0.0006^\circ \text{day}^{-1}$ . The former is the preferred value (figure from Nicholson et al. 1995, updated from Nicholson et al. 1990).

detections inadequate in providing more than a rough estimate of the arcs' radial position. Consequently, modeling of the kinematics and geometry of Neptune's arcs and other rings has relied so far on Voyager high resolution images, with the single Voyager occultation datum providing a valuable constraint in deriving the arc orbital elements. Porco (1991) acquired positional measurements (i.e., absolute radii and longitudes) across 18 of the highest resolution images of the arcs after errors in camera pointing were corrected using stars in the image for absolute reference. For the Voyager UVS occultation of  $\sigma$  Sgr by the Liberté arc (Fig. 15b), an optical-depth-weighted radial average across this profile was used as the center radius. The longitude system used for these measurements is Neptune-centered with its origin taken to be the ascending node of the Neptune equator as determined by Jacobson et al. (1991) on the Earth mean equator of 1950 (EME50) at the time of Voyager Neptune encounter.

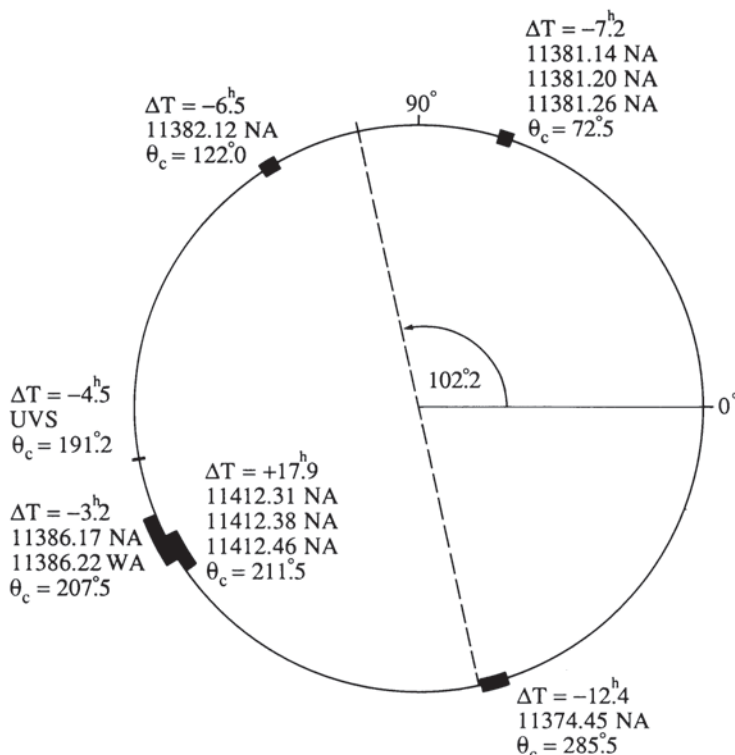


Figure 21. The longitudinal distribution of Voyager 2 high resolution observations of the arcs (including the PPS/UVS observation) in an inertial system centered on Neptune with the zero point defined by the ascending node of Neptune's equator plane (Jacobson et al. 1991) on the Earth Mean Equator of 1950. The indicated longitudes are the locations of the arcs at the time of observation. Two sets of images, one taken 3.2 hr before Voyager 2 closest approach to Neptune and another taken 17.9 hr after closest approach, coincidentally fall at nearly identical longitudes.

Figure 21 shows the distribution of the Voyager data in the inertial Jacobson et al. (1991) longitude system used to model the arcs' orbit, as well as the position of the nodal line of the orbit on the Jacobson equator. Though sparse in number, the data are fairly well distributed around  $360^\circ$ , resulting ultimately in a set of solution parameters with acceptably low correlations and uncertainties.

Using the observed arc mean motion derived by Nicholson et al. (1990), which differs by only  $0.0009^\circ\text{day}^{-1}$  from the most recent value of Nicholson et al. (1995), Porco (1991) determined that the mean semimajor axis of the arcs falls within 0.11 km of the 42:43 ( $m_c = 43$ ) corotation inclination resonance (CIR) of Galatea. This value is less than the uncertainty in the position of the resonance and less than its width (see Sec. III.A.3.). The uncertainty in the arc semimajor axis is <1% of the 23 km separation between consecutive

corotation resonances, so this spatial coincidence is unlikely to be merely a chance occurrence. Furthermore, Galatea's 42:43 ( $m_L = 42$ ) outer Lindblad resonance (OLR) lies  $1.47 \pm 0.13$  km interior to the ring's semimajor axis.

Motivated by the expectation that Galatea would be perturbing the arcs via its Lindblad resonance, Porco successfully fitted a model describing a resonantly forced radial disturbance of azimuthal wavenumber of  $m_L = 42$  rotating through the Adams ring at the expected pattern speed (i.e., Galatea's mean motion,  $n_s = 839.6598^\circ \text{day}^{-1}$ ) to all reliable radius-longitude measurements on the arcs derived from the imaging and Voyager occultation data. Models of this type have been successful in explaining Saturn's outer A and B ring edges (Porco et al. 1984b) and its Huygens ring (Turtle et al. 1991). The model incorporated the effects of inclination to account for the possibility that the Adams ring might be inclined to the Neptune equator plane determined by Jacobson et al. (1991). The parameters of the model which describes the configuration of the Adams ring at epoch August 18, 1989 at 12:00 ET are: radial amplitude,  $ae = 29.6 \pm 1.5$  km (or forced eccentricity,  $e = 0.00047 \pm 0.00002$ ); longitude of radial minimum,  $\theta_0(\text{min}) = 50.82^\circ \pm 0.10^\circ$ ; inclination,  $i_0 = 0.0617^\circ \pm 0.0043^\circ$ ; and longitude of the ascending node,  $\Omega_0 = 102.2^\circ \pm 1.0^\circ$ . [A model including an  $m = 1$  normal mode instead of inclination gave significantly poorer residuals, indicating that the deviations of mean radius observed in all images from a constant value are undoubtedly due to an inclination relative to the Jacobson equator and not due eccentricity.] The resulting mutual inclination between Galatea and the Adams ring is  $i_m = 0.02^\circ \pm 0.01^\circ$ .

Three parameters were held fixed to obtain this solution: the semimajor axis of the ring, the pattern speed, and the nodal regression rate. The semimajor axis inferred from the arcs' mean motion,  $a = 62,932.37$  km, was used to fix  $a$ . (With  $a$  allowed to vary, the fitted value of  $a$  was coincident with the inferred value to within the standard error in the solution, giving confidence that the inferred value is indeed the correct one.) The pattern speed was held fixed at the mean motion of Galatea:  $\Omega_{\text{pat}}^L = n_s = 839.6598^\circ \text{day}^{-1}$  (Owen et al. 1991). The regression rate expected for an orbit inclined to the Neptune equator plane at the semimajor axis of the Adams ring due to Neptune's oblateness alone is  $\dot{\Omega} = -0.676^\circ \text{day}^{-1}$ . However, if the Adams ring is actually lying within its Laplace plane and its inclination is instead a reflection of a necessary revision in Neptune's spin axis direction, then the ring will have a negligible nodal regression rate given by orbit precession rate of Triton,  $0.52^\circ \text{yr}^{-1}$ . In the expectation that the latter would be the case, the nodal regression rate was fixed at zero. (A solution found setting  $\dot{\Omega} = -0.676^\circ \text{day}^{-1}$  was essentially the same as that given above with the exception that the nodal line at epoch was found to be  $106.5 \pm 1^\circ$ .)

Figure 22 displays the arc kinematic model fitted to 3 images of the Fraternité arc at  $-7.2$  hr from closest approach from a range of  $\sim 4.3 \times 10^5$  km. The ring radial scale is  $\sim 6.5$  km pixel $^{-1}$ . The longitudes of the data points have been rotated back to epoch using the solution pattern speed, i.e., Galatea's

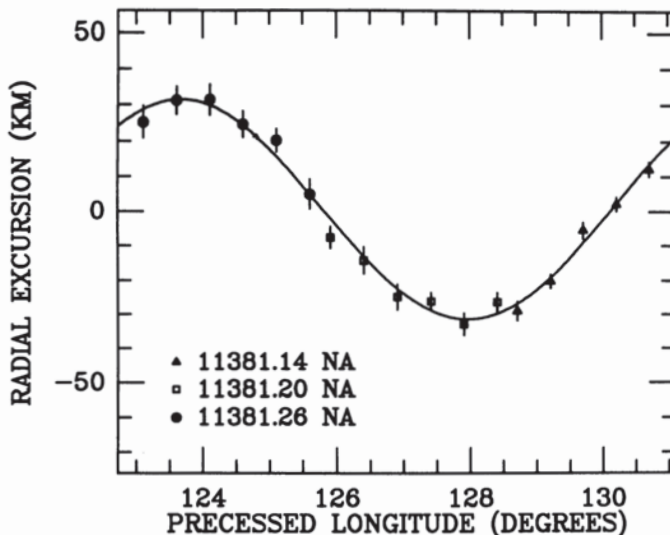


Figure 22. Radial excursion vs longitude of the Fraternité arc from three narrow angle Voyager images taken 7.2 hr before Voyager's closest approach to Neptune. All data points have been precessed back to a common epoch using a pattern speed equal to Galatea's mean motion,  $\Omega_{\text{pat}}^L = n_s = 839.6598^\circ \text{day}^{-1}$ . The solid line indicates a portion of the  $m_L = 42$  pattern which best fits the data.

mean motion. The error associated with this precession is  $<0.02^\circ$ . Radial excursion is given relative to the mean projected radius for that set of frames. A radial distortion of amplitude  $ae = 29.6$  km and azimuthal wavelength of  $360/m^{-1} = 8.57143^\circ$  is clearly seen.

All high-resolution images of the arcs show this traveling distortion, and there is no definitive evidence at present that this distortion is seen traveling through any part of the Adams ring other than the limited longitudinal range containing the arcs. Despite this fact, it can be shown that the distortion is not an eccentricity wake (Sec. III.A.1). Assuming it is a wake excited by Galatea and taking  $ae = 29.6$  km, one can calculate the required mass ratio of Galatea from Eq. 23 to be  $M_s/M_p = 5.04 \times 10^{-8}$  or  $M_s = (5.17 \pm 0.2) \times 10^{21}$  g. This value implies an unreasonably large mass density unless the volume of Galatea is near the upper bound estimated from Voyager images (Thomas and Veverka 1991). Moreover, with this mass the criterion for damping of particle eccentricity between successive encounters with the satellite,  $\frac{1}{m_L^4} \frac{M_p}{M_s} \lesssim 1$ , is violated. (The same violation occurs if Eq. (22) is used instead to derive  $M_s$ .) This can be seen by inspection in Porco (1991, Fig. 2): the regularity of the pattern observed as far away as  $300^\circ$  from Galatea's last passage would not be expected if substantial damping occurred within one synodic period. On these grounds, the traveling distortion is apparently not an eccentricity wake but a resonant perturbation.

Corroborating this result is the observation that the phasing of Galatea

relative to the distortion is that expected for a resonant perturbation. Galatea's longitude at epoch in the Jacobson reference system is calculated to be  $\theta_s = 46.64 \pm 0.01^\circ$  (Porco 1991). At epoch, one of the 42 radial minima of the pattern falls at  $\theta_0(\text{min}) = 50.82 \pm 0.1^\circ$ . For orbits exterior to Galatea's 42:43 OLR, the Lindblad resonance critical argument  $\Psi_L = (m_L + 1)\theta - m_L\theta_s - \tilde{\omega} = \pi$ . Consequently, a ring particle reaches conjunction with the satellite,  $\theta = \theta_s$ , when  $\theta = \tilde{\omega} + \Psi_L = \tilde{\omega} + \pi$ , i.e., when the particle reaches apoapse. Porco (1991) found that, at epoch, the expected position of the satellite relative to the fitted longitude of radial minimum  $\theta_0(\text{min})$  is  $\theta_s = \theta_0(\text{min}) - \Psi_L/m_L = 50.82 - \pi/42 = 46.53 \pm 0.10^\circ$ , identical within uncertainties to  $\theta_s$  determined by Owen et al. (1991). [See Eqs. (29) and (31) of Porco and Nicholson (1987).] The orientation of the  $m_L = 42$  pattern with respect to the satellite's location is that anticipated for radial perturbation by Galatea's 42:43 outer Lindblad resonance if all the particle orbits fall exterior to this resonance. (The significance of the fact that the difference between the arc's semimajor axis and the Lindblad resonance,  $\sim 1.5$  km, is much less than the arcs' radial width is discussed in Sec. III.A.3.) A purely resonantly forced perturbation of  $ae = 29.6$  km yields (from Eq. 22) a mass ratio for Galatea of  $M_s/M_P = (2.07 \pm 0.20) \times 10^{-8}$ , or  $M_s = (2.12 \pm 0.21) \times 10^{21}$  g. Combining this value with measurements of Galatea's size (Thomas and Veverka 1991) yields a reasonable mass density for a Neptune satellite of  $1.0 \pm 0.5$  g cm<sup>-3</sup>.

Though a kinematic model derived from a combined analysis of the groundbased and Voyager data on the arcs is not yet in hand, it is illuminating to compare the groundbased observations against the Porco (1991) arc model. Excepting the quite uncertain radius for the July 22, 1984 event, the observed radii for the Adams ring arc occultations range from 62,904 km to 63,204 km, when reduced using the pole of Porco (1991). The ring's calculated semimajor axis is 62,932 km. Taking into account the  $\pm 30$  km amplitude radial distortion, only the July 9, 1988 event falls definitely outside the radial range expected for the Adams ring. Assuming a slightly revised pattern speed of  $839.6622^\circ\text{day}^{-1}$ , calculated on the assumption that the Adams ring lies *exactly* at Galatea's 42:43 corotation resonance [the measured value of  $n_s = 839.6598 \pm 0.0025^\circ\text{day}^{-1}$  is too uncertain to permit extrapolation over five years], Nicholson et al. (1995) find radius residuals for the occultation data relative to the Porco model of  $+41 \pm 27$  km (June 7, 1985),  $+55 \pm 53$  km (August 20, 1985),  $+275 \pm 28$  km (July 9, 1988), and  $0 \pm 5$  km (PPS). The residual for the July 1988 datum is too large to be attributed either to plausible errors in reconstructing the occultation geometry or to residual uncertainty in the ring pole, and is also incompatible with a simple precessing ellipse model (Nicholson et al. 1995). Some doubt therefore exists as to the reality of this particular arc detection. The other three points seem to be in satisfactory agreement with the Porco model.

A comprehensive kinematic model of the arcs incorporating both Voyager and Earth-based data may make it possible to further constrain the ring pole and/or the resonant pattern speed. Unfortunately, the intrinsic accuracy with

which the Earth-based occultation geometry can be reconstructed is limited by the fits to atmospheric ingress and egress times, which lead to geometric uncertainties of about a half of an atmospheric scale height, or  $\sim 25$  km. Unlike the situation at Uranus, for which the uncertainties in occultation-derived ring radii are  $\sim 1$  km (French et al. 1988), Neptune provides no convenient reference frame in the form of readily detected nearly circular rings.

*3. Successful Arc Dynamical Models.* Porco (1991) presented the proximity of Galatea's resonances to the arcs, the resonantly forced  $m = 42$  traveling distortion, the mutual inclination between Galatea and the orbit of the arcs, and the following arguments as support for a single-satellite arc confinement model similar to that proposed by Goldreich et al. (1986). (Subsequent detailed numerical studies by Foryta [1993] and Horanyi and Porco [1993] also support the single satellite confinement model.)

The single satellite corotation model predicts an exact phasing of the corotation sites relative to Galatea's position and the angular location of the relative line of nodes, but the very small mutual inclination results in an uncertainty in the nodal line position large enough to prevent this prediction from being tested at present. However, it also predicts a particular azimuthal size and spacing of corotation sites: i.e., if the arcs fall within the corotation zones of Galatea's 42:43 CIR, then their angular extents should each be no greater than  $360/2m_c = 4.1860^\circ$ , and their angular spacings should be close to integer multiples of this value. The angular extents of Courage, Liberté, Egalité 1, and Egalité 2 (third column in Table II) all meet this criterion to varying degrees. Only the angular extent of Fraternité,  $9.6^\circ$ , which is between twice and three times this value, poses problems for this model (Sec. III.A.4). The observed arc separations (column 4 of Table II) are not exact integer multiples of  $4.1860^\circ$ , but this may be accounted for by the possibility of slow libration (with a period of  $\sim 10$  yr) around the corotation site by a few relatively large bodies within the arcs which act as the source of dust (Smith et al. 1989; Porco 1991). Consequently, while the phase of the arc-Galatea corotational shepherding relationship cannot be adequately verified, Porco (1991) claimed that the azimuthal spacing and angular extents of the arcs roughly agree with those predicted by the single-satellite model.

For a corotation resonance, small stable librations of the orbit guiding center around the potential maxima take the form of an ellipse, and the resonance radial width—the maximum spread in semimajor axes of librating particles—may be identified with the minor axis of the ellipse (Goldreich et al. 1986). However, the inference that the arc particles are longitudinally filling their corotation zones implies *large* amplitude librations. For particles whose semimajor axes librate over the maximum possible range, the libration path deviates from an elliptical shape. In this case, the resonance width is

given by (Sicardy 1991):

$$\Delta a \sim \frac{8}{\sqrt{3}} \frac{i_m}{n} \sqrt{A_c} \quad (29)$$

where, for the 42:43 CIR,

$$A_c \approx 0.085 m_c^2 \frac{M_s}{M_p} (na)^2. \quad (30)$$

Using the upper bound on the mutual inclination ( $0.03^\circ$ ) and a value for Galatea's mass derived from the amplitude of its presumed Lindblad perturbation of the arcs,  $M_s = (2.12 \pm 0.21) \times 10^{21}$  g, Eqs. (29) and (30) yield a resonance width of  $\Delta a \sim 0.4$  km. [Porco (1991) derived a value of 0.6 km assuming an elliptical shape for large amplitude librations.] It is worth noting that the very close proximity of Galatea's Lindblad and corotation resonances is likely to lead to a coupling between the two that cannot be considered analytically. However, numerical integrations which mimic the Galatea-arc geometry necessarily show the resulting effects of any coupling. Integrations of this type performed by Horanyi and Porco (1993) indicate that arc particles will cease to be confined to a corotation site if their spread in semimajor axes is  $\gtrsim 0.4$  km. Any coupling between the two resonant perturbations is obviously insufficient to alter significantly the result that the spread in particle semimajor axes is much less than the observed 15 km radial width of the arcs.

The rather small  $\Delta a$  carries two important ramifications. First, the orbits of all corotationally confined arc particles, regardless of their position in the libration cycle, fall exterior to Galatea's Lindblad resonance. This configuration is consistent with the observed coherent radial distortion seen traveling through the arcs; if this were not the case and instead  $\Delta a \gtrsim 2$  km, then particles with  $a < a_{OLR}$  would have a phase differing by  $180^\circ$  from those with  $a > a_{OLR}$  and a coherent 30 km amplitude distortion would not be observed. (Though the action of self-gravity among ring particles within other rings, such as Saturn's narrow Colombo ring or the outer edge of Saturn's B ring, can modify the phasing and amplitude of the distortions anticipated from satellite resonant effects alone, self-gravity is unlikely to be important in the Neptune ring arcs where both the particle size and the optical depth, and hence surface mass density, are relatively small.)

Second, a variation in  $\Delta a \sim 0.4$  km across the corotation zone maps into a fractional variation in distance from the Lindblad resonance,  $\Delta(a - a_{res})/(a - a_{res})$ , and a fractional variation in forced amplitude (Eq. 22), of  $\Delta(ae)/ae = -\Delta a/(a - a_{res}) \sim 0.4/1.5 \sim 0.3$ , or an absolute radial width of up to  $W \sim 0.3ae \sim 9$  km. That is, the arcs have a radial width in the Porco (1991) model determined by a spread in forced orbital eccentricity, not in semimajor axis—a possibility noted independently by Sicardy and Lissauer (1992). This is the major point of departure from the single satellite model

of Goldreich et al. (1986) in which the arc widths were set by  $\Delta a$ , placing (through Eqs. 29 and 30) a strong constraint on the product  $M_s i_m^2$ .

In summary, the coherent phasing of the radial distortion fixed in Galatea's reference frame requires that  $\Delta a \lesssim 1$  km. The combined action of Galatea's 42:43 CIR and 42:43 OLR can bring about this set of circumstances as well as explain the observed radial widths, provided that the arc particles are spread over the maximum stable range in semimajor axis (which is expected, as the length of the arcs is near that of the maximum stability zone) and that the arcs have been radially resolved near their greatest radial width. Further modifications to this model are discussed in Sec. III.A.5.

The behavior and detailed morphology of the arcs as suggested by this single-satellite corotation model are illustrated in Fig. 23. In particular, the particle orbits are confocal and nested, with a negative eccentricity gradient, resulting in orbit crossing at quadrature and a radial width which can vary from a minimum value equal to the spread in particle semimajor axis ( $\sim 0.4$  km) near quadrature to a maximum of  $\sim 9$  km.

#### *4. Outstanding Problems with the Single Satellite Model.*

(a) The single satellite model requires a nonzero inclination between the orbits of the satellite and arcs. The mutual inclination derived from modeling of the arcs' orbital elements,  $i_m = 0.02^\circ \pm 0.01^\circ$ , is statistically consistent with zero. If  $i_m$  were identically zero, corotation-inclination shepherding by Galatea would be impossible, and azimuthal confinement of the arcs would have to arise from a different mechanism. Moreover, the observed width of the arcs can only be matched if the mutual inclination of the ring and Galatea is near the upper limit, and if all observations of the width of the arcs occurred near the phase at which the spread in semimajor axes was the greatest. The addition of groundbased data into the arc kinematical/geometric models should help confirm or refute the presence of a mutual inclination between arc and satellite orbits.

(b) The negative eccentricity gradient across the arcs results in relatively high-velocity collisions, a few  $m s^{-1}$ , between ring particles. Though it is unlikely that such collisions are energetic enough to destroy ring particles (Davis and Ryan 1990), and though they are apparently necessary to explain the large abundance of dust in the arcs, they are also capable of altering the orbital elements of the particles and perhaps removing them from resonance completely. It is still unclear how particles can suffer such orbit-altering collisions while obviously maintaining their orbital phases long enough ( $\sim 1$  yr; Porco 1991) to participate in the Lindblad perturbation of Galatea on the arcs.

(c) Related to problem (b) is the observation that the Fraternité arc subtends two and possibly three corotation sites. The particles which fall midway between corotation sites in this arc find themselves where the corotation potential is the weakest and are not confined by the CIR, yet they too are participating in the Lindblad distortion. This observation is made even more surprising by the fact that the surface area of the arcs is dominated by dust which undoubtedly has a very short arc residence lifetime, probably very much

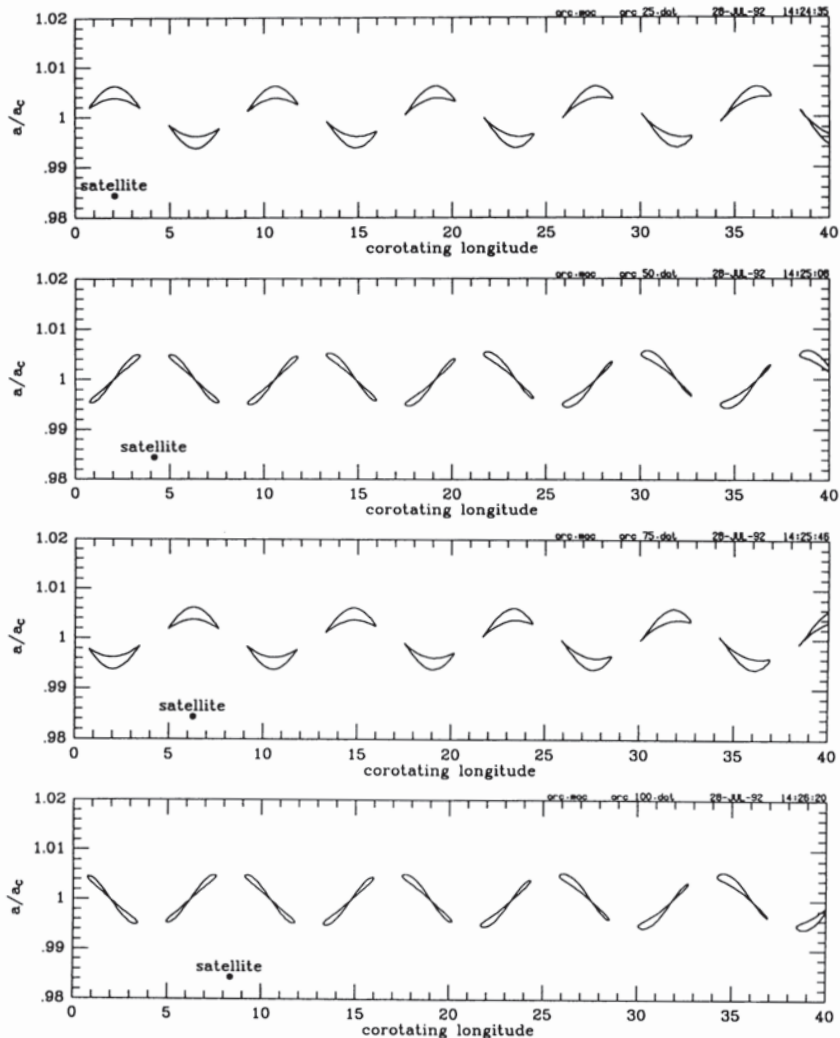


Figure 23. An illustration of the arc kinematics implied by the corotation resonance model of Porco (1991). Individual stable corotation sites, separated by  $360^\circ/2m_c = 4.186^\circ$  ( $m_c = 43$ ), are outlined by the crescent-shaped curves, each of which traces the motion of a typical arc particle over one complete libration cycle. Successive panels show the same  $40^\circ$  segment of the ring, at intervals of  $1/4$  of the orbital period of the perturbing satellite, Galatea, in a reference frame which corotates with the ring particles' mean orbital motion. The location of the satellite is indicated at each time step, advancing at an angular frequency relative to the arcs of  $n_s - n = (n_s - \dot{\Omega}_s)/m_c = 19.5434^\circ\text{day}^{-1}$  or  $8.3791^\circ$  during one complete satellite orbital period. (See text for details.) During this same period, the particles in each arc execute approximately one Keplerian orbit, and therefore one radial oscillation in the corotating frame. The radial displacement of the arcs from their mean semimajor axis is due to the influence of the nearby  $m_l = 42$  outer Lindblad resonance with Galatea, which produces an  $m_l$ -lobed distortion with an azimuthal wavelength of  $360^\circ/m_l = 8.571^\circ$  rotating at the angular velocity of the satellite,  $n_s$ . In the frame corotating with the arcs, this distortion travels through the ring at Galatea's synodic mean motion,  $n_{\text{syn}}$ , causing the arcs to oscillate radially,

less than 1 yr. Possible solutions to this problem are discussed in Sec. III.A.5.

(d) No explanation is given for why the occupied corotation sites are all clustered close together, though Porco (1991) suggested, and Esposito and Colwell (1992; see also Sec. IV.B) numerically showed that the breakup of a single small satellite and the subsequent capture of some of the debris into a few of Galatea's CIR zones, might have resulted in the present configuration of arcs (cf., Foryta 1993).

(e) The large torques exerted on the Adams ring by Galatea predict rapid outward orbital migration of the ring. The perturbations exerted upon ring particles orbiting near Galatea's 42:43 OLR result in a secular transfer of angular momentum from the moon to the ring. The strength of the torque is difficult to estimate, as the width of the ring is very narrow compared with the resonance coupling region, and the efficiency (even the sign) of the angular momentum transport varies substantially within this zone (Shu et al. 1985). Azimuthal density variations would make precise calculations even more complicated. However, a crude order of magnitude estimate can be made using the standard torque formula of Goldreich and Tremaine (1979):

$$\Gamma \approx 0.4a^2n^2 \left( \frac{M_s}{M_p} \right)^2 \left( \frac{a}{a - a_s} \right)^4 M_r \quad (31)$$

where  $M_r$  is the mass of the Adams ring. If a steady state is reached, the corresponding drift in semimajor axis of the ring is:

$$\frac{\dot{a}}{a} \approx n \left( \frac{M_s}{M_p} \right)^2 \left( \frac{a}{a - a_s} \right)^4. \quad (32)$$

The numerical values given above (with  $M_s = 2.12 \times 10^{21}$  g) then yield  $\dot{a} \approx 2.4$  km yr<sup>-1</sup>. This value is too high by many orders of magnitude for the Adams ring to be stable over geological times.

In reality, the standard torque formula may not apply, even in an order of magnitude sense, due to the narrowness of the Adams ring. The derivation of Eq. (31) assumes overlapping of Lindblad resonances within the ring, a condition which is not satisfied within the Adams ring. However, any process

---

much as a water wave traveling under a boat at anchor causes the boat to rise and fall. As postulated by Porco (1991), the maximum radial width of the arcs is determined not by the semimajor axis spread of the arc particle orbits,  $\Delta a$ , associated with their corotational libration, but by the (negative) gradient in eccentricity forced by the Lindblad resonance,  $\Delta e$ . Because the absolute value of the eccentricity gradient exceeds unity, the libration streamlines cross at certain phases of the radial distortion, as seen in the second and fourth panels. For reasons of clarity, both the widths and radial displacement of the arcs in this figure have been exaggerated by a factor of 10 over their observed values: the model parameters for the figure are  $\Delta a/a = 3 \times 10^{-5}$ ;  $e_0 = 5 \times 10^{-3}$ ;  $q = \frac{a \Delta e}{\Delta a} = -40$ ; and corotational and Lindblad libration amplitudes  $D_c = 2.0$  radians and  $D_L = -0.2$  radians (Goldreich et al. 1986).

which randomizes or damps particle eccentricities between satellite encounters produces the same torque, giving the formula a rather wide range of applicability. The large abundance of small particles with (presumably) very short lifetimes in the arcs is consistent with the inference of high-velocity particle collisions resulting from the crossing of orbits. Energy transported along with angular momentum from Galatea could provide the necessary excitation of these velocities. Thus, while it is quite possible that the narrowness of the arcs affects the torque exerted upon the ring, we suspect that the reduction (if this indeed is the sign of the effect) is not large enough to solve the short time scale problem posed by Eq. (32).

*5. Possible Prospects and Modifications.* There are several possible solutions to the dilemmas mentioned above. The inference of a very small spread in arc particle semimajor axes re-opens the possibility that a *single* Trojan point satellite less massive than originally predicted by Lissauer (1985) might be responsible for, or assisting in, the confinement of the arcs. By comparing the perturbation potential of Galatea's CIR (Eq. 27) with that due to a Lagrange moon,  $\Phi_L = f(\theta)a_L^2n_L^2(M_L/M_P)$ , one sees that a satellite on an inclined orbit is roughly equivalent to a Lagrange moon of mass

$$M_L \approx i_m^2 V M_s. \quad (33)$$

For our purpose, it is enough to note that  $V \approx 0.085 m^2$  for  $m$  large. Thus, a Lagrange moon of mass  $M_L \sim 9.1 \times 10^{16} g$ , or  $r \sim 3$  km, would have the same magnitude of potential perturbation on the arcs as does Galatea. Such a satellite would have escaped detection by the Voyager cameras. If such a moon shared the orbit of the arcs, it could help to resolve some of the problems with the Porco (1991) model. Although the mass of such a moonlet would be too small for it to confine an arc whose particles have a spread in semimajor axis  $\Delta a = 15$  km in libration around the unseen moonlet's  $L_4$  or  $L_5$  point, it could confine an arc with the same angular extent but much smaller  $\Delta a \sim 1$  km (Sicardy and Lissauer 1992). The combined effects of the 1:1 corotation potential of such a moonlet and the 42:43 CIR of Galatea could confine a ring with a slightly larger  $\Delta a$  than either could alone. Moreover, the combined effects of the two moons could explain the morphology of the arcs; the additional potential of the Lagrange moonlet would provide a natural explanation for the arcs being concentrated in one region in azimuth (either 60° ahead of or 60° behind the moonlet), and for the existence of an arc which extends over possibly 3 libration centers of Galatea's 42:43 CIR. Galatea's 42:43 CIR would explain why the arc region is choppy, rather than the smooth tadpole shape of libration around one of the moonlet's Trojan points proposed by Lissauer (1985). Additionally, the presence of such a moonlet would slow the ring's rate of outward evolution due to torques from Galatea's 42:43 OLR by a factor equal to the ratio of the sum of the ring's mass and the moonlet's mass to that of the ring, a ratio which could be extremely large (Sicardy and Lissauer 1992).

Alternatively, if one assumes that the concentration of arcs within  $\sim 40^\circ$  is a result of the catastrophic disruption of a single satellite and the capture of debris into Galatea's CIR zones (Sec. IV), then small satellites need not be placed at the Lagrange points but instead within the arcs themselves. With a dynamical influence comparable to that of Galatea's 42:43 CIR, small embedded satellites might account for the extension of material across 2 or 3 corotation zones (as in the Fraternité arc). They may also be the source of the dust in the arcs and carry the densest part of the arc around with them as they librate over the course of 10 yr, explaining the observed positioning of the arcs. They have the added attraction of providing a natural way to slow the rapid drift of the arcs/ring away from Galatea. In fact, most of the mass of the ring may be composed of a fairly small number of large ring particles/small moons which are essentially collisionless, and thus are not subject to torques but act as an anchor for the ring. According to Poisson's theorem, secular torques between planetary bodies vanish to second order in the ratio of their masses to that of the primary; "standard" torques exerted on planetary rings are second order in the mass of the resonant moon and thus require interactions among the ring particles to dissipate or disperse the eccentricities excited by the moon. If the Adams ring contains exceptionally large particles or moons whose orbits are not affected by other ring material on time scales long compared to the synodic period of the ring and Galatea, these bodies will experience no (or a greatly reduced) torque from Galatea. The torque would thus be that given by the standard formula with the ring surface density equal to that in small, collisional particles. However, if the larger ring particles are coupled to the visible ring material on longer time scales, the ring would move outward as a whole at a rate reduced from the standard formula by the ratio of collisional mass in the ring to the total mass of the ring, including any embedded moonlets (cf., Sicardy and Lissauer 1992).

With regard to rapid rate of evolution, another force, e.g., gas drag, may act to remove energy and angular momentum from the orbits of the ring particles, providing a counterbalance to the torques from Galatea. A tenuous extended atmosphere is believed to exert substantial drag forces on dust within the Uranian ring system (Broadfoot et al. 1986). No evidence exists for a similar extended atmosphere of Neptune, but given the paucity of data currently available on the Neptunian system, the possibility that some drag force acts to counterbalance satellite torques cannot be completely excluded.

### B. Other Neptunian Rings

No kinematic or dynamical models have been published for the Le Verrier or Galle rings to date. Analysis of Voyager images taken when the rings were seen almost edge-on (Fig. 7) shows that the major rings are *not* exactly coplanar; Showalter and Cuzzi (1992b) concluded that while the planes of the Galle and Adams rings appear to be coincident, that of the Le Verrier ring is inclined by  $\sim 0.03^\circ$  to the other two rings. This unexpected result strongly suggests that both Adams and Galle lie in or close to their respective Laplace

planes (see Sec. II.A.7), while the Le Verrier ring does not. Further analysis of the Voyager images, and of the limited occultation data available for the Le Verrier ring, may shed further light on this matter.

The mean radius of the Le Verrier ring obtained from the Voyager images is  $53,200 \pm 20$  km (Smith et al. 1989; Porco et al. 1992; Porco et al. 1995; Showalter and Cuzzi 1995), or  $\sim 75$  km greater than the radius obtained from the putative PPS observation of this ring and  $145 \pm 35$  km greater than that of the tentatively identified feature in the August 20, 1985 occultation (see Table V and Fig. 16). [These values are based on the instantaneous ring pole determined by Showalter and Cuzzi (1992b) and the Jacobson precession model for Neptune's equator plane.] These radial discrepancies seem to be significant, but too few data are presently available for this ring to permit an assessment as to whether they are due to a nonzero eccentricity, to an error in the adopted ring pole, or to the low signal-to-noise ratio of the occultation data for this ring.

The mean radius of the Le Verrier ring is much less well known than is that of the Adams ring, which hampers any attempt at identifying a resonance with the nearby satellite. Its nominal radius is within 5 km of Despina's 52:53 outer Lindblad resonance (OLR) at 53,195.9 km, but the spacing between adjacent resonances is only 13.1 km, less than the uncertainty in the ring's radius and much less than the reported ring width of  $\sim 110$  km. There is at present no observational evidence of resonant perturbations in the Le Verrier ring.

### C. Electromagnetic Processes

The Neptune ring system exhibits a relatively high abundance of high-inclination dust (Table III). Hamilton and Burns (1992) have indicated possible roles of both solar radiation pressure and electromagnetic perturbations in explaining this phenomenon. Grains may charge to a few times the energy of the local plasma (about 10 eV from Voyager observations; see, e.g., Grün et al. 1984). This amounts to a potential of 1 volt on a grain of radius  $1\text{ }\mu\text{m}$ . The ratio of electromagnetic to gravitational forces is then (Hamilton and Burns 1992):

$$F_E/F_G \sim 6 \times 10^{-5} \left( \frac{1\text{ }\mu\text{m}}{r} \right)^2. \quad (34)$$

However, at "Lorentz resonances" (Burns et al. 1985; Schaffer and Burns 1987, 1992), grain eccentricity and inclination can be strongly perturbed by coherent superpositioning of weak forces, much as in the case of the more familiar Lindblad, vertical, and corotational gravitational resonances (see, e.g., Franklin et al. [1984] and Shu [1984] for reviews). Schaffer and Burns (1992) show how overlapping Lorentz resonances can lead to chaotic behavior.

Two candidate processes for producing high inclination dust were noted by Hamilton et al. (1990) and Hamilton and Burns (1992). Dust grains with large orbital radii (possibly derived from Triton or Nereid) can have

their eccentricities strongly increased (to typically 0.9) by radiation pressure, diminishing their specific angular momentum  $H = GM_P a\sqrt{1 - e^2}$  to the point where even weak vertical forces may produce significant inclinations. Alternatively, grains drifting *towards* synchronous orbit ( $3.22 R_N$ ) from either direction can become trapped in Lorentz resonances and have their inclinations pumped to very high values. Analogous processes have been studied in the gravitational context by Weidenschilling and Davis (1985). For this to occur, plasma drag, which causes evolution *away from* corotation, cannot be the dominant drag mechanism. Hamilton and Burns (1992) also note that particles as large as the  $10 \mu\text{m}$  grains reported by the PWS team (Gurnett et al. 1991) have  $F_E/F_G$  roughly 2 orders of magnitude smaller than for  $1 \mu\text{m}$  grains (Eq. 34), and would be much harder to perturb into highly inclined or eccentric orbits. On the other hand, they also note that if the highly eccentric, solar-radiation-dominated scenario above applies, impact velocities onto the spacecraft will be much larger than assumed by Gurnett et al. (1991) and the inferred grain radius may be an overestimate.

Hamilton and Burns (1992) have pointed out that the two strongest Lorentz resonances in the Neptune system occur quite near to the Adams and Le Verrier rings. On the other hand, the narrow radial extent of these rings does not allow for much forcing of the grain eccentricities by Lorentz forces. Two possibilities exist to reconcile these facts. The plasma in the immediate vicinity of the rings may be depleted by the presence of the ring material itself, or Debye shielding may be sufficient in these rings (with optical depth  $\sim 10^{-2}$ ) to diminish the charge per grain from the simple optically thin case (Grün et al. 1984).

#### IV. ORIGIN AND EVOLUTION

Even before Voyager encountered Neptune in 1989, the study of Voyager observations of the Jovian, Saturnian and Uranian ring systems had raised questions concerning the apparent youth and possible recent origins of planetary rings. For example, processes such as viscous spreading of narrow rings, transfer of momentum to small shepherding moons (i.e., satellite torques), and drag on the ring particles from the planet's extended atmosphere are believed to give rise to short lifetimes for the Uranian rings. (See Esposito et al. 1991 for a review.) For Saturn's rings, satellite torques (Goldreich and Tremaine 1982; Borderies et al. 1989; Lissauer et al. 1984, 1985), micrometeorite erosion (Northrop and Connerney 1987) and darkening of the ring material by incorporation of meteoritic material (Doyle et al. 1989) have been considered and yield similarly short lifetimes. Cuzzi and Durisen (1990) show that the orbital evolution of even the macroscopic ring particles from momentum deposited by meteoritic impacts provides a time scale shorter than  $2 \times 10^8 \text{ yr}$  for the C ring of Saturn and the Uranus  $\alpha$  and  $\beta$  rings. For comparison, Colwell and Esposito (1990a) estimate the Uranus  $\epsilon$  ring lifetime due to micrometeorite erosion and loss of small charged grains is less than  $10^8 \text{ yr}$ .

Some of these processes are significant for Neptune's rings as well, though time scales are uncertain. For example, as discussed in Sec. III.A, unless there are bodies within the Adams ring which are big enough to absorb the torque of Galatea on the ring and/or a sufficiently distended Neptune atmosphere to counterbalance Galatea's ring torque, the rate of outward evolution of the Adams ring would double the Galatea-ring distance in only several hundred years. Also micrometeorite erosion of the ring particles undoubtedly provides some portion of the visible dust in the Neptune ring system (Smith et al. 1989) and this dust is eventually lost from the rings, primarily due to Poynting-Robertson drag (Sec. IV.C). If this loss mechanism is as effective at Neptune as it is believed to be at Saturn and Uranus, it implies a Neptune ring system lifetime much less than the age of the solar system.

Small moons also have short lifetimes against bombardment by comets. Smith et al. (1989) concluded that most of the small moons of Neptune discovered by Voyager were not primordial, but more likely fragments of larger bodies (see Sec. IV.A). Colwell and Esposito (1992) find short moon lifetimes, typically  $5 \times 10^8$  yr or less, and conclude that some of the observed moons outside the Roche limit are partly unconsolidated rubble piles.

The short lifetimes inferred for the rings we observe today provide a strong incentive to consider a model of continuing ring creation and dispersal/erosion. In particular, the Voyager discoveries of narrow, eccentric, braided and/or dusty rings, and of small moons orbiting close to the rings, led to the proposal of a ring life cycle originating from the destruction of small moons (Smith et al. 1982, 1986; Esposito 1986; Cuzzi and Esposito 1987; Esposito and Colwell 1989). While this hypothesis may not account for the creation of Saturn's present-day massive ring system (Lissauer et al. 1988; Dones 1991), it is an attractive option for explaining the rings of Uranus and Neptune. The Neptune ring system exhibits a number of characteristics, such as ring arcs, large dust content, and narrow rings, that reinforce the requirement for current ongoing processes, both to create and to constrain rings. The small moons within the ring region (Sec. II.A.7) are an integral part of these processes. We discuss below the combined evolution of small moons and rings, with an eye towards explaining the present-day Neptune ring system.

### A. Satellite Disruption

A detailed model of the history of the small satellites of Neptune has been developed by Colwell and Esposito (1992, 1993). Their stochastic simulations of the moons' collisional fragmentation confirm the conclusion of Smith et al. (1989) that these moons are not primordial. Colwell and Esposito's calculations include several improvements over Smith et al. First, instead of the simple impact speed for gravitational focusing given by

$$V_i = \sqrt{V_\infty^2 + \frac{2GM_p}{a}} \quad (35)$$

where  $V_\infty$  is the mean velocity of impactors from the Oort cloud outside the

gravitational sphere of influence of the planet, and  $a$  is the orbital semimajor axis of the target moon, they considered the entire range of impact speeds for an isotropic distribution of impactors in the Sun's frame. This distribution arises from the orbital motions of the moon and the planet, as well as the orbital distribution of the impactors. This spread can be quite large, as can be seen in Fig. 24.

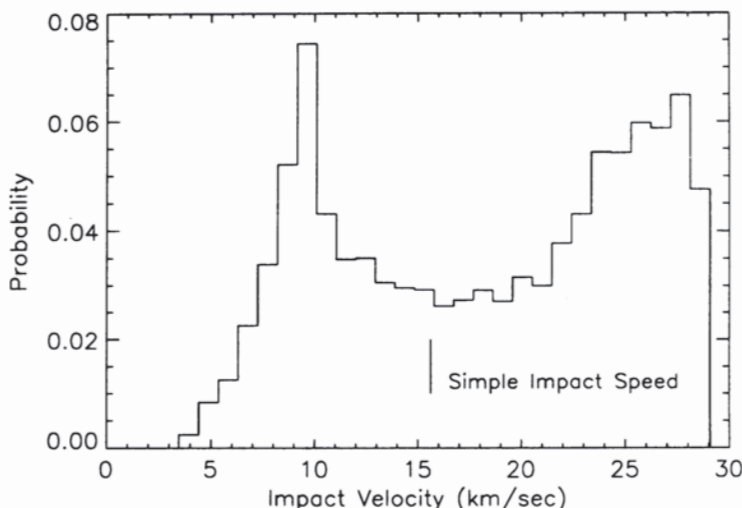


Figure 24. The distribution of impact speeds at an orbit radius of 73,600 km using zero obliquity for Neptune and assuming an isotropic distribution of impactors in the Sun's frame. Vertical line shows the impact speed  $V_i$  (figure from Colwell and Esposito 1992).

Because the threshold for catastrophic fragmentation is a function of the impact kinetic energy (i.e., the product of mass and velocity squared) and the impacting population of comets has a steep power-law distribution in mass, this velocity distribution imparts to a significant fraction of the more numerous smaller projectiles sufficient energy to disrupt a moon, a circumstance which can significantly increase the disruption rate. This is partly offset by the fact that some impactors have velocity lower than  $V_i$  calculated from Eq. (35). The net frequency of disruption almost doubles for a realistic velocity distribution.

For Uranus and Neptune, the expectation is that "planetary family" heliocentric impactors (i.e., associated in  $a, i, e$  with a particular planet), and not Oort cloud impactors, dominate the cratering and disruption rates (Smith et al. 1986, 1989). Like Smith et al., Colwell and Esposito extrapolate from the known population of Jupiter family comets to those in the Uranus and Neptune "families." However, an additional improvement made by Colwell and Esposito is a scaling of the orbits; the eccentricities are reduced by a factor that decreases, but does not entirely eliminate, the number of comets which intersect the orbits of Jupiter, Saturn or Uranus. This artificially accounts for

the more rapid loss expected for those comets in Jupiter-, Saturn- and Uranus-crossing orbits. Clearly, a major uncertainty is the exact flux of impactors at Neptune. Analysis of the cratering history on the Neptune satellites or pursuit of other means of determining the past or present fluxes could provide a secure starting point for simulations of the ring and moon histories.

Colwell and Esposito further modify the Smith et al. calculations by adopting the strain rate scaling model of catastrophic fragmentation presented by Housen and Holsapple (1990). Using this model, the probability of disruption of a small moon can be calculated as a function of size. Some examples are shown in Fig. 25.

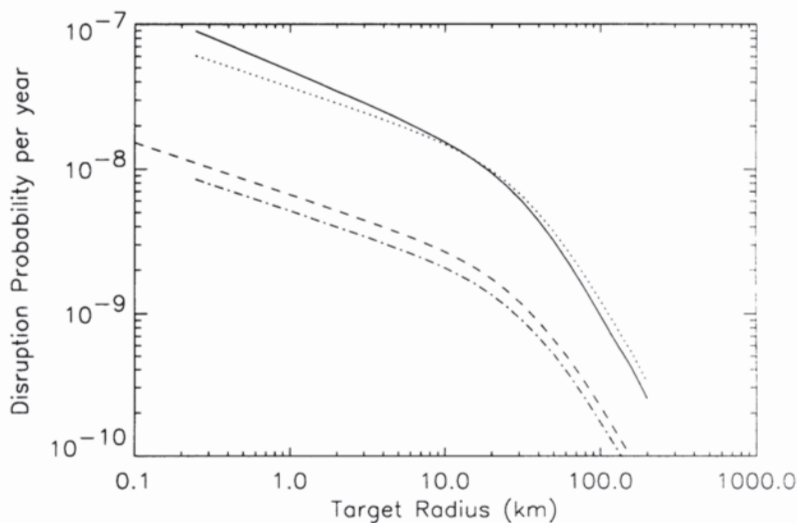


Figure 25. Disruption probabilities at Neptune for a moon orbiting at 73,600 km (orbit of Larissa). Lifetime is approximately the reciprocal of the probability. Top two curves: Neptune family comets extrapolated from Jupiter, solid line showing effect of reduced eccentricities (as discussed in text). Dashed lower curve: from Oort cloud comet distribution. Dot-dash curve: nominal flux with impact velocity,  $V_i$  (figure from Colwell and Esposito 1992).

Colwell and Esposito then follow the process of satellite disruption from an initial distribution through successive disruptions, ignoring re-accretion. Two approaches are used: a Monte Carlo simulation follows the history of only the largest fragment after each disruption; a Markov chain calculation follows the stochastic evolution of all the fragments.

Once a moon is destroyed, the “collisional cascade” to smaller size through successive disruptions occurs relatively quickly. Monte Carlo simulations of 300 separate histories give the results shown in Fig. 26. For an

original moon of radius 40 km, the solid line shows the mean, asterisks the median, and squares the mode for the distribution of largest surviving fragment as a function of time. These results show that the evolution of satellite populations from catastrophic fragmentation is more complex than can be described by a single "time scale" parameter. The speed of this cascade is dependent on the size distribution of the impactors, a poorly known factor. The difference between a slope of  $s = 2.5$  and  $s = 3.5$  in a differential size distribution described by  $n(r)dr \propto r^{-s}dr$  is quite significant. Better measurements of the size distribution are strongly desired.

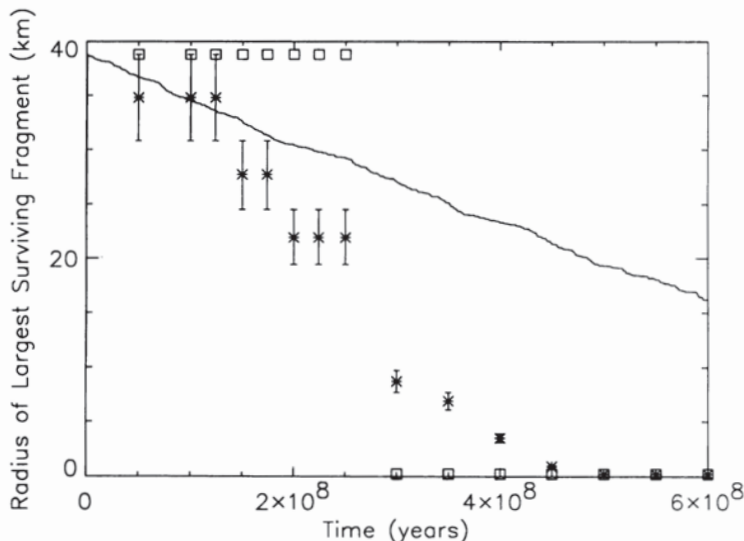


Figure 26. Mean (solid line), median (asterisks) and modal (squares) sizes of a distribution of 300 stochastic simulations of the collisional cascade for an initial 40 km radius moon, at the orbit of Thalassa. Error bars on the median connect the two size bins which fall on either side of the 50% cumulative probability (figure from Colwell and Esposito 1992).

The Markov chain formulation follows the evolution of the complete size distribution of moons and fragments. These simulations show that the more numerous smaller fragments can outlive the largest fragment followed in the Monte Carlo formulation. The collisional debris from an initial complement of satellites may be approximately described by a simple power law distribution. Colwell and Esposito find that after 4 Gyr, the collisionally evolved remnants of an original 100-km radius moon would include about  $10^3$  moons in the 1 to 10 km size range.

The question of the re-accretion of fragments of a disrupted satellite in or near the planet's Roche zone is an important one. Previous estimates of re-accretion time scales (Burns et al. 1984; Stevenson et al. 1986) are based on the calculation of Soter (1971), who computed the time scale for an ejected particle

an ejected particle to collide with its source body using a “particle-in-a-box” formalism. This method assumes that within a box in circular orbit about the planet, the relative motions of the particles, like the molecules of an ideal gas, are dominated by their random velocities. Canup and Esposito (1995) have used a matrix formulation of the integrodifferential equation describing the coagulation of disrupted satellite fragments, and an initial size distribution of Colwell and Esposito (1992). They considered velocity distribution evolution and tidal effects in improving on Soter’s (1971) calculation. Re-accretion probabilities calculated by Canup and Esposito as a function of time are shown in Fig. 27 for Neptune’s moons Galatea and Larissa. These probabilities indicate that outside the Roche limit re-accretion is likely within a few years, a result similar to that found by Soter (1971) despite the difference in assumptions. Obviously re-accretion is not a negligible process beyond the Roche limit, and realistic calculations incorporating re-accretion will be necessary for a thorough understanding of the evolution of satellites in this region.

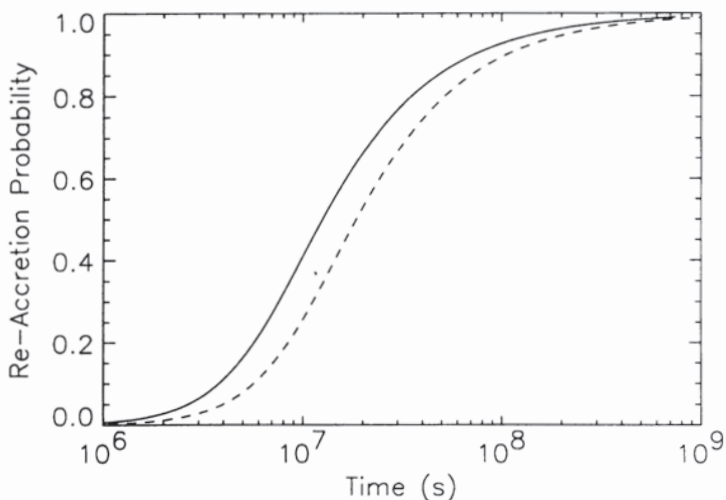


Figure 27. Probability of re-accretion of two Neptunian satellites, following disruption by a comet impact. Solid: Larissa; dashed: Galatea (figure from Canup and Esposito 1995).

However, near and within the Roche limit, the planetary tidal forces complicate the accretion process; the largest fragments do not re-accrete, although they can sweep up smaller debris. (The mere existence of planetary rings shows that accretion does not dominate near the planet.) Consequently, the neglect of accretion in present-day models of ring evolution (like that of Colwell and Esposito) is justified by the detailed simulations of Canup and Esposito (1995).

The calculations of Colwell and Esposito show that the small satellites of Neptune are likely to have evolved through catastrophic fragmentation since the end of the satellite and planet formation epoch 4 Gyr ago. The production of the currently observed smaller satellites is a natural consequence of the successive break up of larger satellites.

### B. Ring Formation

The formation of a narrow ring of material from a population of collisional fragments having initially a limited azimuthal extent and a small, but nonzero spread in semimajor axes is a natural consequence of Kepler shear. The evolution in size and velocity distribution of the fragments resulting from a satellite disruption were studied further by Colwell and Esposito (1993). They found that narrow ring formation occurs after a few hundred orbits and that a small number of large fragments remain. These are the largest members of the power-law size distribution describing the disruption fragments. Colwell and Esposito (1992) argue that these larger fragments will clear gaps (see also, e.g., Hénon 1981; Lissauer et al. 1981; Porco et al. 1984a). The discovery of Pan in Saturn's Encke Gap (Showalter 1991) may provide one example of this. As the ring undergoes viscous spreading in radius, its edges will approach the resonances with larger bodies in the system, allowing the edges to be shepherded and sharpened, as the edges of the Uranian  $\epsilon$  ring are shepherded by the moons Cordelia and Ophelia. The moons' radial evolution will then be coupled with that of the rings (although the common rate of spreading will be slower, because of the moons' larger mass). It is possible that their evolving orbits will move the ring moons into resonance with yet larger satellites. The "Cordelia Connection" suggested by Murray and Thompson (1990) for the Uranus rings may be an example of this; i.e., several of the unseen moons required to halt the radial spreading of the Uranian rings are extremely close to resonances with Cordelia, and Cordelia itself is very close to a resonance with Rosalind. This linking-up due to orbital resonances and associated transfer of angular momentum slows the initially rapid viscous spreading of a newly formed ring.

The moons can also confine the ring material in azimuth; Neptune's arcs provide a vivid example. Like the radial lock-up, this confinement occurs quite quickly; otherwise, differential rotation due to Kepler shear would smear out the arcs on a time scale of years. As discussed in Sec. III.A, Porco (1991) has shown how the azimuthal structure of the ring arcs may be understood as material trapped in 7 of 86 possible Galatea corotation-inclination resonance sites, with the 7 resonance sites falling within an azimuthal range of only  $40^\circ$  (cf., Foryta 1993). Thus, the sites are thinly occupied.

We can estimate the probability that this particular arrangement arose by a set of chance events (Esposito and Colwell 1992). One possibility is that each of the resonance locations was filled by an independent event. Examples might be a collision between two rapidly moving particles in one of the resonance zones, or the destruction of a small moon at or near the resonance

site. Each event would release material to be subsequently trapped in that corotation resonance. The probability that the present azimuthal distribution of ring arcs arose by a set of independent events can be estimated by simple combinatorics. The random hypothesis is excluded with likelihood  $1 - 10^{-8}$  (that is, the probability of all the ring arcs clustering so close together by chance is  $10^{-8}$ ).

The conclusion from such calculations is that we are most likely seeing the result of a single and recent event, such as the destruction of a small moon whose smaller fragments were trapped in 7 of 10 contiguous corotation sites. This destruction could also simultaneously leave several large fragments (as explained above) to assist in the azimuthal confinement as proposed in the model of Sicardy and Lissauer (1992), or, alternatively, to be the dust source bodies trapped at Galatea's corotation resonances as proposed by Porco (1991). In either case, these bodies would slow the rapid rate of evolution of the Adams ring (Sec. III.A).

### C. Dust Creation

Neptune's rings are optically thin and dusty. They are significantly dustier than the main rings of Saturn and Uranus, but comparably dusty to Saturn's F ring and the ring of Jupiter. The dust fraction (by area) for the arcs is in the range  $0.2 < f_d < 0.8$  (Fig. 19). Colwell and Esposito (1990b) model the creation of dust from macroscopic particles suffering collisions and meteoroid impact, following similar treatments for the rings of Jupiter (Burns et al. 1980, 1984) and Uranus (Colwell and Esposito 1990a).

Neptune's exospheric drag and the Poynting-Robertson effect are the most rapid processes for radially transporting uncharged dust grains (Colwell and Esposito 1990b). Grains of radius  $1 \mu\text{m}$  near the orbit of the Adams ring would fall, if unhalted, into the planet's atmosphere due to these effects in  $4 \times 10^5 \text{ yr}$ . The situation for charged grains is much more complicated (Northrop and Connerney 1987). Because of the low ion density at Neptune (Richardson et al. 1991), plasma drag is much slower at Neptune than exospheric drag, with time scales of  $\tau \sim 10^7 \text{ yr}$ . However, the rings recapture the vast majority of any dust released from ring particle surfaces so that little dust escapes the rings on these time scales due to these drag processes. The dust content within the rings is ultimately determined by a balance between collisional and meteoroid excavation of dust as sources, and sweep-up by large particles and loss from the ring by drag as sinks.

Voyager 2 detected dust impacts when it crossed Neptune's ring plane at distances of 85,290 km (inbound) and 103,950 km (outbound) from planet center (Stone and Miner 1991), well outside the ring region. (See Table III). Exospheric and plasma densities are negligible for drag processes at those radii; Poynting-Robertson drag is the dominant orbit evolution mechanism and causes small particles' orbits to decay. Thus Proteus could be the source of these dust particles via meteoroid excavation and subsequent orbital decay from the Poynting-Robertson effect.

The simulations of Colwell and Esposito (1990b) reproduce the dust in the rings and at ring plane crossing for reasonable values of the parameters. Calculations in which  $q_{ej}$ , the slope of the size distribution of the ejecta, (where  $n_{ej}(r)dr \propto r^{-q_{ej}}dr$ ), was varied as a free parameter show that  $q_{ej} \gtrsim 3.5$  is required to produce sufficient dust via collisions and impacts to explain the observations. This value is consistent with laboratory experiments (see, e.g., Asada 1985). The dust fraction,  $f_d$ , is most sensitive to the collision velocity because in this simple collision model the ejecta mass is proportional to the kinetic energy of the impact. Similarly, more dust is produced when the large-particle distribution is characterized by a larger particle size because this also increases the kinetic energy of the collisions.

The observed values of  $f_d$  within the rings could be explained by a difference in the large particle collision velocity if, for example, the low- $f_d$  rings had typical random velocities  $v_{ran} = 100 \text{ cm s}^{-1}$  and the high- $f_d$  rings had  $v_{ran} = 200 \text{ cm s}^{-1}$ . An increase in the upper size cutoff from 10 m to 1 km with no change in the lower size cutoff more than doubles  $f_d$ .

Colwell and Esposito combined the steady-state calculations of dust *within* the rings with the Markov chain model for dust transport *between* the rings and moons to produce radial profiles of dust optical depth. One such profile is shown in Fig. 28. In this model, the dominant sources of dust between the rings are the small moons discovered by Voyager. If a sheet of dust extends to the planet, a possibility suggested by Smith et al. (1989), this model requires additional unseen macroscopic source bodies in that region, since insufficient dust escapes the Galle ring to produce a detectable inner sheet. The dust detected at ring plane crossing by the PWS and PRA experiments on Voyager 2 can be derived from meteoroid impacts onto Proteus, providing it has a regolith.

Smith et al. (1989) showed that while the dust content in the diffuse Galle and Lassell rings can be explained by meteoroid bombardment onto unseen parent bodies, as is believed to be the case for the Jovian ring (Burns et al. 1980, 1984), the abundance of dust within the Le Verrier and Adams rings and the arcs is orders of magnitude more abundant than can be explained by this mechanism. They suggested vigorous interparticle collisions as a viable alternative. The more detailed numerical modeling of dust production by Colwell and Esposito verifies that collisions between ring particles are the dominant source of dust in the narrow Neptune rings and arcs; collision velocities of  $\sim 1 \text{ m s}^{-1}$  are required to reproduce the observed dust fractions. (Such values are consistent with the Porco [1991] ring arc confinement model [Sec. III.A.3], which predicts relative velocities  $\sim 2 \text{ m s}^{-1}$ .) In general, in rings where the optical depth is roughly unity or higher, frequent inelastic collisions prevent the growth of the high random velocities required to produce dust through particle collisions; e.g., for the main rings of Uranus, meteoroid excavation is all that is required to explain the majority of the observed dust (Colwell and Esposito 1990a). In extremely low optical depth rings (like Galle and Lassell), collisions are so infrequent as to be inconsequential, and the only

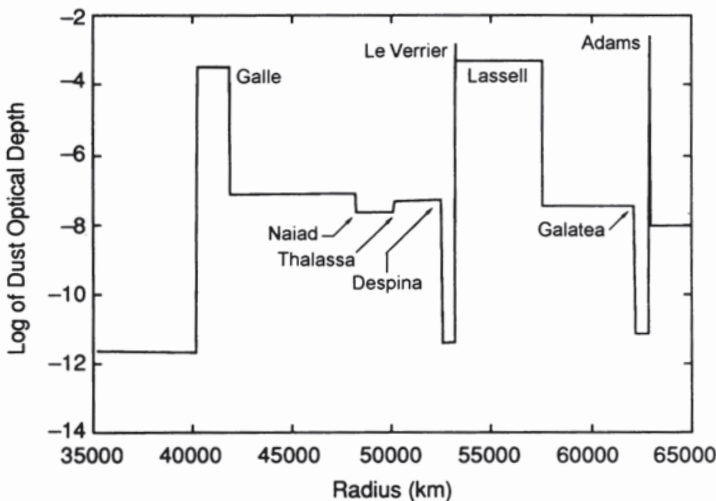


Figure 28. A radial profile of the dust optical depth (for particles  $0.1 < r < 2.0 \mu\text{m}$ ) from Markov chain simulations of dust transport. The locations of Neptune's rings and associated moons are shown (figure from Colwell and Esposito 1990b).

way to produce dust is through meteoroid bombardment. It is noteworthy that the abundance of dust in the narrow Neptune rings and arcs is comparable to that in Saturn's F ring. Perhaps a dust creation model like that of Colwell and Esposito may prove fruitful in explaining the dust content of the F ring.

## V. SUMMARY AND FUTURE DIRECTIONS

The arrival of Voyager 1 at Jupiter in March 1979 opened a new era in the study of the outer solar system. The flight of Voyager 2 past Neptune in August 1989 brought that era to a close. In the intervening decade, the rings surrounding the giant gaseous planets were found to be replete with hitherto unexpected phenomena, enormously complex and diverse, and intimately connected, both presently and evolutionarily, to the satellite systems of their mother planets.

At Neptune, Voyager found a well-developed though tenuous system of rings. Five continuous rings, 2 broad and 3 narrow, plus another narrow discontinuous ring sharing the orbit of the satellite Galatea, all girdle the planet well within its Roche zone. The outermost ring, the Adams ring, contains the only arcs observed so far in Voyager images, and the ones responsible for most of the Earth-based detections of circum-Neptunian material in the mid-1980s. One non-arc groundbased event was a fortuitous occultation by a previously unknown satellite, now known as Larissa, and 3 other events recorded circum-Neptunian material of some sort within Lassell, Galle, and

interior to Galle. The Adams ring arcs are five in number: from leading to trailing, they are Courage, Liberté, Egalité 1, Egalité 2, and Fraternité. They vary in angular extent from  $\sim 1^\circ$  to  $\sim 10^\circ$  and span  $\sim 40^\circ$  in azimuthal range. The Adams ring reaches its maximum brightness in the arc region and becomes substantially fainter with increasing longitude *away* from the arcs. Clumps, presumably denser-than-average concentrations of particles, appear to be common within the arcs, with typical spacings  $\sim 0.5^\circ$ . With the exception of the possible existence of discrete arc-like features in the diffuse rings (detected in Earth-based occultations), and Galatea's companion ring, no large- or small-scale azimuthal structures have yet been seen in any other ring.

Ring orbit pole positions determined from Voyager data for Adams, Le Verrier and Galle, and the orbit normals of most of the inner satellites, are more precise than the spin pole of Neptune determined from Triton's orbit and Voyager tracking data, and differ from the latter by  $\sim 0.06^\circ$ . This circumstance suggests that refinement and revision in the direction of Neptune's pole may be possible. Dust is present throughout the Neptune system within  $\sim 8 R_N$  of the planet's center, and measureable quantities of it were detected even over Neptune's north pole. Further analysis of the *in situ* measurements of near-equatorial dust density maxima may also provide a valuable constraint on the location of Neptune's pole, as dust will tend to settle into a plane determined by the (very accurately known) orbital plane of Triton and the (relatively poorly known) equatorial plane of Neptune.

The phase function and single-scattering albedo of the ring particles may be determined by combining brightness measurements derived from imaging data with the optical depths derived from occultations. If plausible guesses for large particle albedo and small particle phase function can be made,  $\tau$  may be deduced from imaging data alone. (In both cases, the width of the ring must be known or assumed.) Both approaches yield consistent results for the optical depths of the arcs, and the two main narrow rings. Using the arc widths of  $\sim 15$  km measured in the groundbased occultation data,  $\tau_{\text{arcs}} \sim 0.1$ ; for the non-arc Adams ring,  $\tau \sim 0.005$  (for an assumed ring width of 50 km); for an assumed Le Verrier width of 120 km,  $\tau \sim 0.003$ .

The phase function of any object is best characterized when a wide range of phase angles is sampled. Unfortunately, imaging data exist for Neptune's rings at only a few phase angles. Nonetheless, it is clear that the Le Verrier ring has the steepest phase function; the Galle and Lassell rings, the flattest (though the low phase data on these rings are uncertain owing to the rings' low brightnesses in backscattered light); and the Adams ring (non-arc) is intermediate. A steep phase function indicates the presence of fine, wavelength-sized particles which scatter light preferentially in the forward (high-phase) direction. With so few data, only the simplest inferences on particle size distribution can be made. Moreover, there is sufficient ambiguity in the form of the phase function describing the small particle component in the rings that it is impossible to determine the total mass or physical area in

dust. Nonetheless, it seems certain that the arcs and the Le Verrier ring, and under some assumptions, even the non-arc regions of the Adams ring, contain a significant fraction of dust, comparable to that observed in Saturn's F ring. For Lassell, the low phase data are poor and preliminary photometric results indicate a different mix of particle sizes than for Le Verrier or Adams.

Assuming that the groundbased occultation results apply to the "large" particles in the rings, with  $r \gtrsim 50 \mu\text{m}$  (and this will not be the case for very steep particle size distributions), an albedo for the particles in the Egalité arc,  $\tilde{\omega}_L \sim 0.04$ , has been determined using the occultation optical depths and the brightness measurements made from low phase images (which sample mostly the large particle population). The particles in Neptune's rings are apparently as dark as those in the rings of Uranus and may consist of ice "dirtied" with silicates and/or some carbon-bearing material. Inferences made concerning color of the rings indicate that they may be redder than the small satellite of Jupiter, Amalthea.

A kinematic model of the arcs derived from combined Voyager and groundbased data analysis is not yet available. However, Voyager data alone show that the eccentricities of the arc particle orbits are excited by a high wavenumber Lindblad resonance of Galatea into a coherent 30-km amplitude radial distortion which travels through the arcs at the orbital speed of the satellite. A nearby corotation-inclination resonance of the same satellite seems capable of confining the arcs in azimuth, though some arc characteristics are difficult to explain with this model. Also, Galatea's torque on the ring appears to be so great as to lead to a high rate of ring/satellite spreading. Furthermore, the collisional environment within the arcs anticipated from Galatea's perturbations alone implies an arc residence lifetime for colliding particles probably much less than the time ( $\sim 1 \text{ yr}$ ) it takes Galatea's Lindblad perturbation to grow. Small moons, with radii only a few km, would have a dynamical influence comparable to that of Galatea. If placed either at one of the arcs' Lagrange points, or within the arcs themselves, they could assist Galatea in arc confinement, possibly explaining some of the problems mentioned above with the single-satellite model, as well as slow the rapid retreat of the Adams ring from the satellite. Unluckily, bodies this small are well below the detection limit in Voyager images.

Short ring lifetimes inferred from meteoroid bombardment and Galatea's torque on the Adams ring imply interrelated histories for rings and nearby small moons in the Neptune system. Detailed numerical simulations demonstrate the plausibility of a model where disrupted satellites provide the source of the Neptune rings and arcs. Although these simulations depend in detail on many parameters that are poorly known for Neptune, the following sequence emerges.

A satellite is disrupted, leaving behind a narrow ring and large fragments or moons. Some fragments remain clustered close together in longitude and become the source of the arcs seen in the Adams ring. The system evolves until the moons ultimately confine the rings radially and azimuthally. Portions

as a unit. Moons excite eccentricities in the ring particle orbits which lead to collisions energetic enough to create the dust (and its size distribution) observed by the Voyager cameras. Better knowledge of the Neptune family impactors, the dust environment, and the mechanics of cratering and disrupting partly consolidated bodies would help to constrain and confirm these ideas.

The information gathered by Voyager on Neptune's rings will remain the largest collection of its kind for many years to come, and much of the work on Voyager data reviewed in this chapter remains to be completed. Derivation of particle properties from imaging photometry, and from the combination of imaging and occultation data, is still in progress. A search through Voyager images for the features responsible for the three groundbased occultation events falling within and interior to the Lassell ring should eventually be conducted. The preliminary results on the orbital geometry of the Le Verrier and Galle rings will be refined, and a complete kinematical/geometric model for the Adams ring arcs will be derived once Voyager and groundbased arc data are analyzed together. With this information in hand, it should be possible to refine the direction of Neptune's spin axis, as well as verify that the conditions for corotational shepherding by Galatea—such as a nonzero mutual inclination between the Adams ring and Galatea's orbit—are still met.

Data gathering on Neptune's rings in the post-Voyager era will be far slower than it was prior to 1989. Neptune is moving away from the galactic plane, and the opportunities to observe stellar occultations will grow more rare with time. Between 1994 and the turn of the century, Neptune is expected to occult 31 stars having visual magnitudes as large as  $V = 15.46$  (Mink et al. 1992); nine of these will be occultations by the region of the Adams ring containing the arcs and the brightest of these has a magnitude of  $V = 12.45$ . Considering that the inter-arc regions, which comprise  $\sim 50\%$  of the  $40^\circ$  span of the arcs, are insufficiently dense to cause a detectable dip in an occultation lightcurve unless the star is extremely bright, and considering that typical near-infrared ( $K$ ) magnitudes are generally smaller than  $V$  by only 1.5, the chances of a positive arc detection, even if all 9 occultations are successfully observed, are rather slim. Only with great good fortune will there be new data on Neptune's arcs in the following half decade. Not until the next Neptune-bound spacecraft arrives at its destination can we expect another view of Neptune's rings as expansive and precise as the one so faithfully bestowed by Voyager.

*Acknowledgments.* We are happy to thank J. Burns, R. Canup, J. Colwell, A. Dobrovolskis, C. Ferrari, V. Haemmerle, J. Holberg, D. Kary, R. Kolvoord, B. Mauk, I. Mosqueira, W. M. Owen, Jr., M. Showalter, B. Sicardy, and G. Stewart for helpful discussions and/or release of results in advance of publication. CP, PN and LE acknowledge support by the NASA Neptune Data Analysis Program; CP, JC, JL, and LE acknowledge support by the NASA Planetary Geology and Geophysics Program.

## REFERENCES

- Acuña, M. H., and Ness, N. F. 1976. The complex main magnetic field of Jupiter. *J. Geophys. Res.* 81:2917–2922.
- Asada, N. 1985. Fine fragments in high-velocity impact environments. *J. Geophys. Res.* 90:12445–12453.
- Athanassoula, E., and Bosma, A. 1985. Shells and rings around galaxies. *Ann. Rev. Astron. Astrophys.* 23:147–168.
- Banfield, D., and Murray, N. 1992. A dynamical history of the inner Neptunian satellites. Neptune and Triton, Jan. 6–10, Tucson, Ariz., Abstract book, p. 5.
- Borderies, N. 1989. Properties of possible polar rings around Neptune. *Icarus* 77:135–147.
- Borderies, N., Goldreich, P., and Tremaine, S. 1989. The formation of sharp edges in planetary rings by nearby satellites. *Icarus* 80:344–360.
- Broadfoot, A. L., Herbert, F., Holberg, J. B., Hunten, D. M., Kumar, S., Sandel, B. R., Shemansky, D. E., Smith, G. R., Yelle, R. V., Strobel, D. F., Moos, H. W., Donahue, T. M., Atreya, S. K., Bertaix, J. L., Blamont, J. E., McConnell, J. C., Dessler, A. J., Linick, S., and Springer, R. 1986. Ultraviolet spectrometer observations of Uranus. *Science* 233:74–79.
- Broadfoot, A. L., Atreya, S. K., Bertaix, J. L., Blamont, J. E., Dessler, A. J., Donahue, T. M., Forrester, W. T., Hall, D. T., Herbert, F., Holberg, J. B., Hunten, D. M., Krasnopolsky, V. A., Linick, S., Lunine, J. I., McConnell, J. C., Moos, H. W., Sandel, B. R., Schneider, N. M., Shemansky, D. E., Smith, G. R., Strobel, D. F., and Yelle, R. V. 1989. Ultraviolet spectrometer observations of Neptune and Triton. *Science* 246:1459–1465.
- Brouwer, D., and Clemence, G. M. 1961. *Methods of Celestial Mechanics* (New York: Academic Press).
- Burns, J. A., Showalter, M. R., Cuzzi, J. N., and Pollack, J. B. 1980. Physical processes in Jupiter's ring: Clues to its origin by Jove! *Icarus* 44:339–360.
- Burns, J. A., Showalter, M. R., and Morfill, G. E. 1984. The ethereal rings of Jupiter and Saturn. In *Planetary Rings*, eds. R. Greenberg and A. Brahic (Tucson: Univ. of Arizona Press), pp. 200–272.
- Burns, J. A., Schaffer, L. A., Greenberg, R. J., and Showalter, M. R. 1985. Lorentz resonances and the structure of the Jovian ring. *Nature* 316:115–119.
- Canup, R. M., and Esposito, L. W. 1995. Accretion in the Roche zone, I. Coexistence of rings and ringmoons. *Icarus*, in press.
- Cheng, A. F., Mauk, B. H., Krimigis, S. M., and MacLennan, C. B. 1992. Energetic ion phase space densities in Neptune's magnetosphere. Neptune and Triton, Jan. 6–10, Tucson, Ariz., Abstract book, p. 15.
- Colwell, J. E., and Esposito, L. W. 1990a. A numerical model of the Uranian dust rings. *Icarus* 86:530–560.
- Colwell, J. E., and Esposito, L. W. 1990b. A model of dust production in the Neptune ring system. *Geophys. Res. Lett.* 17:1741–1744.
- Colwell, J. E., and Esposito, L. W. 1992. Origins of the rings of Uranus and Neptune. I. Statistics of satellite disruptions. *J. Geophys. Res.* 97:10227–10241.
- Colwell, J. E., and Esposito, L. W. 1993. Origins of the rings of Uranus and Neptune. II. Initial distributions of disrupted satellite fragments. *J. Geophys. Res.* 98:7387–7401.
- Connerney, J. E., Acuna, M., and Ness, N. 1991. The magnetic field of Neptune. *J. Geophys. Res.* 96:19023–19042.
- Cooke, M. L. 1991. *Saturn's Rings: Photometric Studies of the C Ring and Radial Variation in the Keeler Gap*. Ph.D. Thesis, Cornell Univ.

- Covault, C. E., Glass, I. S., French, R. G., and Elliot, J. L. 1986. The 7 and 25 June 1985 Neptune occultations: Constraints on the putative Neptune arc. *Icarus* 67:126–133.
- Cuzzi, J. N. 1985. Rings of Uranus: Not so thick, not so black. *Icarus* 63:312–316.
- Cuzzi, J. N., and Durisen, R. H. 1990. Bombardment of Planetary Rings by Meteoroids: General Formulation and Effects of Oort Cloud Projectiles. *Icarus* 84:467–501.
- Cuzzi, J. N., and Esposito, L. W. 1987. The rings of Uranus. *Sci. Amer.* 237:52–66.
- Cuzzi, J. N., and Scargle, J. 1985. Wavy edges suggest moonlet in Encke's Gap. *Astrophys. J.* 292:276–290.
- Cuzzi, J. N., Lissauer, J. J., Esposito, L. W., Holberg, J. B., Marouf, E. A., Tyler, G. L., and Boisshot, A. 1984. Saturn's rings: Properties and processes. In *Planetary Rings*, eds. R. Greenberg and A. Brahic (Tucson: Univ. of Arizona Press), pp. 73–199.
- Davis, D., and Ryan, E. 1990. On collisional disruption: Experimental results and scaling laws. *Icarus* 83:156–182.
- Dermott, S. F. 1984. Dynamics of narrow rings. In *Planetary Rings*, eds. R. Greenberg and A. Brahic (Tucson: Univ. of Arizona Press), pp. 589–637.
- Dermott, S. F., Malhotra, R., and Murray, C. D. 1989. Dynamics of the Uranian and Saturnian satellite systems: a chaotic route to melting Miranda? *Icarus* 76:295–334.
- Dobrovolskis, A. R. 1980. Where are the rings of Neptune? *Icarus* 43:222–226.
- Dobrovolskis, A. R., Borderies, N. B., and Steiman-Cameron. 1989a. Stability of polar rings around Neptune. *Icarus* 81:132–144.
- Dobrovolskis, A. R., Steiman-Cameron, T. Y., and Borderies, N. J. 1989b. Neptune may have polar rings. *Geophys. Res. Lett.* 16:949–952.
- Dones, L. 1991. A Recent Cometary Origin for Saturn's Rings? *Icarus* 92:194–203.
- Dones, L., Cuzzi, J. N., and Showalter, M. R. 1993. Voyager photometry of Saturn's A ring. *Icarus* 105:184–215.
- Doyle, L. R., Dones, L., and Cuzzi, J. H. 1989. Radiative transfer modelling of Saturn's outer B ring. *Icarus* 80:104–135.
- Elliot, J. L., French, R. G., Meech, K. J., and Elias, J. H. 1984. Structure of the Uranian rings I: Square-well model and particle size constraints. *Astron. J.* 89:1587–1603.
- Elliot, J. L., Baron, R. L., Dunham, E. W., French, R. G., Meech, K. J., Mink, D. J., Allen, D. A., Ashley, C. B., Freeman, K. C., Erickson, E. F., Goguen, J., and Hammel, H. B. 1985. The 1983 June 15 occultation by Neptune. I. Limits on a possible ring system. *Astron. J.* 90:2615–2623.
- Elliot, J. L., Mink, D. J., Elias, J. H., Baron, R. L., Dunham, E. W., Pingree, J. E., French, R. G., Liller, W., Nicholson, P. D., Jones, T. J., and Franz, O. G. 1981. No evidence of rings around Neptune. *Nature* 294:526–529.
- Esposito, L. W. 1986. Structure and evolution of Saturn's rings. *Icarus* 67:345–357.
- Esposito, L. W., and Colwell, J. E. 1989. Creation of the Uranus rings and dust bands. *Nature* 339:637–740.
- Esposito, L. W., and Colwell, J. E. 1992. Neptune's rings and satellite system: Collisional origin and evolution. *Eos: Trans. AGU* 73:177 (abstract).
- Esposito, L. W., Cuzzi, J. N., Holberg, J. B., Marouf, E. A., Tyler, G. L., and Porco, C. C. 1984. Saturn's rings: structure, dynamics and particle properties. In *Saturn*, eds. T. Gehrels and M. S. Matthews (Tucson: Univ. of Arizona Press), pp. 463–545.
- Esposito, L. W., Brahic, A., Burns, J. A., and Marouf, E. A. 1991. Particle properties and processes in Uranus' rings. In *Uranus*, eds. J. T. Bergstrahl, E. D. Miner and M. S. Matthews (Tucson: Univ. of Arizona Press), pp. 410–468.

- Ferrari, C., and Brahic, A. 1991. Neptune's arcs and narrow rings: Morphology and nature. *Bull. Amer. Astron. Soc.* 23:1178 (abstract).
- Ferrari, C., and Brahic, A. 1994. Azimuthal brightness asymmetries in planetary rings. I: Neptune's arcs and narrow rings. *Icarus* 111:193–210.
- Foryta, D. W. 1993. Étude numérique des anneaux planétaires application aux arcs de Neptune. Ph.D. Thesis, Observatoire de Paris.
- Franklin, F. A., and Colombo, G. 1978. On the azimuthal brightness variations of Saturn's rings. *Icarus* 33:279–287.
- Franklin, F. A., Lecar, M., and Wiesel, W. 1984. Ring particle dynamics in resonances. In *Planetary Rings*, eds. R. Greenberg and A. Brahic (Tucson: Univ. of Arizona Press), pp. 562–588.
- Freeman, K. C., and Lynga, G. 1970. Data for Neptune from occultation observations. *Astrophys. J.* 160:767–780.
- French, R. G., Elliot, J. L., French, L. M., Kangas, J. A., Meech, K. J., Ressler, M. E., Buie, M. W., Frogel, J. A., Holberg, J. B., Fuensalida, J. J., and Joy, M. 1988. Uranian ring orbits from Earth-based and Voyager occultation observations. *Icarus* 73:349–378.
- French, R. G., Elliot, J. L., and Levine, S. E. 1986. Structure of the Uranian rings. II. Ring orbits and widths. *Icarus* 67:134–163.
- French, R. G., Nicholson, P. D., Porco, C. C., and Marouf, E. A. 1991. Dynamics and structure of the Uranian rings. In *Uranus*, eds. J. T. Bergstrahl, E. D. Miner and M. S. Matthews (Tucson: Univ. of Arizona Press), pp. 410–468.
- French, R. G., Maene, S., Mason, E. C., McGhee, C. A., Nicholson, P. D., Matthews, K., and Roques, F. 1993. Delimiting Neptune's arcs: Stellar occultation observations in the vicinity of Liberté. *Bull. Amer. Astron. Soc.* 25:1110 (abstract).
- Goldreich, P., and Tremaine, S. 1979. Towards a theory for the uranian rings. *Nature* 277:97–99.
- Goldreich, P., and Tremaine, S. 1982. The dynamics of planetary rings. *Ann. Rev. Astron. Astrophys.* 20:249–283.
- Goldreich, P., Tremaine, S., and Borderies, N. 1986. Towards a theory for Neptune's arc rings. *Astron. J.* 92:490–494.
- Gor'kavyj, N. N. 1991. The arcs near Neptune as chains of epitons in a continuous transparent ring. *Soviet Astron. Lett.* 17:428–432.
- Gor'kavyj, N. N., and Taidakova, T. A. 1991. Theory of the Neptunian arcs. II. Dynamics of epitons in the ring. *Soviet Astron. Lett.* 17:462–465.
- Gor'kavyj, N. N., Taidakova, T. A., and Gaftonyuk, N. M. 1991. Theory of the Neptunian arcs. I. Stability of an individual epiton. *Soviet Astron. Lett.* 17:457–461.
- Greenberg, R., Wacker, J. F., Hartmann, W. K., and Chapman, C. R. 1978. Planetesimals to planets: Numerical simulation of collisional evolution. *Icarus* 35:1–26.
- Greenzweig, Y., and Lissauer, J. J. 1990. Accretion rates of protoplanets. *Icarus* 87:40–77.
- Gresh, D. L., Marouf, E. A., Tyler, G. L., Rosen, P. A., and Simpson, R. A. 1989. Voyager radio occultation by Uranus' rings. I. Observational results. *Icarus* 77:131–168.
- Grün, E., Morfill, G. E., and Mendis, D. A. 1984. Dust-magnetosphere interactions. In *Planetary Rings*, eds. R. Greenberg and A. Brahic (Tucson: Univ. of Arizona Press), pp. 275–332.
- Guinan, E. F., Harris, C. C., and Maloney, F. P. 1982. Evidence for a ring system of Neptune. *Bull. Amer. Astron. Soc.* 14:658 (abstract).
- Gurnett, D. A., Kurth, W. S., Scarf, F. L., Burns, J. A., Cuzzi, J. N., and Grün, E. 1987. Micron-sized particle impacts detected near Uranus by the Voyager 2 Plasma Wave Instrument. *J. Geophys. Res.* 92:14959–14968.

- Gurnett, D. A., Kurth, W. S., Poynter, R. L., Granroth, L. J., Cairns, I. H., Macek, W. M., Moses, S. L., Coroniti, F. V., Kennel, C. F., and Barbosa, D. D. 1989. First plasma wave observations at Neptune. *Science* 246:1494–1498.
- Gurnett, D. A., Kurth, W. S., Granroth, L. J., Allendorf, S. C., and Poynter, R. L. 1991. Micron-sized particles detected near Neptune by the Voyager 2 Plasma Wave Instrument. *J. Geophys. Res.* 96:19177–19186.
- Hamilton, D. P., and Burns, J. A. 1992. Orbital evolution of dust grains around Neptune. Neptune and Triton, Jan. 6–10, Tucson, Ariz., Abstract book, p. 29.
- Hamilton, D. P., Burns, J. A., Horanyi, M., and Gurnett, D. A. 1990. Dynamics of Neptune's dust halo. *Bull. Amer. Astron. Soc.* 22:1043 (abstract).
- Hénon, M. 1981. A simple model of Saturn's rings. *Nature* 293:33–35.
- Hénon, M., and Petit, J.-P. 1986. Series expansions for encounter-type solutions of Hill's Problem. *Celestial Mech.* 38:67–100.
- Holberg, J. B., Nicholson, P. D., French, R. G., and Elliot, J. L. 1987. Stellar occultation probes of the Uranian rings at 0.1 and 2.2  $\mu\text{m}$ : A comparison of Voyager and Earth-based results. *Astron. J.* 94:178–188.
- Hood, L. L. 1989. Investigation of the Saturn dust environment from the analysis of energetic charged particle measurements. In *Cassini Mission Saturn Orbiter Proposal Information Package, Volume XIII: Physical Models*, JPL D-6464.
- Horanyi, M., and Porco, C. 1993. Where exactly are the arcs of Neptune? *Icarus* 106:525–535.
- Horn, L. J., Hui, J., Lane, A. L., and Colwell, J. E. 1990. Observations of neptunian rings by Voyager photopolarimeter experiment. *Geophys. Res. Lett.* 17:1745–1748.
- Housen, K. R., and Holsapple, K. A. 1990. On the fragmentation of asteroids and planetary satellites. *Icarus* 84:226–253.
- Hubbard, W. B. 1986. 1981N1: A Neptune arc? *Science* 231:1276–1278.
- Hubbard, W. B., Brahic, A., Sicardy, B., Elicer, L. R., Roques, F., and Vilas, F. 1986. Occultation detection of a Neptunian ring-like arc. *Nature* 319:636–640.
- Hubbard, W. B., Frecker, J. E., Gehrels, J. A., Gehrels, T., Hunten, D. M., Lebofsky, L. A., Smith, B. A., Tholen, D. J., Vilas, F., Zellner, B., Avey, H. P., Mottram, K., Murphy, T., Varnes, B., Carter, B., Nielsen, A., Page, A. A., Fu, H. H., Wu, H. H., Kennedy, H. D., Waterworth, M. D., and Reitsema, H. J. 1985. Results from observations of the 15 June 1983 occultation by the Neptune system. *Astron. J.* 90:655–667.
- Jacobson, R. A., Riedel, J. E., and Taylor, A. H. 1991. The orbits of Triton and Nereid from spacecraft and Earth-based observations. *Astron. Astrophys.* 247:565–575.
- Julian, W. H., and Toomre, A. 1966. Non-axisymmetric responses of differentially rotating disks of stars. *Astrophys. J.* 146:810–832.
- Klemola, A. R., Liller, W., Marsden, B. G., and Elliot, J. L. 1978. Predicted occultations by Neptune 1978–1980. *Astron. J.* 83:205–207.
- Klemola, A. R., and Mink, D. J. 1991. Occultations by Uranus and Neptune: 1991–1999. *Astron. J.* 102:389–394.
- Kolvoord, R. A., and Burns, J. A. 1992. Three-dimensional perturbations of particles in a narrow planetary ring. *Icarus* 95:253–264.
- Kovalevsky, J., and Link, F. 1969. Diameter, flattening, and optical properties of the upper atmosphere of Neptune as derived from the occultation of BD –17°4388. *Astron. Astrophys.* 2:398–412.
- Lane, A. L., Hord, C. W., West, R. A., Esposito, L. E., Coffeen, D. L., Sato, M., Simmons, K. E., Pompfrey, R. B., and Morris, R. B. 1982. Photopolarimetry from Voyager 2: Preliminary results on Saturn, Titan, and the rings. *Science* 215:537–543.
- Lane, A. L., West, R. A., Hord, C. W., Nelson, R. M., Simmons, K. E., Pryor,

- W. R., Esposito, L. E., Horn, L. J., Wallis, B. D., Buratti, B. J., Brophy, T. G., Yanamandra-Fisher, P., Colwell, J. E., Bliss, D. A., Mayo, M. J., and Smythe, W. D. 1989. Photometry from Voyager 2: Initial results from the Neptunian atmosphere, satellites, and rings. *Science* 246:1450–1454.
- Lin, D. N. C., Papaloizou, J. C. B., and Ruden, S. P. 1987. On the confinement of planetary arcs. *Mon. Not. Roy. Astron. Soc.* 227:75–95.
- Lissauer, J. J. 1985. Shepherding model for Neptune's arc ring. *Nature* 318:544–545.
- Lissauer, J. J., Peale, S. J., and Cuzzi, J. N. 1984. Ring torque on Janus and the melting of Enceladus. *Icarus* 58:159–168.
- Lissauer, J. J., and Peale, S. J. 1986. The production of “braids” in Saturn's F ring. *Icarus* 67:358–374.
- Lissauer, J. J., Shu, F. H., and Cuzzi, J. N. 1981. Moonlets in Saturn's rings? *Nature* 292:707–711.
- Lissauer, J. J., Goldreich, P., and Tremaine, S. 1985. Evolution of the Janus-Epimetheus coorbital resonance due to torques from Saturn's rings. *Icarus* 64:425–434.
- Lissauer, J. J., Squyres, S. W., and Hartmann, W. K. 1988. Bombardment history of the Saturn system. *J. Geophys. Res.* 93:13776–13804.
- Manfroid, J., Haefner, R., and Bouchet, P. 1986. New evidence for a ring around Neptune. *Astron. Astrophys.* 157:L3–L5.
- Marley, M. S., Hubbard, W. B., and Porco, C. C. 1989. Neptune ring arc confinement and planetary oscillation modes. *Bull. Amer. Astron. Soc.* 21:913 (abstract).
- Marley, M. S., and Porco, C. C. 1993. Planetary acoustic mode seismology: Saturn's rings. *Icarus* 106:508–524.
- Marouf, E. A., Tyler, G. L., and Rosen, P. A. 1986. Profiling Saturn's rings by radio occultation. *Icarus* 68:120–166.
- Mauk, B. H., Kane, M., Keath, E. P., Cheng, A. F., Krimigis, S. M., Armstrong, T. P., and Ness, N. F. 1990. Energetic charged particle angular distributions near ( $<2 R_N$ ) and over the pole of Neptune. *Geophys. Res. Lett.* 17:1701.
- Mauk, B. H., Keath, E. P., Kane, M., Krimigis, S. M., Cheng, A. F., Acuña, M. H., Armstrong, T. P., and Ness, N. F. 1991. The magnetosphere of Neptune; hot plasmas and energetic particles. *J. Geophys. Res.* 96:19061–19085.
- Mauk, B. H., Krimigis, S. M., Ness, N. F., and Acuña, M. H. 1992. Aspects of the signatures of charged particle material interactions within Neptune's magnetosphere. Neptune and Triton, Jan. 6–10, Tucson, Ariz., Abstract book, p. 52.
- Meyer-Vernet, N., Aubier, M. G., and Pedersen, B. M. 1986. Voyager 2 at Uranus: Grain impacts in the ring plane. *Geophys. Rev. Lett.* 13:617–620.
- Michel, F. C. 1981. Collisionless Saturnian rings. *Planet. Space Sci.* 29:1137–1142.
- Mink, D. J., and Klemola, A. R. 1985. Predicted occultations by Uranus, Neptune and Pluto: 1985–1990. *Astron. J.* 90:1894–1899.
- Mink, D. J., Klemola, A. R., and Elliot, J. L. 1981. Predicted occultations by Neptune: 1981–1984. *Astron. J.* 86:135–137.
- Mink, D. J., Maene, S., French, R. G., and Klemola, A. R. 1992. Occultations of faint stars by Neptune and its rings: 1992–1999. *Icarus* 99:430–435.
- Murray, C. D., and Thompson, R. P. 1990. Orbits of shepherd satellites deduced from the structure of the rings of Uranus. *Nature* 348:499–502.
- Narayan, R., and Hubbard, W. B. 1988. Theory of anisotropic refractive scintillation—application to stellar occultations by Neptune. *Astrophys. J.* 325:503–518.
- Nicholson, P. D., and Jones, T. J. 1980. Occultations by Neptune. *IAU Circ.* 3515.
- Nicholson, P. D., McLeod, B. A., Gilmore, G., Buie, M. W., and Matthews, K. 1988. Near-infrared stellar-occultation predictions for Uranus and Neptune: 1987–1990. *Astron. J.* 95:562–575.
- Nicholson, P. D., Cooke, M. L., Matthews, K., Elias, J. H., and Gilmore, G. 1990.

- Five stellar occultations by Neptune: Further observations of ring arcs. *Icarus* 87:1–39.
- Nicholson, P. D., Mosqueira, I., and Matthews, K. 1995. Stellar occultation observations of Neptune's rings: 1984–1988. *Icarus*, in press.
- Northrop, T. B., and Connerney, J. E. 1987. A meteorite erosion model and the age of Saturn's rings. *Icarus* 70:124–137.
- Ockert, M. E., Cuzzi, J. N., Porco, C. C., and Johnson, T. V. 1987. Uranian ring photometry: Result from Voyager 2. *J. Geophys. Res.* 92:14969–14978.
- Owen, W. M., Jr., and Synnott, S. P. 1987. Orbits of the ten small satellites of Uranus. *Astron. J.* 93:1268–1271.
- Owen, W. M., Jr., Vaughan, R. M., and Synnott, S. P. 1991. Orbits of the six new satellites of Neptune. *Astron. J.* 101:1511–1515.
- Paonessa, M., and Cheng, A. F. 1987. Satellite sweeping in offset, tilted dipole fields. *J. Geophys. Res.* 92:1160.
- Paranicas, C. P., and Cheng, A. F. 1991. Theory of ring sweeping of energetic particles. *J. Geophys. Res.* 96:19123–19130.
- Pedersen, B. M., Meyer-Vernet, N., Aubier, M. G., and Zarka, P. 1991. Dust distribution around Neptune: Grain impacts near the ring plane measured by the Voyager Planetary Radio Astronomy experiment. *J. Geophys. Res.* 96:19187–19196.
- Pollack, J. B., and Cuzzi, J. N. 1980. Scattering by nonspherical particles of size comparable to a wavelength: a new semiempirical theory and its application to tropospheric aerosols. *J. Atmos. Sci.* 37:868–881.
- Porco, C. C. 1991. An explanation for Neptune's ring arcs. *Science* 253:995–1001.
- Porco, C. C., and Goldreich, P. 1987. Shepherding of the uranus rings. I. Kinematics. *Astron. J.* 93:724–729.
- Porco, C. C., and Nicholson, P. D. 1987. Eccentric features in Saturn's outer C ring. *Icarus* 72:437–467.
- Porco, C. C., Nicholson, P. D., Borderies, N., Danielson, G. E., Goldreich, P., Holberg, J. B., and Lane, A. L. 1984a. The eccentric Saturnian ringlets at 1.29  $R_S$  and 1.45  $R_S$ . *Icarus* 60:1–16.
- Porco, C. C., Danielson, G. E., Goldreich, P., Holberg, J. B., and Lane, A. L. 1984b. Saturn's nonaxisymmetric ring edges at 1.95  $R_S$  and 2.27  $R_S$ . *Icarus* 60:17–28.
- Porco, C. C., Cuzzi, J. N., Ockert, M. E., and Terrie, R. J. 1987. The color of the Uranian rings. *Icarus* 72:69–78.
- Porco, C. C., Haemmerle, V., Owen, W. M., Jr., and Holberg, J. 1995. Neptune's ring and satellite systems: Geometry, kinematics and dynamics from combined groundbased and Voyager observations. In preparation.
- Porco, C. C., Cuzzi, J. N., Esposito, L. W., Lissauer, J. J., and Nicholson, P. D. 1992. The Neptune ring system. Neptune and Triton, Jan. 6–10, Tucson, Ariz., Abstract book, p. 67.
- Reitsema, H. J., Hubbard, W. B., Lebofsky, L. A., and Tholen, D. J. 1982. Occultation by a possible third satellite of Neptune. *Science* 215:289–291.
- Richardson, J. D., Belcher, J. W., Zhang, M., and McNutt, Jr., R. L. 1991. Low-energy norns near Neptune. *J. Geophys. Res.* 96:18993–19011.
- Salo, H. 1991. Numerical simulations of dense collisional systems. *Icarus* 90:254–270.
- Schaffer, L., and Burns, J. A. 1987. The dynamics of weakly charged dust: Motion through Jupiter's gravitational and magnetic fields. *J. Geophys. Res.* 92:2264–2280.
- Schaffer, L., and Burns, J. A. 1992. Lorentz resonances and the vertical structure of dusty rings; analytical and numerical results. *Icarus* 96:65–84.
- Selesnick, R. S. 1992. Magnetic field models from energetic particle data at Neptune. *J. Geophys. Res.* 97:10857–10863.

- Selesnick, R. S., and Stone, E. C. 1991. The electron absorption signature of 1989N1. *J. Geophys. Res.* 96:19137–19148.
- Selesnick, R. S., and Stone, E. C. 1992. Energetic particle signatures of satellites and rings in Neptune's magnetosphere. *Adv. Space Phys.* 11:71–79.
- Showalter, M. R. 1991. Visual detection of 1981S13, Saturn's eighteenth satellite, and its role in the Encke gap. *Science* 351:709–713.
- Showalter, M. R., and Burns, J. A. 1982. A numerical study of Saturn's F ring, *Icarus* 52:526–544.
- Showalter, M. R., and Cuzzi, J. N. 1992a. Structure and particle properties of Neptune's ring system. Neptune and Triton, Jan. 6–10, Tucson, Ariz., Abstract book, p. 78.
- Showalter, M. R., and Cuzzi, J. N. 1992b. Physical properties of Neptune's ring system. *Bull. Amer. Astron. Soc.* 24:1029 (abstract).
- Showalter, M. R., and Cuzzi, J. N. 1993. Seeing ghosts: Photometry of Saturn's G ring. *Icarus* 103:124–143.
- Showalter, M. R., and Cuzzi, J. N. 1995. Structure and particle properties of Neptune's ring system. In preparation.
- Showalter, M. R., Cuzzi, J. N., Marouf, E. A., and Esposito, L. W. 1986. Satellite "wakes" and the orbit of the Encke gap moonlet. *Icarus* 66:297–323.
- Showalter, M. R., Burns, J. A., Cuzzi, J. N., and Pollack, J. B. 1987. Jupiter's ring system: new results on structure and particle properties. *Icarus* 69:458–498.
- Showalter, M. R., Cuzzi, J. N., and Larson, S. M. 1991. Structure and particle properties of Saturn's E ring. *Icarus* 94:451–473.
- Showalter, M. R., Pollack, J. B., Ockert, M. E., Doyle, L. R., and Dalton, J. B. 1992. A photometric study of Saturn's F ring. *Icarus* 100:394–411.
- Shu, F. H. 1984. Waves in planetary rings. In *Planetary Rings*, eds. R. Greenberg and A. Brahic (Tucson: Univ. of Arizona Press), pp. 513–561.
- Shu, F. H., Dones, L., Lissauer, J. J., Yuan, C., and Cuzzi, J. N. 1985. Nonlinear spiral density waves: viscous damping. *Astrophys. J.* 299:542–573.
- Sicardy, B. 1988. Etude observationnelle, analytique et numérique des environnements planétaires. Applications aux anneaux de Saturne et d'Uranus et aux arcs de Neptune. Ph.D. Thesis, Univ. of Paris 7.
- Sicardy, B. 1991. Numerical exploration of planetary arc dynamics. *Icarus* 89:197–219.
- Sicardy, B., and Lissauer, J. J. 1992. Dynamical models of the arcs in Neptune's 63K ring (1989N1R). *Adv. Space Res.* 12:81–95.
- Sicardy, B., Roques, R., and Brahic, A. 1991. Neptune's rings, 1983–1989: Ground-based stellar occultation observations. I. Ring-like arc detection. *Icarus* 89:220–243.
- Sinclair, A. T. 1972. On the origin of the commensurabilities amongst the satellites of Saturn. *Mon. Not. Roy. Astron. Soc.* 160:169–187.
- Smith, B. A., Soderblom, L. A., Beebe, R., Boyce, J., Briggs, G., Bunker, A., Collins, S. A., Hansen, C. J., Johnson, T. V., Mitchell, J. L., Terrile, R. J., Carr, M., Cook, A. F., II, Cuzzi, J., Pollack, J. B., Danielson, G. E., Ingersoll, A., Davies, M. E., Hunt, G. E., Masursky, H., Shoemaker, E. M., Morrison, D., Owen, T., Sagan, C., Veverka, J., Strom, R., and Suomi, V. E. 1981. Encounter with Saturn: Voyager 1 imaging science results. *Science* 212:163–191.
- Smith, B. A., Soderblom, L. A., Batson, R., Bridges, P., Inge, J., Masursky, H., Shoemaker, E. M., Beebe, R. F., Boyce, J. M., Briggs, G. A., Bunker, A., Collins, S. A., Hansen, C. J., Johnson, T. V., Mitchell, J. L., Terrile, R. J., Cook, A. F., Cuzzi, J. N., Pollack, J. B., Danielson, G. E., Ingersoll, A. P., Davies, M. E., Hunt, G. E., Morrison, D., Owen, T., Sagan, C., Veverka, J., Strom, R., and Suomi, V. E. 1982. A new look at the Saturn system: The Voyager 2 images. *Science*

215:504-537.

- Smith, B. A., Soderblom, L. A., Beebe, R., Bliss, D., Boyce, J. M., Brahic, A., Briggs, G. A., Brown, R. H., Collins, S. A., Cook, A. F., II, Croft, S. K., Cuzzi, J. N., Danielson, G. E., Davies, M. E., Dowling, T. E., Godfrey, D., Hansen, C. J., Harris, C., Hunt, G. E., Intersoll, A. P., Johnson, T. V., Krauss, R. J., Masursky, H., Morrison, D., Owen, T., Plescia, J. B., Pollack, J. B., Porco, C. C., Rages, K., Sagan, C., Shoemaker, E. M., Sromovsky, L. A., Stoker, C., Strom, R. G., Suomi, V. E., Synott, S. P., Terrile, R. J., Thomas, P., Thompson, W. R., and Veverka, J. 1986. Voyager 2 in the Uranian system: Imaging science results. *Science* 233:43-64.
- Smith, B. A., Soderblom, L. A., Banfield, D., Barnet, C., Basilevsky, A. T., Beebe, R. F., Boller, K., Boyce, J. M., Brahic, A., Briggs, G. A., Brown, R. H., Chyba, C., Collins, S. A., Colvin, T., Cook, A. F., II, Crisp, D., Croft, S. K., Cruikshank, D., Cuzzi, J. N., Danielson, G. E., Davies, M. E., De Jong, E., Dones, L., Godfrey, D., Goguen, J., Grenier, I., Haemmerle, V. R., Hammel, H., Hansen, C. J., Helfenstein, C. P., Howell, C., Hunt, G. E., Ingersoll, A. P., Johnson, T. V., Kargel, J., Kirk, R., Kuehn, D. I., Limaye, S., Masursky, H., McEwen, A., Morrison, D., Owen, T., Owen, W., Pollack, J. B., Porco, C. C., Rages, K., Showalter, M., Sicardy, B., Simonelli, D., Spencer, J., Sromovsky, B., Stoker, C., Strom, R. G., Suomi, V. E., Synott, S. P., Terrile, R. J., Thomas, P., Thompson, W. R., Verbiscer, A., and Veverka, J. 1989. Voyager 2 at Neptune: Imaging science results. *Science* 246:1422-1449.
- Soter, S. 1971. The dust belts of Mars. CCSR report #462 (Ithaca, N. Y.: Cornell Univ.).
- Stevenson, D. J., Harris, A. W., and Lunine, J. I. 1986. Origins of satellites. In *Satellites*, eds. J. A. Burns and M. S. Matthews (Tucson: Univ. of Arizona Press) pp. 39-88.
- Stewart, G. R., Lin, D. N. C., and Bodenheimer, P. 1984. Collision-induced transport processes in planetary rings. In *Planetary Rings*, eds. R. Greenberg and A. Brahic (Tucson: Univ. of Arizona Press), pp. 447-512.
- Stone, E. C., and Miner, E. D. 1991. The Voyager encounter with Neptune. *J. Geophys. Res.* 96:18903-18906.
- Synott, S. P. 1984. Orbits of the small inner satellites of Jupiter. *Icarus* 58:178-181.
- Synott, S. P., Peters, C. F., Smith, B. A., and Morabito, L. A. 1981. Orbits of the small satellites of Saturn. *Science* 212:191-192.
- Thomas, P. C., and Veverka, J. 1991. Neptune's small inner satellites. *J. Geophys. Res.* 96:19261-19268.
- Tittemore, W. C., and Wisdom, J. 1989. Tidal evolution of the Uranian satellites. II. An explanation of the anomalously high orbital inclination of Miranda. *Icarus* 77:63-89.
- Turtle, E., Porco, C., Haemmerle, V., Hubbard, W., and Clark, R. 1991. The kinematics of eccentric features in Saturn's Cassini division from combined Voyager and groundbased data. *Bull. Amer. Astron. Soc.* 23:1179 (abstract).
- Tyler, G. L., Sweetnam, D. N., Anderson, J. D., Borutzki, S. E., Campbell, J. K., Eshleman, V. R., Gresh, D. L., Gurrola, E. M., Hinson, D. P., Kawashima, N., Kursinski, E. R., Levy, G. S., Lindal, G. F., Lyons, J. R., Marouf, E. A., Rosen, P. A., Simpson, R. A., and Wood, G. E. 1989. Voyager radio science observations at Neptune and Triton. *Science* 246:1466-1473.
- Van Allen, J. A. 1983. Absorption of energetic protons by Saturn's ring G. *J. Geophys. Res.* 88:6911-6918.
- Van Allen, J. A. 1984. Energetic particles in the inner magnetosphere of Saturn. In *Saturn*, eds. R. Greenberg and A. Brahic (Tucson: Univ. of Arizona Press), pp. 281-317.

- Van Allen, J. A. 1987. An upper limit on the sizes of shepherding satellites at Saturn's ring. *G. J. Geophys. Res.* 92:1153–1159.
- Van de Hulst, H. C. 1981. *Light Scattering by Small Particles* (New York: Dover Publications), p. 107.
- Ward, W. R. 1981. On the radial structure of Saturn's rings. *Geophys. Res. Lett.* 8:641–643.
- Warwick, J. W., Evans, D. R., Peltzer, G. R., Peltzer, R. G., Romig, J. H., Sawyer, C. B., Riddle, A. C., Schweitzer, A. C., Desch, M. D., Kaiser, M. L., Farrell, W. M., Carr, T. D., de Pater, I., Staelin, D. H., Gulkis, S., Poynter, R. L., Boischot, A., Genova, F., Leblanc, Y., Lecacheux, A., Pedersen, B. M., and Zarka, P. 1989. Voyager planetary radio astronomy at Neptune. *Science* 246:1498–1501.
- Weidenschilling, S. J., and Davis, D. R. 1985. Orbital resonances in the solar nebula: Implications for planetary accretion. *Icarus* 62:16–29.
- Yoder, C. F., Synnott, S. P., and Salo, H. 1989. Orbits and masses of Saturn's co-orbiting satellites, Janus and Epimetheus. *Astron. J.* 98:1875–1889.